

EFFECT OF BLOWING PATTERN THROUGH LEADING EDGE ON FLOW  
STRUCTURE OF 45 DEGREE SWEPT DELTA WING

A THESIS SUBMITTED TO  
THE GRADUATE SCHOOL OF NATURAL AND APPLIED SCIENCES  
OF  
MIDDLE EAST TECHNICAL UNIVERSITY

BY

GÖKAY GÜNACAR

IN PARTIAL FULFILLMENT OF THE REQUIREMENTS  
FOR  
THE DEGREE OF MASTER OF SCIENCE  
IN  
MECHANICAL ENGINEERING

SEPTEMBER 2016



Approval of the thesis:

**EFFECT OF BLOWING PATTERN THROUGH LEADING EDGE ON FLOW  
STRUCTURE OF 45 DEGREE SWEEP DELTA WING**

submitted by **GÖKAY GÜNACAR** in partial fulfillment of the requirements for the degree of **Master of Science in Mechanical Engineering Department, Middle East Technical University** by,

Prof. Dr. Gülbin Dural Ünver  
Dean, Graduate School of **Natural and Applied Sciences**

Prof. Dr. R. Tuna Balkan  
Head of Department, **Mechanical Engineering**

Assoc. Prof. Dr. M. Metin Yavuz  
Supervisor, **Mechanical Engineering Dept., METU**

**Examining Committee Members:**

Assoc. Prof. Dr. Cüneyt Sert  
Mechanical Engineering Dept., METU

Assoc. Prof. Dr. M. Metin Yavuz  
Mechanical Engineering Dept., METU

Asst. Prof. Dr. Ali Emre Turgut  
Mechanical Engineering Dept., METU

Assoc. Prof. Dr. Oğuz Uzol  
Aerospace Engineering Dept., METU

Assoc. Prof. Dr. Selin Aradağ  
Mechanical Engineering Dept., TOBB ETU

**Date:** 07.09.2016

**I hereby declare that all information in this document has been obtained and presented in accordance with academic rules and ethical conduct. I also declare that, as required by these rules and conduct, I have fully cited and referenced all material and results that are not original to this work.**

Name, Last name: Gökay Günacar

Signature :

# **ABSTRACT**

## **EFFECT OF BLOWING PATTERN THROUGH LEADING EDGE ON FLOW STRUCTURE OF 45 DEGREE SWEEP DELTA WING**

Günacar, Gökay

M.S., Department of Mechanical Engineering

Supervisor: Assoc. Prof. Dr. Mehmet Metin Yavuz

September 2016, 87 pages

There has been an increasing interest in recent years in control of flow structure over non-slender delta wings, which are the simplified planforms of Unmanned Air Vehicles (UAV), Unmanned Combat Air Vehicles (UCAV), and Micro Air Vehicles (MAV). Different control approaches have been applied to alter the flow structure with particular interests in preventing stall and delaying vortex breakdown. Among different flow control techniques, blowing through leading edge of the wing has been commonly used due to its high effectiveness.

In the present study, the effect of blowing pattern through the leading edge on flow structure of a 45° swept delta wing is investigated by employing surface pressure measurement and laser illuminated smoke visualization in a low-speed suction-type wind tunnel. The air injection, which is controlled by a solenoid valve and the flow meters, is performed from the leading edges at chordwise distances of  $x/C=0.16$ , 0.44, and 0.68. By adjusting the injection rates at each chordwise distance, three different blowing patterns, descending, uniform, and, ascending, are applied at dimensionless momentum coefficients of 0.005, 0.01 and 0.02. The experiments are performed at attack angles of 7, 13, and 16 degrees and at Reynolds numbers varying from 14000 to 75000. The results indicate that the blowing through leading edge successfully eliminates the three-dimensional surface separation, which occurs at

relatively high attack angles. The effect of blowing pattern on flow structure is clearly evident for the corresponding cases in which the best performance is achieved by the descending blowing pattern. Furthermore, the results show that the blowing deteriorates the flow structure and moves the breakdown location toward upstream at relatively low attack angles where the leading edge vortex and its breakdown are apparent.

Keywords: Non-slender Delta Wing, Flow control, Leading Edge Blowing, Blowing Pattern

# ÖZ

## HÜCUM KENARINDAN YAPILAN ÜFLEME BİÇİMLERİNİN 45 DERECE OK AÇILI DELTA KANAT ÜZERİNDEKİ AKIŞ YAPISINA ETKİSİ

Günacar, Gökay

Yüksek Lisans, Makina Mühendisliği Bölümü

Tez Yöneticisi: Doç. Dr. Mehmet Metin Yavuz

Eylül 2016, 87 sayfa

İnsansız Hava Araçları (İHA), İnsansız Savaş Araçları ve Mikro Hava Araçları'nın basitleştirilmiş planformları olan düşük ok açılı delta kanatların akış yapısının kontrolü üzerine son yıllarda artan bir ilgi bulunmaktadır. Özellikle perdövites(stall) durumunun önlenmesi ve girdap kırımının geciktirilmesine yönelik olarak, akış yapılarını değiştirmek için farklı kontrol yaklaşımları uygulanmıştır. Kanadın hücum kenarından üfleme tekniği sahip olduğu yüksek verimlilik sebebiyle çeşitli akış kontrol teknikleri arasında sıklıkla kullanılmaktadır.

Bu çalışmada, 45° ok açılı kanadın hücum kenarı üzerinde akış kontrolü konseptinin etkisi, kanat yüzeyinde basınç ölçümü ve yüzey duman görüntülemesi tekniklerinin kullanıldığı bir düşük hızlı emme tipli rüzgar tüneli içerisinde incelenmiştir. Solenoit valf ve debimetreler ile kontrol edilen hava üflemesi kanat hücum kenarının  $x/C=0.16, 0.44, 0.68$  noktalarından verilmiştir. Kanat ucu girdabının oluşumu, kırımını ve farklı akış kontrol stratejileri detaylı olarak incelenmiştir. Deneyle 7°, 13° ve 16° olmak üzere farklı hücum açıları ve farklı Reynold Sayıları'nda yapılmıştır. Yüzey yakınından ve yüzeye dik düzlemlerden sağlanan akış görüntüleme sonuçları kanat ucu girdabı ve girdap kırımın yerleri hakkında bilgi sağlamıştır. Kanadın her iki tarafından üfleme oranları ayarlanarak azalan, sabit ve

artan üfleme dizilimlerinde 0.005, 0.01 ve 0.02 boyutsuz momentum katsayıları olarak 3 farklı üfleme dizilimi uygulanmıştır. Deneyle 7, 13 ve 16 hücum açılarında 14000 ile 75000 arasında deęişen Reynolds sayılarında gerçekleştirilmiştir. Sonuçlar kanat hücum kenarından yapılan üfleme tekniğinin kısmen yüksek hücum açılarında oluşan üç boyutlu yüzeyden ayrılmayı başarılı bir şekilde önlemiştir. Azalan üfleme biçimiyle elde edilen en iyi performanslarda, üfleme biçiminin akış yapısına etkisi açıktır. Buna ek olarak, sonuçlar hücum kenarı girdabının ve kırınımının görüldüğü hücum açısının düşük olduđu durumlarda üflemenin akış yapısını bozduğunu ve kırınım noktasını yukarı doğru taşıdığını göstermektedir.

Anahtar kelimeler: Orta ok açılı delta kanat, Akış kontrol, Hücum kenarından üfleme, Üfleme biçimi

*To my parents*

## ACKNOWLEDGMENTS

I would like to deliver my sincerest gratitude to my supervisor Assoc. Prof. Dr. M. Metin Yavuz for his support, encouragement, patience, criticism and guidance throughout this study. It was the greatest pleasure and a precious experience for me to work with such a good person in my life.

I am fully grateful to my colleagues/friends Alper Çelik, İlhan Öztürk and Mohammad Reza Zharfa for their support in experiments and data processing, and to Mahmut Murat Göçmen, Kadir Ali Gürsoy, Cenk Çetin, Yiğitcan Güden and Emin Oğuz İnci for their technical support on editing this thesis.

I would like to thank Ali Karakuş for his sincere support, without his coffee and tea breaks this thesis would not be possible.

I would like to express my deepest appreciation to my beloved roomies Berat Çelik and Eren Demircan for keeping me alive during this stressful period.

I would also like to thank past and current members of Fluid Mechanics Laboratory: Osman Akdağ, İsa Kavas, Habib Can Tunç, Gizem Şencan, Mehmet Yalılı, Gülsüm Çaylan, Berksu Erkal, Burak Gülsaçan and to all other members of the fluid lab.

I would like to show my gratitude to the lab technicians Rahmi Ercan and Mehmet Özçiftçi for their invaluable help.

Last but the most, I owe my deepest gratitude to my parent Nurcan and Murat Günacar, for their unconditional love, support and encouragement, which made possible all the years spent here.

# TABLE OF CONTENTS

ABSTRACT.....	v
ÖZ .....	vii
ACKNOWLEDGMENTS .....	x
TABLE OF CONTENTS.....	xi
LIST OF TABLES .....	xiii
LIST OF FIGURES .....	xiv
NOMENCLATURE.....	xvii
CHAPTERS	
1. INTRODUCTION .....	1
1.1 Motivation of the Study .....	4
1.2 Aim of the Study .....	5
1.3 Structure of the Thesis .....	5
2. LITERATURE REVIEW.....	9
2.1 Flow Structure on Delta Wing .....	9
2.2 Control of Flow Structure on Delta Wing.....	10
3. EXPERIMENTAL SYSTEM AND TECHNIQUES .....	21
3.1 Wind Tunnel.....	21
3.1.1 Wind Tunnel Characterization .....	21
3.2 Delta Wing Model.....	22
3.3 Qualitative Flow Measurement – Laser Illuminated Smoke Visualization .	24
3.4 Quantitative Flow Measurement - Pressure Measurements.....	25
3.5 Steady Blowing Setup.....	26

3.6 Experimental Uncertainty Analysis .....	28
4. RESULTS AND DISCUSSION .....	41
4.1 Results of Surface Flow Visualization .....	41
4.2 Results of Cross Flow Visualization .....	44
4.3 Pressure Measurements .....	46
5. CONCLUSION AND RECOMMENDATIONS FOR FUTURE WORK .....	67
5.1 Conclusion.....	67
5.2 Recommendations for Future Work.....	69
REFERENCES.....	71
APPENDICES	
A. SOURCE CODES OF CALCULATION OF PRESSURE COEFFICIENT .	77
B. CALCULATION OF UNCERTAINTY .....	83
C. PRESSURE MEASUREMENTS FOR $Re=20000$ .....	85

## LIST OF TABLES

### TABLES

Table 3.1 Results of velocity measurements inside the test section at different fan powers. ....	22
Table 3.2 Turbulence intensities that were measured via LDA in the test section at different velocities.....	22
Table 3.3 Summary of pressure measurement uncertainty .....	30
Table 3.4 Summary of momentum coefficient uncertainty .....	30
Table 3.5 Relative uncertainty at different Reynolds numbers.....	31

# LIST OF FIGURES

## FIGURES

Figure 1.1 Current and future unmanned combat air vehicles and micro air vehicles [2] .....	6
Figure 1.2 Sketch of vertical flows around a delta wing [3] .....	7
Figure 1.3 Leading-edge vortices and vortex breakdown over 65°-sweep wing [13].	7
Figure 1.4 Variation of lift coefficient with angle of attack, adapted from [11].	8
Figure 2.1 Surface oil flow visualization of the flow over a 50 degree sweep delta wing at an angle of attack 2.5 degree [4] .....	17
Figure 2.2 Dye flow visualization for vortex flow for $\alpha = 5^\circ$ at $Re = 8.7 \times 10^3$ in water tunnel experiments[50].....	18
Figure 2.3 Flow visualization of leading-edge vortex for a) jet off, b) jet on, and c) just after the jet is turned off [47].....	18
Figure 2.4 Vortex control techniques: a)VCB, b)SWB, c)PLEB d)TLEB, e)RASB.	19
Figure 2.5 Magnitude of time averaged cross flow velocity at $x/C=0.28$ , for $St=1.3$ and $\alpha=25^\circ$ [6] .....	19
Figure 2.6 Section view of leading edge tip geometries tested[6] .....	20
Figure 2.7 Comparison of unsteady blowing at a range of momentum coefficients from different leading edge tip profiles, $\alpha=25^\circ$ , $x/C=0.28$ [6] .....	20
Figure 3.1 The low speed wind tunnel facility used in this study .....	32
Figure 3.2 Optically transparent test section .....	32
Figure 3.3 Experiment matrix .....	33
Figure 3.4 Calibration curve of the wind tunnel for obtaining the required fan power for a given velocity.....	33
Figure 3.5 Plan view of the delta wing showing pressure taps located at the three chordwise stations and blowing holes at leading edges .....	34
Figure 3.6 Cross-section view of blowing hole.....	34
Figure 3.7 CAD drawing of the fabricated delta wing .....	35

Figure 3.8 Photographs of the fabricated delta wing from different views; a) Top-back view, b) Bottom view, which also shows the pressure taps that were used in pressure measurements.....	35
Figure 3.9 The smoke generator used in experiments (Plint&Partners Como3694) .	36
Figure 3.10 Experimental set-up for flow visualization at cross-flow planes $x/C=0.32$ , $0.56$ and $x/C=0.80$ (plan view).....	36
Figure 3.11 Experimental set-up for flow visualization at a plane parallel to the leading edge vortices (side view).....	37
Figure 3.12 The 16-channel pressure scanner system used in the experiments (Netscanner 9116).....	37
Figure 3.13 Schematic of control setup.....	38
Figure 3.14 Schematic of different flow control patterns; a) descending, b) uniform, c) ascending.....	38
Figure 3.15 Velocity measurement at the exit of the jet hole. ....	39
Figure 4.1 Surface flow visualization at $\alpha = 7^\circ$ angle of attack and $Re = 14000$ , at different momentum coefficients and blowing patterns .....	50
Figure 4.2 Surface flow visualization at $\alpha = 7^\circ$ angle of attack and $Re = 35000$ , at different momentum coefficients and blowing patterns .....	51
Figure 4.3 Surface flow visualization at $\alpha = 13^\circ$ angle of attack and $Re = 14000$ , at different momentum coefficients and blowing patterns .....	52
Figure 4.4 Surface flow visualization at $\alpha = 13^\circ$ angle of attack and $Re = 35000$ , at different momentum coefficients and blowing patterns .....	53
Figure 4.5 Surface flow visualization at $\alpha = 16^\circ$ angle of attack and $Re = 14000$ , at different momentum coefficients and blowing patterns .....	54
Figure 4.6 Surface flow visualization at $\alpha = 16^\circ$ angle of attack and $Re = 35000$ , at different momentum coefficients and blowing patterns .....	55
Figure 4.7 Cross flow visualization on $x/C = 0.32$ and $x/C = 0.80$ chordwise distances at $\alpha = 7^\circ$ angle of attack and $Re=14000$ for different momentum coefficients.....	56

Figure 4.8 Cross flow visualization on $x/C = 0.32$ and $x/C = 0.80$ chordwise distances at $\alpha = 7^\circ$ angle of attack and $Re=35000$ for different momentum coefficients .....	57
Figure 4.9 Cross flow visualization on $x/C = 0.32$ and $x/C = 0.80$ chordwise distances at $\alpha = 13^\circ$ angle of attack and $Re=14000$ for different momentum coefficients .....	58
Figure 4.10 Cross flow visualization on $x/C = 0.32$ and $x/C = 0.80$ chordwise distances at $\alpha = 13^\circ$ angle of attack and $Re=35000$ for different momentum coefficients .....	59
Figure 4.11 Spanwise $-C_p$ plots at $\alpha = 7^\circ$ angle of attack and $Re=35000$ on chordwise distances of $x/C = 0.32, 0.56$ and $0.80$ and different Reynolds numbers .	60
Figure 4.12 Spanwise $-C_p$ plots at $\alpha = 7^\circ$ angle of attack and $Re=75000$ on chordwise distances of $x/C = 0.32, 0.56$ and $0.80$ and different Reynolds numbers .	61
Figure 4.13 Spanwise $-C_p$ plots at $\alpha = 13^\circ$ angle of attack and $Re=35000$ on chordwise distances of $x/C = 0.32, 0.56$ and $0.80$ and different Reynolds numbers .	62
Figure 4.14 Spanwise $-C_p$ plots at $\alpha = 13^\circ$ angle of attack and $Re=75000$ on chordwise distances of $x/C = 0.32, 0.56$ and $0.80$ and different Reynolds numbers .	63
Figure 4.15 Spanwise $-C_p$ plots at $\alpha = 16^\circ$ angle of attack and $Re=35000$ on chordwise distances of $x/C = 0.32, 0.56$ and $0.80$ and different Reynolds numbers .	64
Figure 4.16 Spanwise $-C_p$ plots at $\alpha = 16^\circ$ angle of attack and $Re=75000$ on chordwise distances of $x/C = 0.32, 0.56$ and $0.80$ and different Reynolds numbers .	65
Figure C.1 Spanwise $-C_p$ plots at $\alpha = 7^\circ$ angle of attack and $Re=20000$ on chordwise distances of $x/C = 0.32, 0.56$ and $0.80$ and different Reynolds numbers .	85
Figure C.2 Spanwise $-C_p$ plots at $\alpha = 13^\circ$ angle of attack and $Re=20000$ on chordwise distances of $x/C = 0.32, 0.56$ and $0.80$ and different Reynolds numbers .	86
Figure C.3 Spanwise $-C_p$ plots at $\alpha = 16^\circ$ angle of attack and $Re=20000$ on chordwise distances of $x/C = 0.32, 0.56$ and $0.80$ and different Reynolds numbers .	87

## NOMENCLATURE

$\Lambda$	Sweep angle
$C$	Chord length
$s$	Semi span length
$\alpha$	Angle of attack
$Re$	Reynolds number based on chord length
$U_\infty$	Free stream velocity
$\omega$	Vertical velocity
$x$	Chordwise distance from wing apex
$y$	Spanwise distance from wing root
$p$	Static pressure
$\bar{p}$	Average of the static pressure
$p_\infty$	Static pressure of the flow
$p_{dyn}$	Dynamic pressure of the flow
$C_p$	Pressure coefficient
$C_\mu$	Momentum coefficient
$\rho$	Density of the fluid
$\nu$	Fluid kinematic viscosity



# CHAPTER 1

## INTRODUCTION

The interest of military applications to Micro air vehicles and Unmanned air vehicles, has made triangular planforms very popular [1]. Many applications are performed to fulfill a need of performance of micro air vehicles and unmanned air vehicles, which need sufficient lift force and maneuverability under difficult flight conditions.

Delta wings are generally classified into two groups such as slender and non-slender wings. Non-slender wing planform stands out to produce high levels of lift due to its larger triangular shape compared to slender delta wing, which has a sweep angle more than 55 degrees. Gursul et al. [2], [3] defined the non-slender wings as one with a leading-edge sweep equal to or less than 55°, and slender wings, which have a leading edge sweep more than 55°. Some of the unmanned air vehicles and micro air vehicles, which have delta wing planforms with low sweep angle, are demonstrated in Figure 1.1. Due to the existence of aerodynamic, stability and control issues of these vehicles, laminar-transitional flows occur, and so the separation, transition and vortical flows take a part [2]. Gursul et al. worked on unsteady aerodynamics of non-slender delta wings in terms of its shear layer, instability, vortex structure and its interactions as well. It was emphasized that the non-slender delta wings deliver distinct features compared to slender wings at high angles of attack. Lee et.al reported that wings having 70 degrees sweep angle are able to improve its lift ability up to 40 degrees of angle of attack[4]. In contrast, an airfoil loses its lift feature about 15 degrees. Further investigations on lift enhancement of these planforms enlightened the idea that lift coefficient is proportional to the sweep angle[5]. Hence, recent studies have pushed researchers to understand flow over non-slender delta wing planforms.

Flow characteristic of the delta wing is highly dependable to angle of attack and the wing geometry. The flow over delta wing at angle of attack separates from windward side of the leading edges and then turns into curved free shear layers[3]. Two counter rotating leading edge vortices dominate the flow at a moderate incidence over slender delta wings. Typical leading edge vortices over a slender delta wing is depicted in Figure 1.2 [3], [6]. This primary vortex structure is known to be fully developed as long as its formation exists along the entire leading edge[7]. The interaction of the primary vortex with the boundary layer developing at the inboard of the wing is resulted with secondary vortex formation rotating in opposite direction with respect to primary vortices, which can also be seen at non-slender delta wings at low incidences[3], [7], [8]. Leading edge vortices (LEV) generated by delta wings are very crucial for the performance of the aircraft. For slender wings, primary vortex structure occurs due to the rollup of shear layer separation. These LEV's dominate the flow on slender wings at considerably high angles of attack [9]. Ol and Gharib [8] conducted their experiments with delta wings of  $50^\circ$  and  $65^\circ$  sweep in a water tunnel within Reynolds numbers of  $6 \times 10^3 - 1.5 \times 10^4$ . The experiments, performed with PIV, which is a method of flow visualization, revealed the occurrence of LEV for both  $50^\circ$  and  $65^\circ$  wings up to 2.5 degree angle of attack.

Increase in attack angle causes formation of different form of instability, which is including vortex breakdown [2]. Vortex breakdown, which was first observed by Werle in 1954, occurs particularly when the flow loses its momentum at high angles of attack [10]. However, the consequence of this behavior, which is loss in lift, corresponds to behavior of slender delta wings. The vortex breakdown location, observed on non-slender delta wings, is not easy to determine compared to slender wings, which makes visualization experiments more challenging [2]. An example of visualization of vortex breakdown is depicted in Figure 1.3. In earlier studies, it was indicated that observing vortex core and vortex breakdown, on the delta wings having 45 and 55 degrees sweep angle, were difficult due to the unsteadiness of the flow [5]. Wentz and Kohlman [11] stated that the vortex breakdown was seen near the apex for 50 degree wing. Those studies were conducted at same Reynolds numbers, which were at the order of  $10^6$ . However, they concluded that the location of vortex breakdown could not be found for  $45^\circ$  delta wing. It was stated that the

breakdown, at small angle of attacks, was close to the apex.

The magnitude of leading edge vortices increases when they interact with streamwise flow [12]. This interaction stabilizes the flow on the wing and results with additional lift force, which is one of the distinct features of unmanned combat air vehicles and micro air vehicles [13]. Yayla declared that the contribution of leading edge vortices to total lift is about 40% at high incidences [14]. The comparison of lift coefficient of delta wings having different swept angle is shown in Figure 1.4 [5]. The same study claims that stall angles and the maximum lift coefficients of moderate wings are lower than slender wings. Polhamus' study states that lift enhancement by vortices at low angles of attack less effects the total lift.

Recent investigations reveal the significance of the reattachment of the flow to the wing surface, which is separated from the leading edge [7]. For slender delta wings reattachment line is through the inboard of the vortex core that occurs only at low incidences, whereas the shear layer separated from leading edge may reattach to the wing surface for non-slender delta wings constituting a vortex bound which may occur even after vortex breakdown [3].

At sufficiently high angle of attack, onset of the breakdown location is shifted closer the wing apex and when it reaches to the apex the wing is completely stalled [15]. For non-slender delta wings primary attachment location is through the outboard of the wing root chord, even when the breakdown approaches to apex. Increasing attack angle moves the attachment line towards the inboard plane that causes the considerable buffeting within the attachment region. And a further increase in angle of attack causes the eradication of flow reattachment which is resulted with the coalescence of vortex bounds from both sides of the wings together with the stall of the wing [2]. Low swept delta wings should be characterized with the attention of vortex structure . This attention should be considered together with the near surface flow patterns. This approach would reach to characterization of three dimensional surface separation of the wing, which is related with leading edge vortex[16]. Three dimensional separated flows are defined as concentration of vorticity, which occurs due to existence of boundary layer separation. Once the separation occurs, vorticity

starts to accumulate in the vicinity of surface and creates rolling up formation of vortices[17].

Flow separation, vortex structure, flow reattachment, vortex breakdown and vortex instabilities are the parameters, need to be controlled. Flow structure, which changes the aerodynamics performance of wing completely differs with increasing angle of attack. Hence, control of these structures is vital part of the design for these planforms. Various flow control techniques have been applied to delta wings by researchers in decades, such as multiple vortices, control surfaces, blowing and suction, low-frequency and high frequency excitation, feedback control, passive control with wing flexibility and plasma actuators [3]. Two basic methods are active and passive control techniques. Controlling vortices over slender delta wing can be accomplished by modifications, which correspond to passive control technique. Recent studies indicate that highly flexible delta wings are required to implement passive control method [18]. To manufacture flexible wing is challenging, for this reason implementing flow control technique to delta wing without interfering its structure is priority of this study.

There are different kinds of control techniques applied to alter the flow structure including leading edge vortex, three-dimensional surface separation, and other forms of flow instabilities. Well known methods are classified as blowing and suction through the leading edge or trailing edge [4] of the planform. Recent studies confirm that excitation of the leading edge vortices with different blowing patterns may exhibit effective results on the flow structure of delta wing[19]–[21].

### **1.1 Motivation of the Study**

Micro Air Vehicles (MAV), Unmanned Combat Air Vehicles (UCAV) and Unmanned Air Vehicles (UAV) experience complex flow patterns during steady flight and/or defined maneuvers, which must be first well understood and then controlled in order to optimize the flight performances. Different control approaches have been applied to alter the flow structure with particular interests in preventing stall and delaying vortex breakdown. Among different flow control techniques, blowing through leading edge of the wing has been commonly used due to its high effectiveness. However, very few studies in literature have investigated the effect of

blowing pattern on flow structure of non-slender delta wing. In addition, this effect needs full characterization for different attack angles, Reynolds numbers, and momentum coefficients.

## **1.2 Aim of the Study**

The present study aims to investigate the effect of blowing pattern through the leading edge on flow structure of a  $45^\circ$  swept delta wing by employing surface pressure measurement and laser illuminated smoke visualization. For this purpose, the flow control setup was built in which the air is injected through blowing holes from the leading edges at chordwise distances of  $x/C=0.16$ ,  $0.44$ , and  $0.68$ . By adjusting the injection rates at each blowing hole, three different blowing patterns, descending, uniform, and, ascending, are applied at dimensionless momentum coefficients of  $0.005$ ,  $0.01$  and  $0.02$ . For descending and ascending blowing patterns, different amount of momentum is provided through each hole, such that the injected momentum decreases/increases from the apex toward the trailing edge. The experiments are performed at attack angles of  $7$ ,  $13$ , and  $16$  degrees and at Reynolds numbers varying from  $14000$  to  $75000$ .

## **1.3 Structure of the Thesis**

This thesis is composed of five main chapters. Chapter 1 provides introductory information for the delta wing flows and the aim of the study along with the motivation.

The related previous studies in literature including the flow structure on delta wings and flow control techniques are summarized and discussed in Chapter 2. The topics related to slender delta wings are briefly mentioned and the major attention is given to the non-slender delta wings.

Technical details of the flow control set-up and the measurement systems used in the current study are given in Chapter 3. The methodology followed for conducting the steady blowing measurements is discussed in detail.

The results are summarized and discussed in Chapter 4. First, surface and cross flow visualization results are reported. Then, the surface pressure measurement results are reported.

Chapter 5 provides the conclusions throughout the study including the recommendations for possible future work.



Figure 1.1 Current and future unmanned combat air vehicles and micro air vehicles [2]

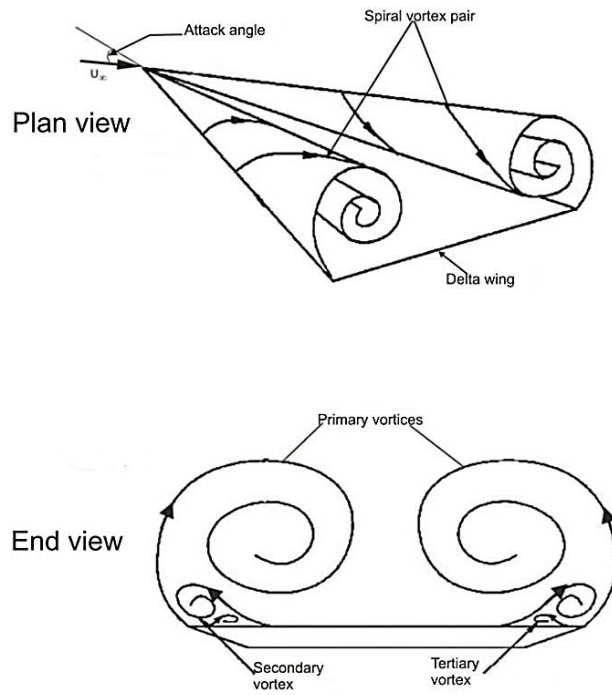


Figure 1.2 Sketch of vertical flows around a delta wing [3]

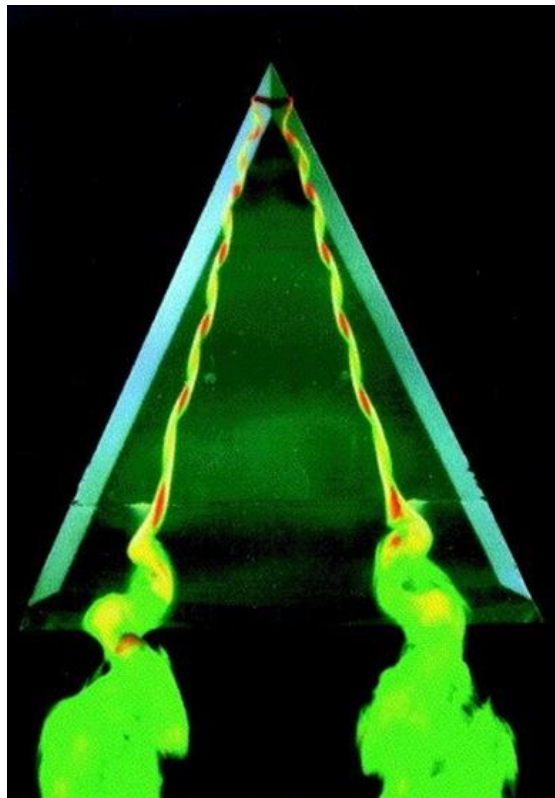


Figure 1.3 Leading-edge vortices and vortex breakdown over 65°-sweep wing [13]

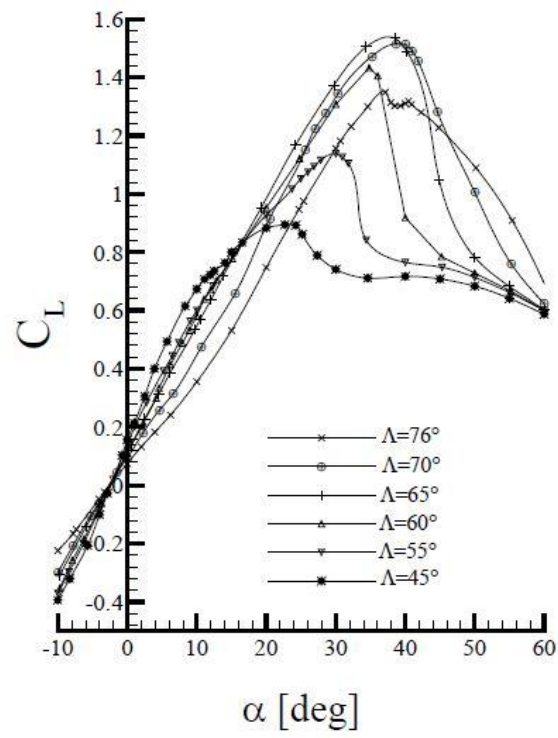


Figure 1.4 Variation of lift coefficient with angle of attack, adapted from [11]

## CHAPTER 2

### LITERATURE REVIEW

#### 2.1 Flow Structure on Delta Wing

Although the unsteady flow structure over high sweep wings are well understood, there is still a lack of information about phenomena over low and moderate sweep wings which requires further studies on these geometries [7]. Numerous studies, have been performed to comprehend the flow structure on unmanned combat air vehicles and micro air vehicles. Understanding the vortex structure of moderate delta wings has vital significance due to the high demands and investments of the defense industry. Extensive and elaborate work was conducted for high sweep wings, which give brief insight about non-slender wings. Unsteady vortical flow structure over high sweep delta wings has been discussed by Rockwell and Visbal broadly [22], [23]. Studies show that boundary layer and primary vortex interaction causes secondary vortex, which is in the opposite direction. Figure 2.1 represents the experiment conducted by Taylor and Gursul, which clearly depicts the primary attachment line and the secondary separation line [9]. It is suggested that for Reynolds numbers on the order of  $10^3$ , vortices draw wake-like velocity profiles and exist close to the wing surface, hence vortex and boundary layer interaction becomes important. Increasing the angle of attack yields vortex breakdown location to approach wing's tip and therefore, shear layers become more dominant for the flow structure. Figure 2.2 clarifies that as the Reynolds number is increased, dual vortex structure occurred due to the interaction between boundary layer and primary vortex starts to lose its significance and secondary vortex undergoes a sudden expansion earlier than the primary vortex. Another experimental study was conducted by Shih and Ding [24] for 60 degree wing and the results were confirming the essence of primary leading edge vortices and the secondary vortices, which is a result of

interaction of vortex structures within the shear layer. Moreover, flow visualizations via dye injection were conducted by Ol and Gharib [8] for 50 and 60 degree delta wings at Reynolds numbers of  $6 \times 10^3$ - $1.5 \times 10^4$ . Experimental study suggests that both wings have similar flow characteristics such as geometry of leading edge shear layer, leading edge vortex and velocity distribution when the angle of attack is under 10 degree. However, when the incidence becomes higher than 10 degree, flow fields differ qualitatively. Vortex breakdown location [25], vortex shedding [26], vortex wandering [27], helical mode instability [25], [28] and shear layer instabilities [29] are some of the terms that unsteady flow phenomena includes for high and low swept delta wings. The utmost importance of these terms arises from their effects on buffeting at aircraft structures such as wings and fins and aircraft stability, which has been certified in detail by the aforementioned researchers.

## **2.2 Control of Flow Structure on Delta Wing**

Since non-slender and moderate swept angle delta wings have the ability of providing extra lift force compared to conventional wings and high swept delta wings, further research is demanded to increase the potential of these planforms. Some of the current studies focus on using flexible delta wing planforms, whereas structural behavior of wings could be used as passive flow control to improve capability of non-slender planforms [30]–[32]. The advantage of flow control technique is that it is possible to manage the desired flow control by making small changes rather than changing design parameters significantly on wing structure, such as modifying flowfield around tip of the wing. Thus, with small amount of energy, flow parameters can be altered[20], [33]. However, any control mechanism requires an energy from outside to the system is called active flow control method, where steady or unsteady blowing or suction could be used whether on the whole wing or on some specific location of the wing geometry such as trailing edge or leading edge. There are some other cases, which are called as active flow control techniques such as piezoelectric excitation and small and large scale perturbations.

Werle [10] proposed the first illustration of delaying vortex breakdown via suction along the vortex axis. In order to explain behavior of vortex breakdown against suction, Parmenter and Rockwell [34] conducted similar experiment. Furthermore, in

another experiment, by implementing blowing holes to the vortex core, delay of vortex breakdown was achieved [18]. Pulsed blowing was also efficient at different angles of attack during maneuver [35]. Helin and Watry [36] and Shih and Ding [37] proved that excitation from trailing edge has substantial effect on delaying vortex breakdown. Phillips et al. [38] remarked that fin is not a limiting factor when the trailing edge blowing is applied to eliminate or delay vortex breakdown. Figure 2.3 shows two different cases, which are visualization captures when the blowing jet is on, off and just after jet is off. It suggests that when the blowing process is on, it seems to be in line with the blowing direction. When the jet is turned off, the vortex starts to follow free stream direction and it becomes almost parallel to the free stream. However, almost all vortex control techniques aims to improve the structure, it is better to denote that some of the flow control methods might result in early vortex breakdown in some cases, where strength of vortex cause vortex lift at low incidences. Most powerful way to control the flow around delta wing is known to be steady flow control. But, Gu et al. [39] proposed an application, in which the blowing is injected through tangential direction and given periodically. The results were to confirm the delay of vortex breakdown and proved that oscillatory blowing through leading edge increases the lift forces at high angles of attack.

Despite, previous studies suggested that blowing through leading edge is a both effective and efficient method, trailing edge studies seems to be more practical due to its feasibility for real delta wings planforms. Helin [36] tested 60 degree delta wing at angles of attack of 0, 10, 20, 30 degrees. Directions of the blowing nozzles were parallel to the wing surface and the velocity ratios injected from nozzles were in the range of 0 and 8. This flow control techniques was able to delay vortex breakdown up to 18%. Nawrocki [40] spent more effort on the previous study and implemented horizontally vectored nozzles to the trailing edge. In addition to Helin's study, downstream displacement was seen for the vortex breakdown location, however, results yield that the vortex breakdown location depends on the nozzle angle. Another study conducted by Shih and Ding [37] has the purpose of implementing larger nozzles by manufacturing thicker delta wing planform. Results confirmed that vortex breakdown was delayed about 10% within the range of 10 to 35 degree angles of attack. Considering the earlier trailing edge studies, it is suggested that 45 degree

vectored angle is suitable for the largest delay of vortex breakdown. Breakdown was delayed up to 50% of the chord. Experiments were varied for different blowing cases such as asymmetric applications. For instance, in some applications portside of the wing has nozzles, which are looking downward with 30 degree, while starboard nozzles are looking upward with 30 degree and downward deflected nozzle is able to delay vortex location at about 22% of the chord. However, the impact of the upward deflected nozzle was not significant enough to alter vortex breakdown location. In following years, studies diversified and researchers started to combine different control techniques as well. Renac et al.[21] provided new experiments with rounded leading edge delta wing, which has 60 degree sweep angle. Qualitative and quantitative measurements are obtained for different Reynolds numbers and different blowing coefficients and strategies. First aim of this experiment was to provide new measurements with its particular geometry, which is similar to real air combat vehicles. Second aim of the experiment was to alter properties of the flow structure, which is dominated by counter rotating vortices. In addition, jet holes are fabricated at one side of the wing in order to get rolling moment. Results showed that vortex breakdown occurs earlier compared to slender ones and its development is slowed down by the rounded leading edges. The blowing coefficient, which is less than 0.02, barely alter vortex breakdown location, however, it modifies vortex structure. Such study was conducted by Vorobieff and Rockwell [41], [42] to emphasize that multiple actuators might be useful for delta wing studies. The idea was to excite the flow structure by using leading edge flaps and trailing edge blowing together. Experiments were conducted over 75 degrees swept angle delta wing and the air was injected through trailing edge with nozzles 30 degrees deflected downward. The results showed that delay of breakdown can reach up to 16% of the chord. Mitchell et al. [33] performed his experiment in a water channel and the wing mounted to the test section had 75 degree sweep angle. Dye injection holes were oriented on the leading edge for each side. Injection locations were 30, 50, 90 and 130 mm away from the tip of the wing, respectively. Tests were run at Reynolds number  $4 \times 10^5$  and velocity ratios injected through trailing edge were 0, 5, 10, 15. Since the delta wing models presented above correspond to different nozzle areas, they have different velocity ratios and different vortex breakdown locations as well. Then, comparisons

with the nondimensional momentum coefficients will be performed. In this study momentum coefficient  $C_\mu$  shows variations for asymmetric applications. Mitchell et al. identified an asymmetry of vortex breakdown on different sides. This information was associated to small yaw angle with respect to free stream flow in water tunnel. The vortex breakdown location of no flow control case were oscillating about 5% which had an agreement with the previous experiments performed in wind tunnel and water tunnel facilities. For asymmetric flow control, experiments demonstrated quite good results and were consistent at all flow rates. However, asymmetric injection caused early vortex breakdown. In addition to that, symmetric flow control was tend to create an early vortex breakdown, as well as asymmetric flow control, when the flow injection was in a high velocity ratio range. Yavuz and Rockwell [43] used PIV to characterize flow patterns adjacent to the surface of trailing edge controlled 35 degree sweep delta wing at angles of attack 5, 8 and 10 degree. Experiments were conducted for two types of blowing configuration: single and double injection. The momentum coefficient range was able to cover both previous studies and the possible applications might be used in future planforms as well. Topological results showed that even at small amount of blowing through trailing edge might remarkably modify the flow structure. However, surface flow patterns lose its susceptibility to blowing through trailing edge, when angles of attack reach their critical values. Additionally, comparison of blowing types indicated that dual blowing dramatically excites the flow structure, while the effect of single blowing way smaller than the dual blowing. Conversely, single blowing became much more efficient when it reaches to high value of momentum coefficient. Johari et al. [18] investigated four different methods to understand the complex flow behavior of delta wing, which had 60 degree sweep angle. Figure 2.4 represents the blowing configurations tested in this study. First method is vortex core blowing, which aims to delay vortex breakdown by exciting the flow of the vortex. However, Malcolm and Skow [44] qualitatively studied on the same subject and implied that due to the lack of physical advantages of the system, the method's effectiveness is moderate and implementing blowing nozzles externally disturbs the actual flow passing through the wing. Second method is spanwise blowing, which demonstrates exciting the vorticity of the shear layer flow along the leading edge to enhance the vortex strength. Spanwise blowing achieved to have

17% improvement lift with a moderate blowing coefficient 0.1. However, this advantage results in premature secondary vortex breakdown. Parallel leading edge blowing is the third method covered in this study. Despite it seems to be as same as spanwise blowing explained above, this technique is completely different regarding blowing holes are located into the wing's structure. Results showed that there is 20% improvement in lift, when the angle of attack is 15 degree and the momentum coefficient is 0.08. The cumbersome of this technique is that the required momentum for a continuous control effect is significantly high. The fourth technique investigated is called as tangential leading edge blowing, which consists of blowing fluid tangent to the leading edges. This technique is able to increase lift coefficient about 30%. A novel control technique, similar to spanwise blowing, is recessed angle spanwise blowing. Injection ports are located at three different locations: 20, 30.5 and 41% of the chord. Blowing increased vortex stability and improved the delay of vortex breakdown. In summary, study suggests that recessed angle spanwise blowing has a small range of momentum coefficient compared to tangential leading edge blowing. Recessed angle spanwise blowing seems to be easier to apply, because there are only a few parts to implement to the system.

Margalit et al. [45] performed unsteady blowing, square wave, which is more efficient compared to sine wave and drew attention that high frequency results in effective pulse. Furthermore, in order to emphasize the locations where square wave blowing is effective, delta wing was divided into sections. Effective locations were denoted as  $x/C=0.76$  to  $0.88$  and stated any blowing independent of its location resulted in increase in normal force.

Riou and Garnier [46] demonstrated the suction flow control on 65 degree sweep delta wing to emphasize how that technique changes aerodynamic characteristics of the air vehicle in transonic regime. Suction slots were located on the leading edge and the momentum coefficient was 2%. It was emphasized that suction significantly change vortex breakdown location, furthermore, it erased the trace of secondary vortex. Results indicated that magnitude of the pressure coefficient decreases when the suction is carried out. The decrease reached 23% at front station, while the decrease at rear station was about 12%. The change in lift coefficient was about 22% improvement and the drag force decreased about 9%. Another suction flow control

technique was performed by McCormick and Gursul [47]. Their studies focused on changing the vortex location by using small amount of leading edge suction, which significantly alter the vortex core location at the end. This study aimed to control shear layer over delta wings, which have 65 and 70 degree of sweep angle. Results suggested that using suction technique could move the vortex breakdown location to downstream.

Wang et al. [48] tested two different wing models with the sweep angles of 50 and 60, which represents moderate and low swept wings. There were two different nozzles tested, which were rectangular and circular ones. The study includes velocity measurement, force measurement and flow visualization. This study mostly focused on measuring aerodynamic forces on delta wings and sweep angle effect. Nozzle geometry, which affects the interaction between boundary layer and shear layers was investigated [49]. In order to give a better insight to the flow characteristics, PIV (particle image velocity) measurement was done close to the wing surface. According to the results, blowing through centerline was quite reasonable on slender delta wing compared to non-slender delta wing. Effect of nozzle geometry was investigated with the help of PIV measurement on a crossflow plane. Results confirmed that both nozzles create counter rotating vortex structures as the injection starts. Distance between counter rotating vortices was larger when the injection was performed with rectangular nozzles. This study concluded that the effect of trailing edge blowing has the same effect on aerodynamic forces on different sweep angle wings, which are 50 and 65. Williams et al. [6] examined leading edge unsteady flow control on 50 degree sweep angle delta wing. Results taken via PIV measurement and pressure measurement, to explore vortex formation of unsteady blowing, were compared to the case without blowing. Figure 2.5 depicts the separated shear layer and the effect of excitation, which is also reformation of the vortex breakdown by the increasing injection. In order to clarify what type of wing is effective, 4 different tip design were tested. Figure 2.6 represents the cross section of different wings tested. Comparison of blowing through different leading edges, whereas the location on  $x/C=0.28$  at 25 degree angle of attack, is represented in Figure 2.7. Most efficient results were collected via tip 3, which was consistent to increase suction effect. First two tips tend to create a premature vortex and tip 4 had almost no effect on the flow

structure passing through the wing. In fact, tip 3 is more likely a combination of other types, and is the one closest to shear layer and the wing surface.

To conclude, the aim of flow control techniques might be whether the improvement of the lift force or to control features of flight. Studies explored above concluded that one of distinct feature of delta wing, reattachment, can be altered or improved. Leading edge blowing mostly strengthens the vortices or can create early vortex breakdown as well. Suction decreases the strength of vortex breakdown and is able delay vortex breakdown. However, trailing edge blowing seems to be least efficient technique to alter or delay vortex breakdown, its effect increases prior to stall on low swept delta wings.

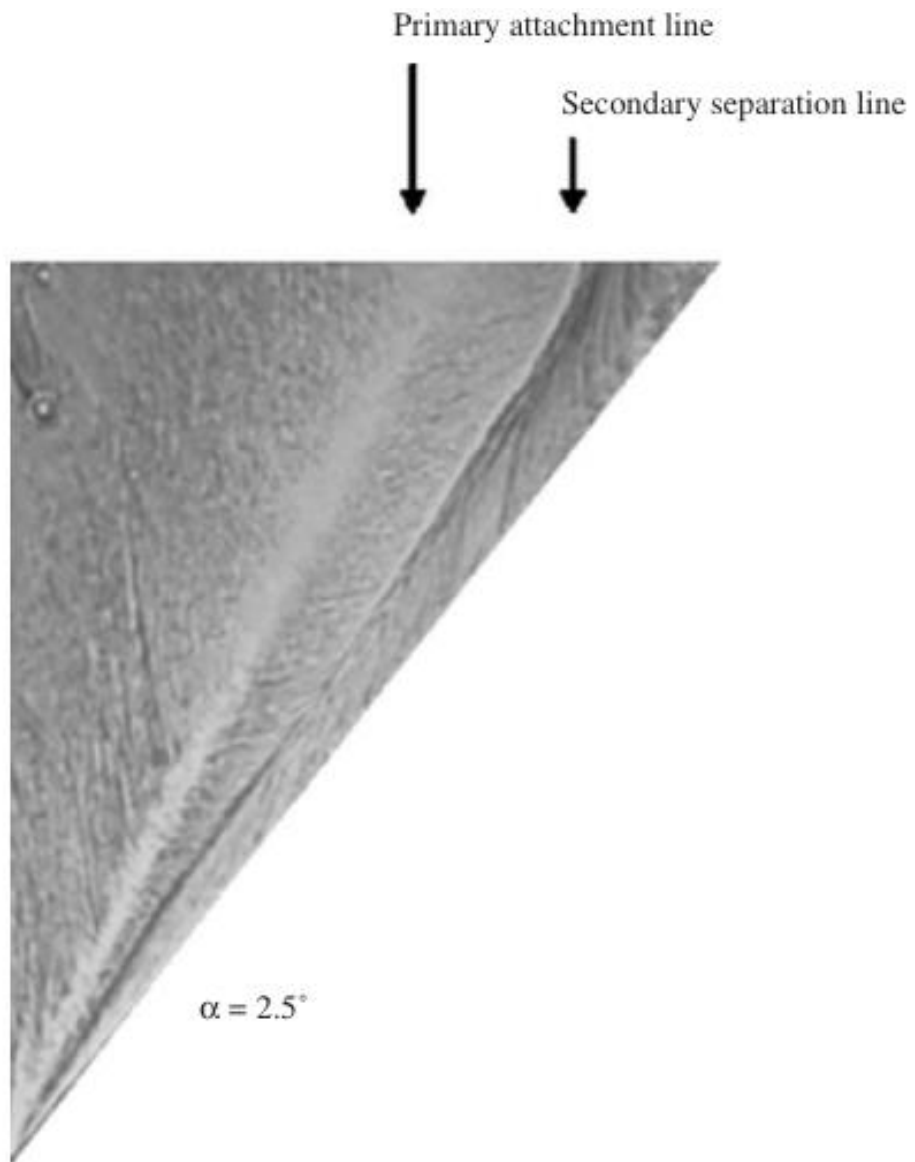


Figure 2.1 Surface oil flow visualization of the flow over a 50 degree sweep delta wing at an angle of attack 2.5 degree [4]

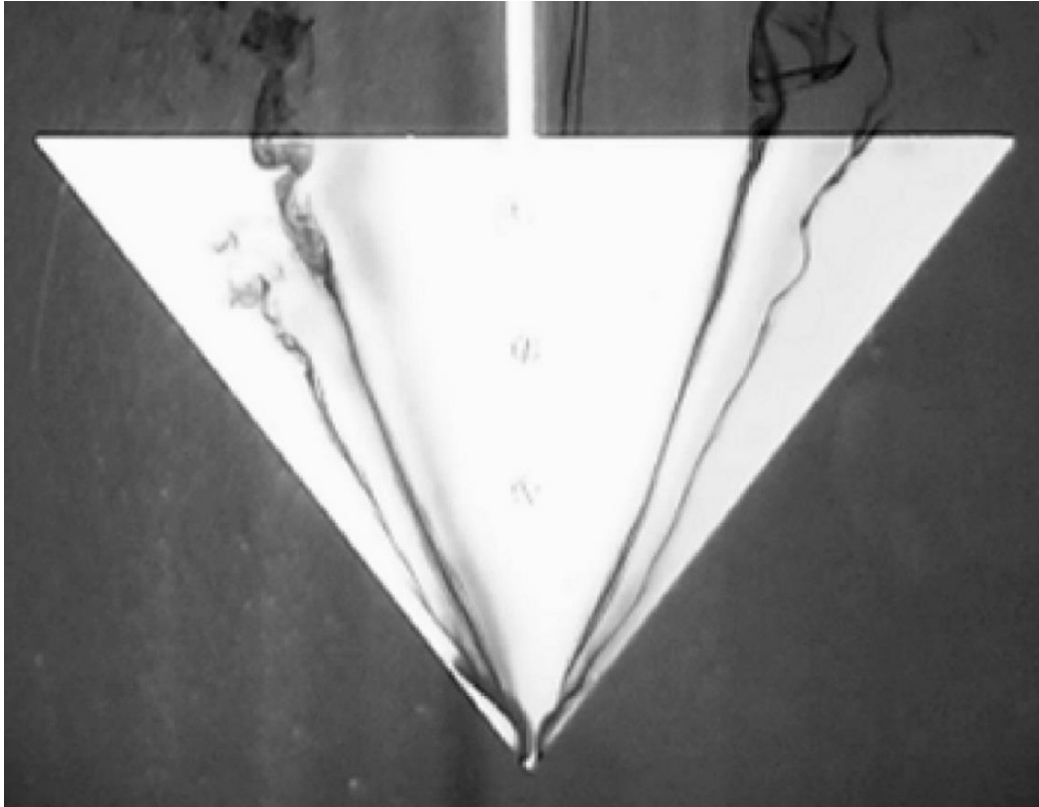


Figure 2.2 Dye flow visualization for vortex flow for  $\alpha = 5^\circ$  at  $Re = 8.7 \times 10^3$  in water tunnel experiments[50]

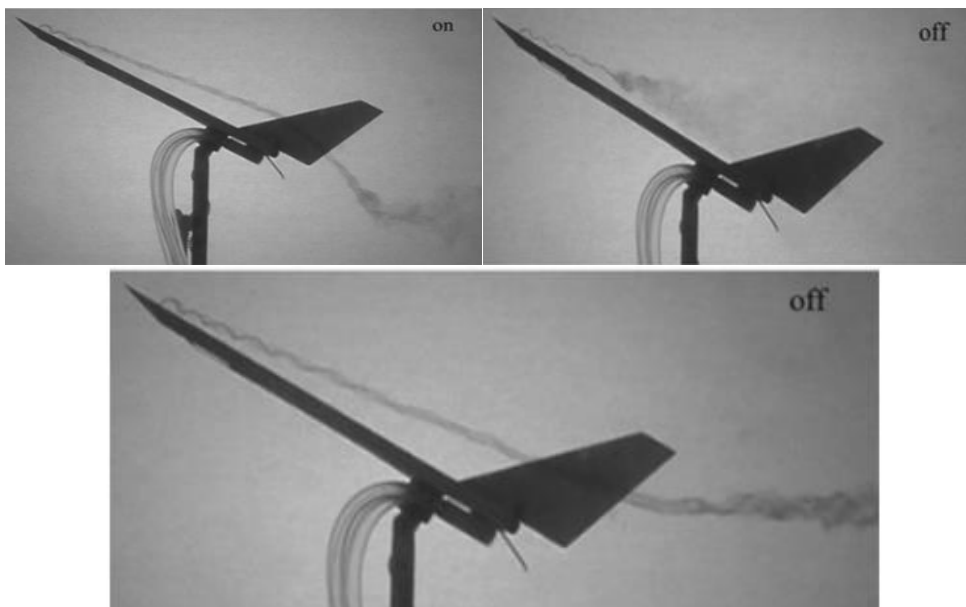


Figure 2.3 Flow visualization of leading-edge vortex for a) jet off, b) jet on, and c) just after the jet is turned off [47]

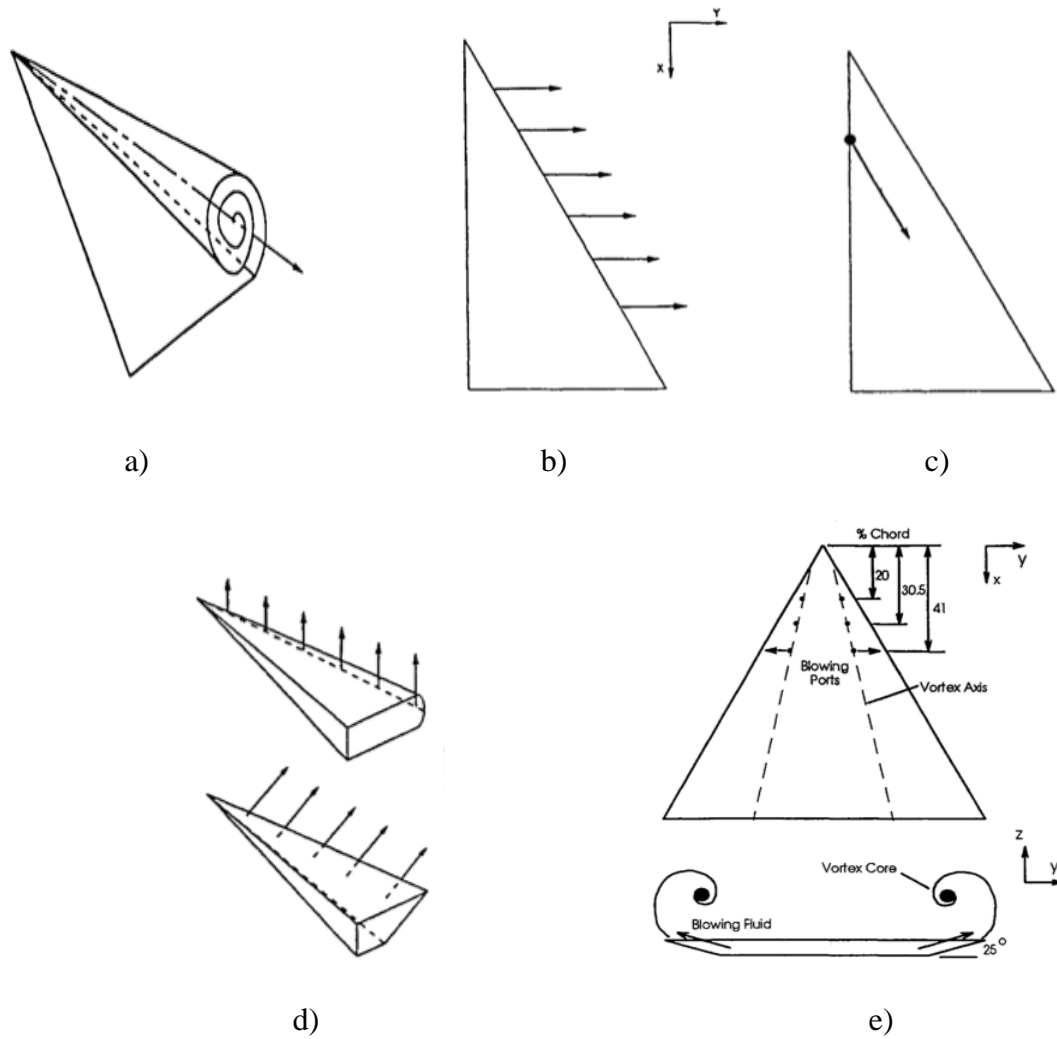


Figure 2.4 Vortex control techniques: a)VCB, b)SWB, c)PLEB d)TLEB, e)RASB

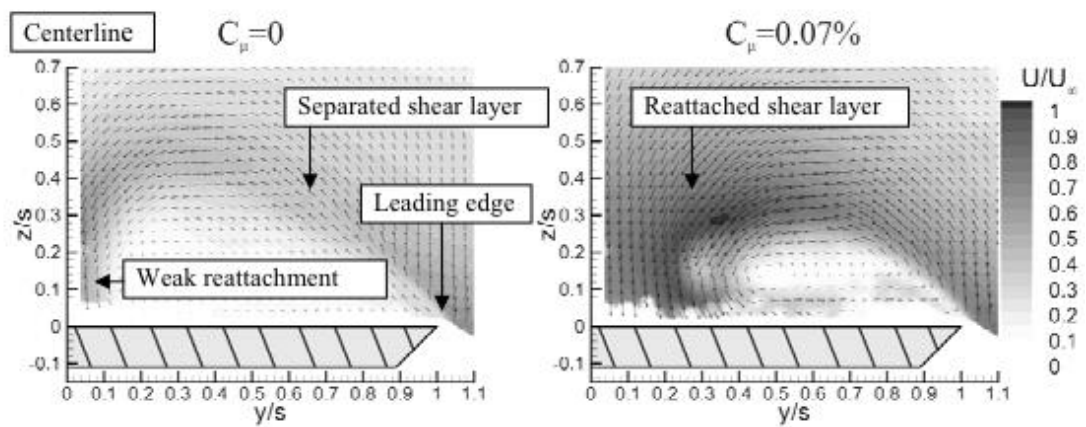


Figure 2.5 Magnitude of time averaged cross flow velocity at  $x/C=0.28$ , for  $St=1.3$  and  $\alpha=25^\circ$  [6]

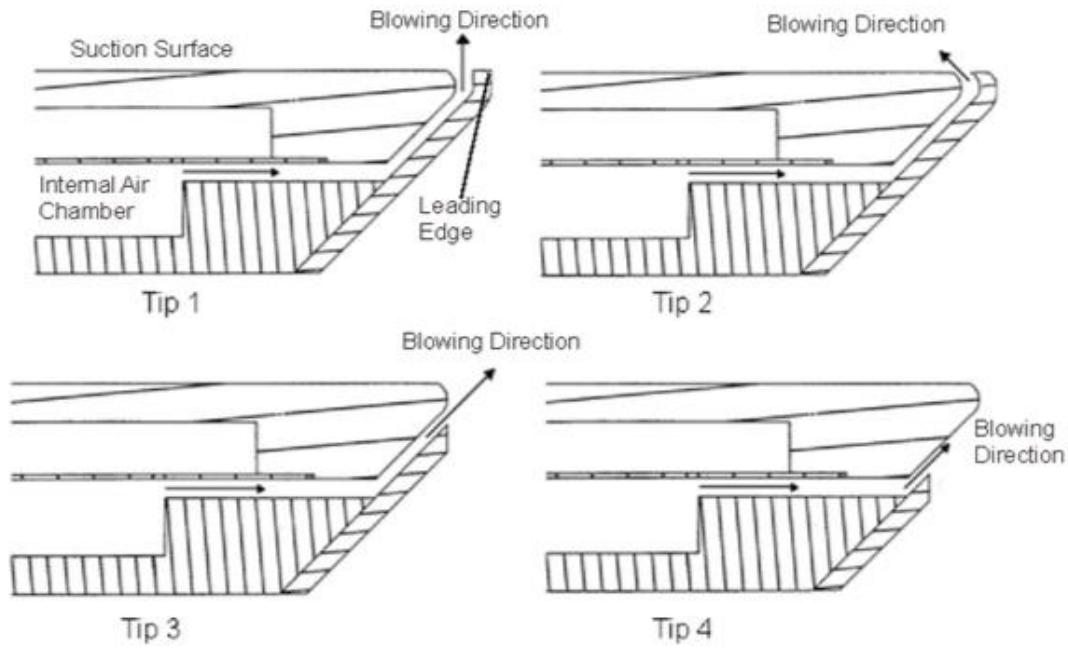


Figure 2.6 Section view of leading edge tip geometries tested[6]

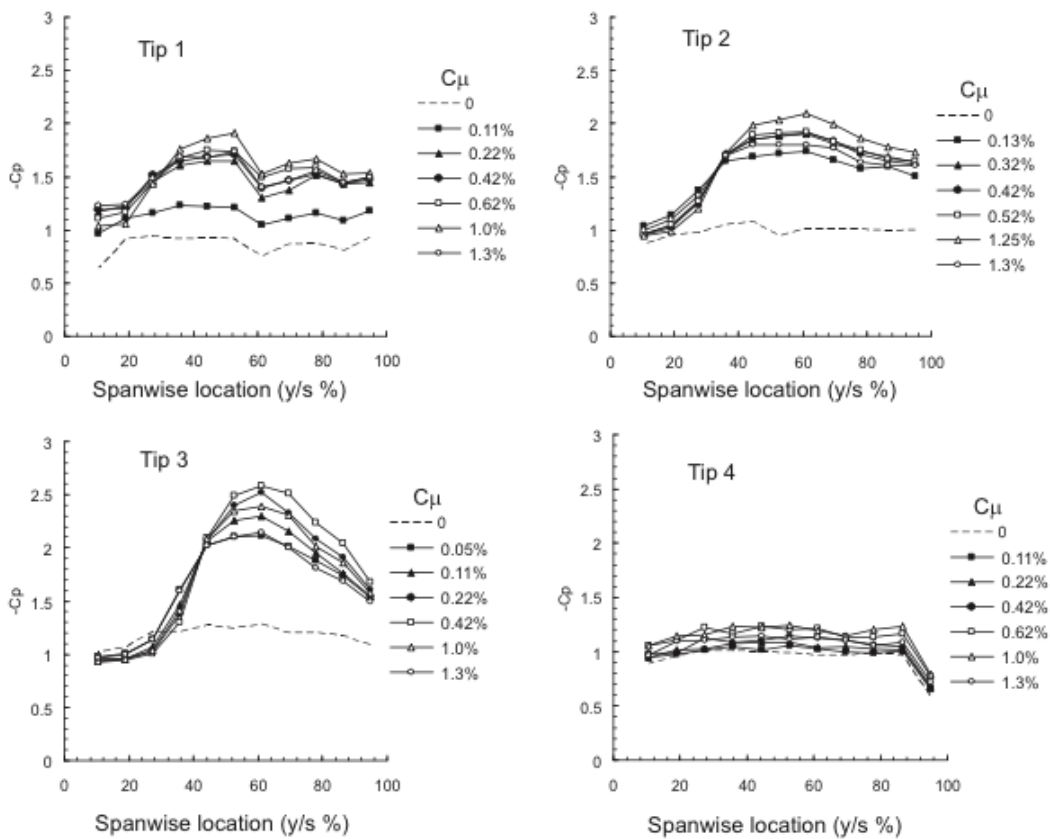


Figure 2.7 Comparison of unsteady blowing at a range of momentum coefficients from different leading edge tip profiles,  $\alpha = 25^\circ$ ,  $x/C = 0.28$ [6]

## CHAPTER 3

### EXPERIMENTAL SYSTEM AND TECHNIQUES

#### 3.1 Wind Tunnel

The experiments were conducted in a low speed, suction type, open circuit wind tunnel facility located at the Fluid Mechanics Laboratory of Mechanical Engineering Department at Middle East Technical University. The tunnel has a fully transparent test section, which has a dimensions of 750 x 510 x 2.000 mm. Figure 3.1 and Figure 3.2 depict the tunnel and fully transparent test section, respectively. The air passes through inlet sections, whereas turbulence screens and the honeycomb with screens are located to prevent the foreign objects and provide uniform flow. After the flow passes through inlets, it comes across with contraction cone, and is then accelerated with a 8:1 contraction ratio. The tunnel can provide a free stream velocity up to 30 m/s, however, tunnel was run in the range of 1.39 – 7.46 m/s, which correspond to desired Reynolds numbers 14000 and 75000, respectively. Reynolds number is calculated based on the wing chord length of 0.15 m. Figure 3.3 represents the experiment matrix including attack angles, Reynolds numbers, and the momentum coefficients used in the present study.

##### 3.1.1 Wind Tunnel Characterization

The velocity measurements of the tunnel were performed by Laser Doppler Anemometry (LDA) technique and Pitot - static tube pressure measurement using pressure scanner in order to obtain the calibration curve of the tunnel before the experiments conducted. Dynamic pressure data taken from Pitot – static tube give the corresponded velocities regarding temperature, humidity and the elevation of the laboratory. The average velocity of two different measurements is used as the

freestream velocity. The average velocities and the corresponding fan powers are tabulated in Table 3.1. Turbulence intensity has the utmost importance for wind tunnel experiments. Thus, the flow in the test section was traced by Laser Doppler Anemometry (LDA) method to determine the turbulence intensities in the test section at wide range of velocities. It is found that the turbulence intensities in the test section, which are tabulated in Table 3.2, do not exceed 1%. The calibration curve of the wind tunnel is shown in Figure 3.4. It is seen that the calibration curve is linear even at low velocities.

Table 3.1 Results of velocity measurements inside the test section at different fan powers.

<b>Fan Power (%)</b>	<b>4.5</b>	<b>10</b>	<b>15</b>	<b>20</b>	<b>25</b>	<b>30</b>	<b>35</b>	<b>40</b>	<b>45</b>	<b>50</b>	<b>55</b>	<b>60</b>	<b>65</b>	<b>70</b>	<b>75</b>
<b>Ave. Velocities in the Test Section (m/s)</b>	<b>0.41</b>	<b>1.86</b>	<b>3.14</b>	<b>4.47</b>	<b>5.75</b>	<b>7.12</b>	<b>8.42</b>	<b>9.77</b>	<b>11.11</b>	<b>12.48</b>	<b>13.72</b>	<b>15.24</b>	<b>16.69</b>	<b>17.81</b>	<b>19.32</b>

Table 3.2 Turbulence intensities that were measured via LDA in the test section at different velocities

<b>Velocity (m/s)</b>	<b>Turbulence Intensity (%)</b>
1.06	0.783
3.47	0.928
6.36	0.754
9.12	0.807
12.20	0.865
16.70	0.931
20.72	0.862

### 3.2 Delta Wing Model

The delta wing had a sweep angle of  $\Lambda=45^\circ$ , a chord of 150 mm and a span of 300 mm. The wing was made of polyamide PA2200. It had a thickness of 15 mm, and its leading edges were beveled at 45 degree on the windward side. A sketch that shows

the lower surface of the wing is given in Figure 3.5. The wing surface was painted to black to increase the visibility of smoke for qualitative measurement.

The wing dimensions were determined considering the test section dimensions of the wind tunnel and the blockage ratio of the prospective wing. The maximum blockage ratio was 1.6% for the angle of attack 16 degree, which was the highest attack angle used in this study.

The manufactured wing model had 54 pressure taps on the lower surface of the wing, which were evenly and symmetrically distributed. Pressure taps were positioned at three streamwise stations, corresponding to  $x/C=0.32$ ,  $0.56$  and  $0.80$ . Figure 3.5 represents the pressure taps and their locations on the wing surface. There were 6 blowing holes on the wing surface, which were located at  $x/C=0.16$ ,  $0.44$  and  $0.68$ . Blowing direction of the excitation was chosen parallel to the leading edge bevel angle, which was 45 degree. The cross section of the hole geometry at the leading edge is presented in Figure 3.6. To provide an efficient blowing, blowing holes were located closest point to leading edges as the wing geometry allows. Thus, a total of six blowing holes, three in each half of the wing, were located 1 mm inboard of the leading edges. Three different jet velocities were employed. Corresponding momentum coefficients are  $C_{\mu} = 0.005$ ,  $0.01$ ,  $0.02$ . The number of pressure taps and their locations at each station on the wing were determined to provide high resolutions at the experiments. To avoid significant disturbances on the flow structure due to the pressure taps, diameter of the taps were chosen as 0.5 mm due to the manufacturing resolution of the rapid prototyping machine. For smoke visualization, four smoke holes were positioned near the apex of the wing with 3 mm diameter each.

Rapid prototyping method was used to fabricate the highly complex geometry. Figure 3.7 represents CAD drawing of the wing used in the experiments. The wing used in this study was manufactured by EOSINT P380 3d Printer. The fabricated wing is depicted in Figure 3.8.

A mount for delta wing was designed and manufactured to provide a solid structure to prevent undesired disturbance in the flow field passing through delta wing. In

addition, mount was designed to give different angles of attack, yaw and roll angle and elevation as well.

### **3.3 Qualitative Flow Measurement – Laser Illuminated Smoke Visualization**

Laser illuminated smoke visualization was employed as a qualitative measurement technique. Laser illumination is simple and cheap technique to apply any experimental set-up such as wind tunnel. A suitable tracer particle for visualization needs to be selected depending on the experiment. Possible tracer particles are smoke and dye, which can be used in wind tunnel and water tunnel experiments, respectively.

Since the present study is conducted in wind tunnel facility, smoke is used as a tracer particle. Smoke is delivered by smoke generator, which provides a mixture of kerosene mist and pressurized CO<sub>2</sub> (carbon dioxide). Figure 3.9 illustrates the smoke generator used in experiments. Flow rate of the supplied smoke might disturb the flow structure, therefore flow rate is adjusted from the vane belongs to carbon dioxide tube.

The laser on its own is not enough for visualization experiments. Laser is supposed to have a sheet form to observe complex flow structures such as wakes, vortices and vortex breakdown. For this purpose, an optical equipment, cylindrical lens, was used to transform single point laser to sheet laser. Green laser with 532 nm wavelength and 400 mW power was implemented to the experimental set-up with a cylindrical lens. Lens could move separately, which made possible to use same laser sheet for either surface flow visualization or cross flow visualization. Cross flow images were taken at locations  $x/C=0.32$  and  $0.80$ , which correspond to first and second pressure tap stations. Canon 50D and Nikon 3100 Digital SLR cameras were used to capture surface flow and cross flow images. The shutter speed of the camera was varied within the range of  $1/30$  and  $1/200$ . For cross flow images, it was crucial to prevent disturbance in the flow field, hence a mirror was oriented with 45 degree angle far behind the delta wing. Figure 3.10 presents the orientation of wing, laser, camera and mirror in the test section. Camera was located under the test section for

surface flow visualization. Figure 3.11 depicts illustration of typical surface flow visualization from side view.

### **3.4 Quantitative Flow Measurement - Pressure Measurements**

Surface pressure measurements were carried out using a Netscanner 9116 Pressure Scanner, depicted in Figure 3.12, which consists of 16 silicon piezoresistive pressure sensors within the range of 0 – 2.5 kPa and includes temperature sensors. Pressure transducer has the processor in itself, which optimizes transducer's output for nonlinearity, sensitivity and thermal effects by using calibration and the temperature data recorded via pressure and temperature sensors. This processing leads transducer to reach  $\pm 0.003\%$  resolution with  $\pm 0.15\%$  static accuracy and  $\pm 0.0015\%$  total thermal error on full scale.

There were 54 pressure taps of 0.5 mm diameter on the windward side of the wing. 54 pressure taps were evenly and symmetrically distributed to the left and the right side of the wing. Figure 3.5 shows the locations of the pressure taps on the schematic of the wing. In order to confirm that symmetric pressure tap results do not differ from each other, preliminary measurements were conducted for all stations at different flow conditions such as at different Reynolds numbers and at different incidences. Results of these preliminary measurements showed a symmetrical structure in pressure distributions on the full wing. Hence, due to the reason of symmetric behavior of pressure taps, pressure measurements presented in this study were performed on the left half of the wing only. However, since there were 16 channels on pressure scanner, surface pressure measurements were divided into two parts and performed at different times. During the experiments, 5000 data (500 Hz for 10 seconds) were taken for each pressure tap, which is directly connected to the pressure scanner. Pressure taps, used and connected to the scanner, are illustrated in Figure 3.5.

Surface pressure measurements, obtained via pressure scanner, are presented as dimensionless pressure coefficient  $C_p$ , which are calculated by the formula given in Equation 3.1.  $C_p$  results represent pressure distribution on the wing surface at three different spanwise stations. All the calculated  $C_p$  values were plotted as  $-C_p$  distribution on the surface of the wing at the results chapter.

$$C_p = \frac{p - p_\infty}{\frac{1}{2} \rho u_\infty^2} = \frac{p - p_\infty}{p_{dyn.}} \quad (3.1)$$

- $p$  : Measured static pressure at an instant  
 $p_\infty$  : Static pressure of the flow  
 $p_{dyn.}$  : Dynamic pressure of the flow  
 $\rho$  : Density of the fluid  
 $u_\infty$  : Freestream velocity of the fluid in streamwise direction

### 3.5 Steady Blowing Setup

The blowing setup was built in order to provide steady air injection through the leading edges of the wing model. A schematic of flow control setup is given in Figure 3.13. Bosch Rexroth ED02 pressure regulator was used to activate air supply, which was connected to flow meters, data acquisition card and power supply. Pressure regulator was a pneumatic device and converted an electrical set point into pressure. Therefore, a pressure sensor was integrated in the pressure regulator to record outlet pressure. To operate the regulator, device was supplied with compressed air and 24 V DC voltage with a set point 0 V. Once the electrical and pneumatic supplies were connected, the pressure could be adjusted. The maximum pressure that could be supplied was 8 bars, and the outlet pressure range was 0 to 6 bar as the set point voltage was varied. A virtual instrument user interface was built in Labview program to be able to adjust the output voltage of the NI 9263 analogue output DAQ card to control the flow rate of the blowing. The volumetric flow rate of the injected air through the each blowing hole location was controlled by three separate rotameters located just after the pressure regulator. The steady blowing cases are characterized by the dimensionless momentum coefficient, which can be defined as the ratio of the momentum of the added flow to the free stream momentum on the wing. It is an expression of the energy amount added to the flow field. In this study, three different momentum coefficients,  $C_\mu = 0.005, 0.01$  and  $0.02$

were tested for three different blowing patterns, uniform blowing, descending blowing, and ascending blowing. The decision on selected momentum coefficients were based on the preliminary experiments and a study conducted recently [19]. Moreover, it is essential to stay in the practical range of momentum coefficients for real applications. The momentum coefficients were calculated as in the following Equation 3.2.

$$C_{\mu} = \frac{Q_J V_J}{U_{\infty}^2 A_S} \quad (3.2)$$

- $Q_J$  : Steady blowing mean flow rate
- $V_J$  : Steady blowing jet velocity
- $U_{\infty}$  : Free stream velocity
- $A_S$  : Wing planform area

The sketch of different blowing patterns, which are used in the experiments, is given in Figure 3.14. Three identical circular blowing holes are located at three different chordwise locations on the suction side, which provide the possibility to compare different blowing patterns. The decision on the dimension and the quantity of the holes were based on the many parameters including the wing dimensions, available space in the wing body to provide blowing, desired momentum coefficients, and some other practical issues. Uniform blowing pattern provides 1/3 of total momentum from each hole. In decreasing blowing pattern, momentum decreases from apex through the trailing edge with the ratios of 6/9, 2/9 and 1/9, for each blowing location, respectively. In increasing blowing pattern, conversely, momentum increases from apex through the trailing edge with the ratios of 1/9, 2/9 and 6/9, for each blowing location, respectively. In order to achieve the required momentum coefficients and blowing patterns, the rotameters, which had the ranges of 0-0.1, 0.1-1 and 3-15 liter per minute, were installed. Rotameter was able to provide desired flow rate by the adjustable vane on it.

In order to verify the blowing flow rate in achieving the correct momentum coefficient, the velocity at the exit of the blowing hole was measured using a pitot static tube. The measurement was performed with a spatial resolution of 1 mm starting from the closest distance to the hole for Reynolds number 35000 at dimensionless momentum coefficient of 0.01. For this case, the calculated velocity at the exit of the hole is 14.9 m/s. The measurement results are presented in Figure 3.15. Due to the blockage, very high velocities are detected as the probe advances toward the blowing hole. The studies in literature, which have the Reynolds number based on the hole diameter close to the present study, states that the hole exit velocity should stay approximately constant up to the distance of 4 times the exit hole diameter[51], [52]. As indicated in Figure 3.15, that distance corresponds to 8 mm which reads the velocity close to the calculated value. Furthermore, recent measurements performed with hot wire anemometry also confirms that the hole exit velocity is around the calculated value of 14.9 m/s for the corresponding momentum coefficient and the Reynolds number [53].

### 3.6 Experimental Uncertainty Analysis

It is always possible to encounter with errors in experimental measurements. In order to collect reliable data from the experiments, uncertainty analysis should be used for validity. There are two types of errors, which are fixed and random error. Fixed errors can be eliminated by calibration. However, random errors are not predictable and differ at each measurement due to their nature.

The aim of uncertainty analysis is to estimate random errors in the experiments with three procedures. Firstly, the uncertainty interval of each quantity should be estimated. Secondly, confidence limits on each measurement should be defined. Lastly, propagation of uncertainty into results from data collected should be analyzed.

When the measured value is reported, the value  $X$  is written as follows;

$$X = X_{best} \pm \Delta X \quad (3.3)$$

where  $X_{best}$  is best estimate of measured parameter and  $\Delta X$  is the uncertainty in the measurement

Equation 3.4 can be defined as

$$X = X_{best} \left[ 1 \pm \left( \frac{\Delta X}{X_{best}} \right) \right] \quad (3.4)$$

where the ratio of  $\Delta X$  to  $X_{best}$  is called as fractional uncertainty. But most of the cases fractional uncertainty is multiplied by 100 and reported as percent uncertainty. Since, current calculations include complex operations compared to simple addition or multiplication processes, a more functional rule should be considered for calculation of  $C_p$  and  $C_\mu$ , which are basic parameters of current study. When the calculated quantity  $q$  is a function of the measured values  $a, b, \dots, z$  with uncertainties  $\Delta a, \Delta b, \dots, \Delta z$ , total uncertainty becomes

$$\Delta q = \left( \left( \frac{\partial q}{\partial a} \Delta a \right)^2 + \left( \frac{\partial q}{\partial b} \Delta b \right)^2 + \dots + \left( \frac{\partial q}{\partial z} \Delta z \right)^2 \right)^{\frac{1}{2}} \quad (3.5)$$

Equation 3.4 states that each measured value goes into determination of  $q$ . The first term in the equation represents the uncertainty that  $a$  contributes to the total uncertainty  $q$ . Each subsequent describes the uncertainty contributed by other measurement values. Additionally, it should be noted that exact number or constant such as  $2, \pi, \text{ and } g = 9.81 \text{ m/s}^2$  do not contribute to the uncertainty mentioned above.

For this purpose, the experimental uncertainty analysis is outlined in Table 3.3 and Table 3.4. Table 3.3 presents the pressure coefficient uncertainty arises due to accuracy of pressure transducer and manometer. Table 3.4 summarizes the uncertainty of momentum coefficient. In order to calculate uncertainty analysis for different blowing scenarios, MATLAB software is used. Source codes are presented in Appendix B. Sample scenario chosen for Table 3.3 and Table 3.4 is at  $\alpha = 7^\circ$  and  $Re=35000$  with  $C_\mu = 0.01$ . The calculated relative uncertainty is presented in Table 3.5 for different Reynolds numbers. The results confirm that high uncertainty is encountered at low Reynolds number.

Table 3.3 Summary of pressure measurement uncertainty

Quantity	Uncertainty	Measurement Technique	Factors
Freestream Dynamic pressure	0.07%	Measured directly - Netscanner 9116 Pressure Scanner connected to a pitot- static tube	Scanner accuracy (0.05%)
Pressure tap Reading, $p$	0.05%	Measured directly - Netscanner 9116 Pressure Scanner	Scanner accuracy (0.05%)
Static pressure of the flow, $p_{\infty}$	0.05%	Measured directly - Netscanner 9116 Pressure Scanner	Scanner accuracy (0.05%)
Pressure coefficient  $C_p = \frac{p - p_{\infty}}{p_{dyn.}}$	0.66%	Uncertainty calculated from freestream dynamic pressure and pressure tap reading	

Table 3.4 Summary of momentum coefficient uncertainty

Quantity	Uncertainty	Measurement Technique	Factors
Freestream Dynamic pressure	0.07%	Measured directly - Netscanner 9116 Pressure Scanner connected to a pitot-static tube	Scanner accuracy (0.05%)
Jet hole diameter	0.05%	Measured directly - Netscanner 9116 Pressure Scanner	Scanner accuracy (0.13%)
Wing Chord	0.05%	Measured directly with ruler	Minimum step of the ruler
Wing span	0.05%	Measured directly with ruler	Minimum step of the ruler
Flow rate	5%	Measured by Flowmeter connected to valve	Deviation of measurement device
Momentum coefficient  $C_{\mu} = \frac{Q_J V_J}{U^2 A_S}$	10.6%	Uncertainty calculated from jet hole diameter, wing area and flow rate	

Table 3.5 Relative uncertainty at different Reynolds numbers

<b>Reynolds Number</b>	<b><math>X_{C_p}</math></b>	<b><math>X_{C_\mu}</math></b>
20000	0.10	0.12
35000	0.07	0.10
75000	0.01	0.10



Figure 3.1 The low speed wind tunnel facility used in this study



Figure 3.2 Optically transparent test section

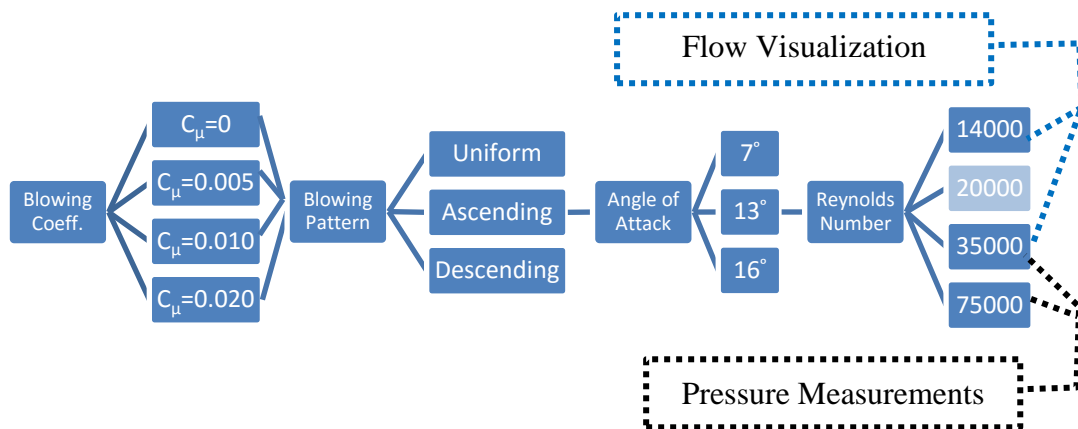


Figure 3.3 Experiment matrix

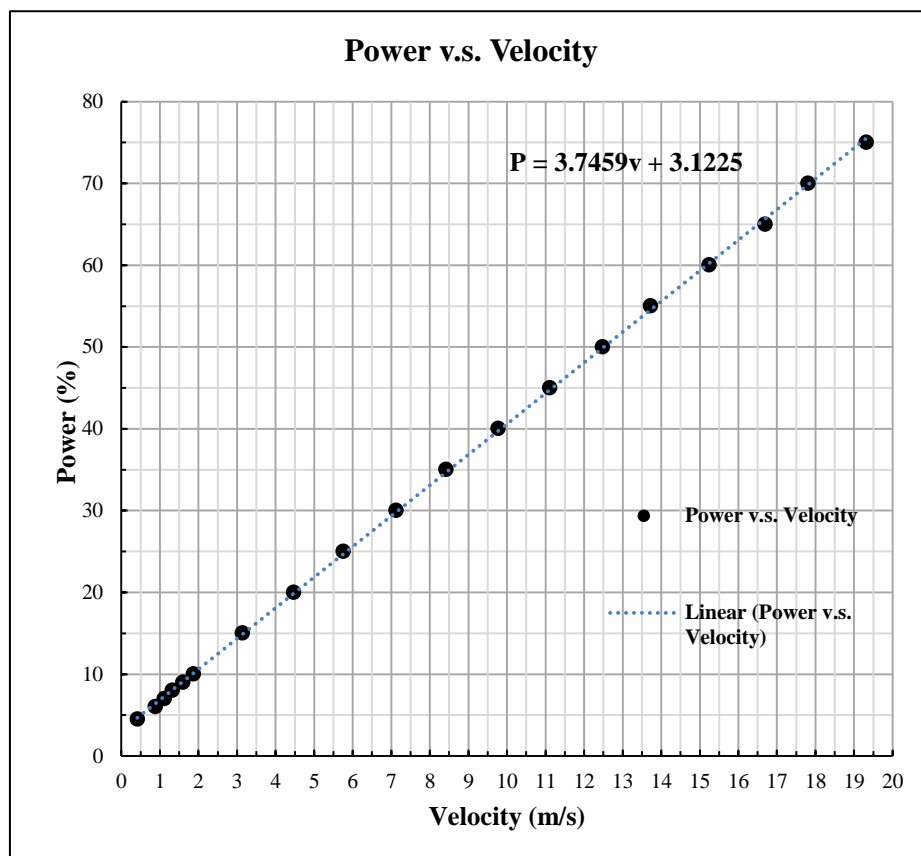


Figure 3.4 Calibration curve of the wind tunnel for obtaining the required fan power for a given velocity

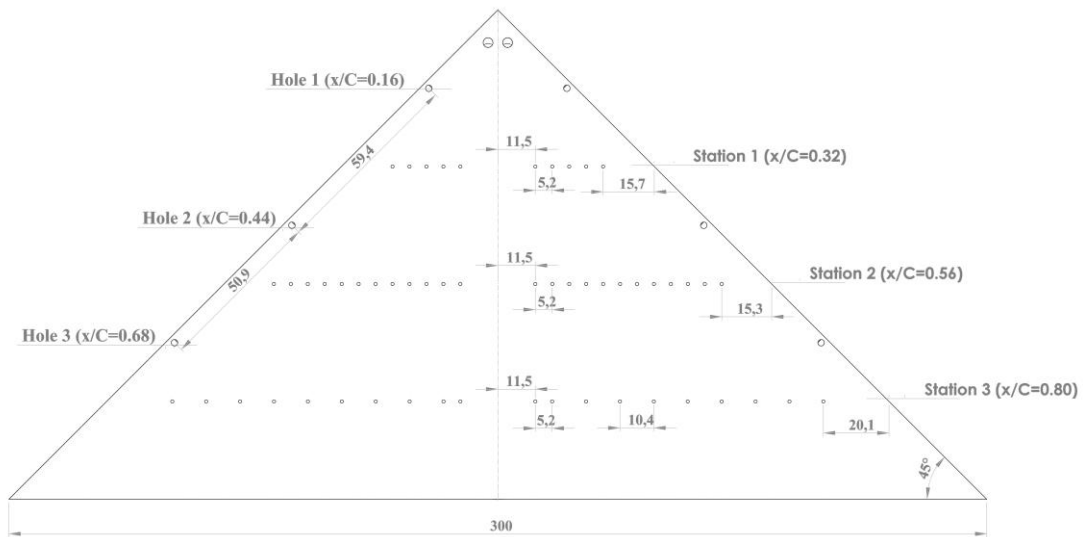


Figure 3.5 Plan view of the delta wing showing pressure taps located at the three chordwise stations and blowing holes at leading edges

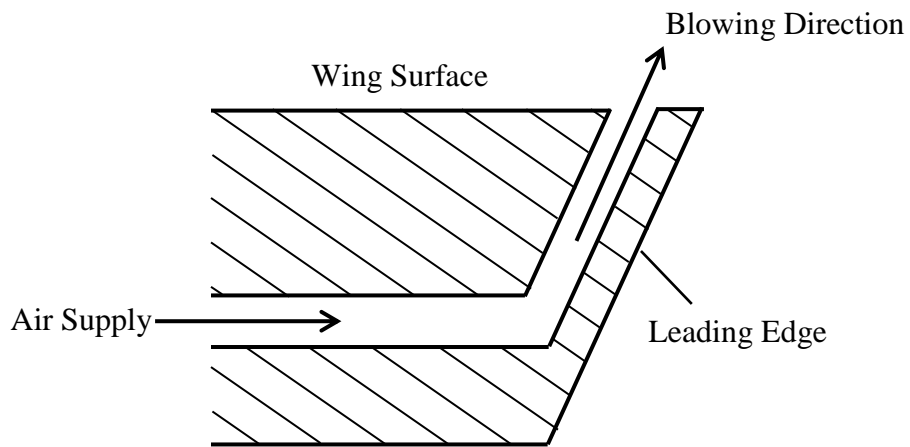


Figure 3.6 Cross-section view of blowing hole

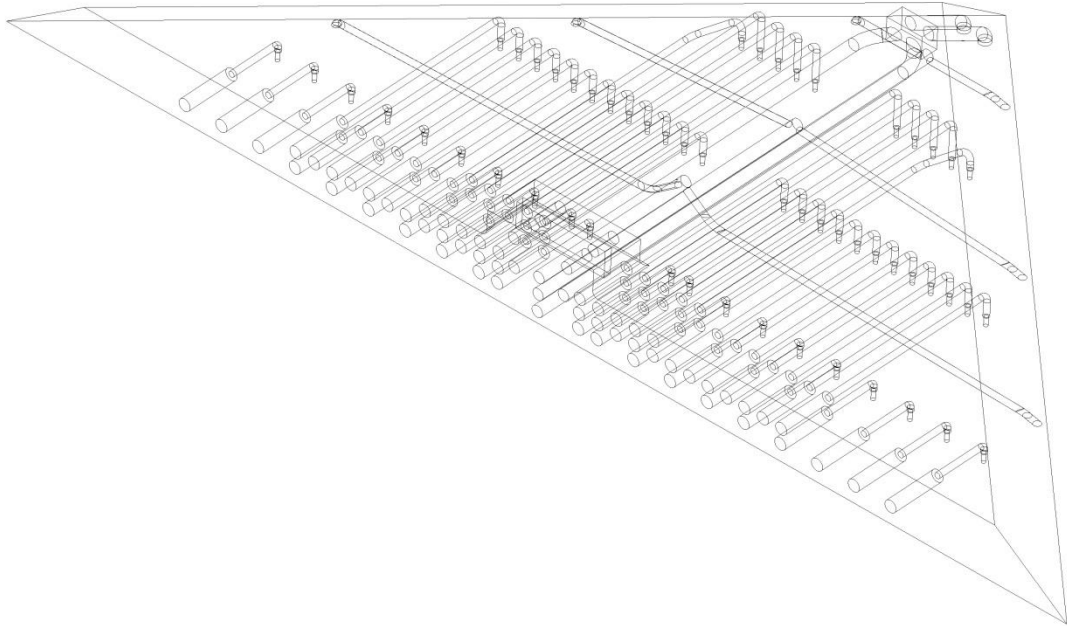


Figure 3.7 CAD drawing of the fabricated delta wing



Figure 3.8 Photographs of the fabricated delta wing from different views; a) Top-back view, b) Bottom view, which also shows the pressure taps that were used in pressure measurements



Figure 3.9 The smoke generator used in experiments (Plint&Partners Como3694)

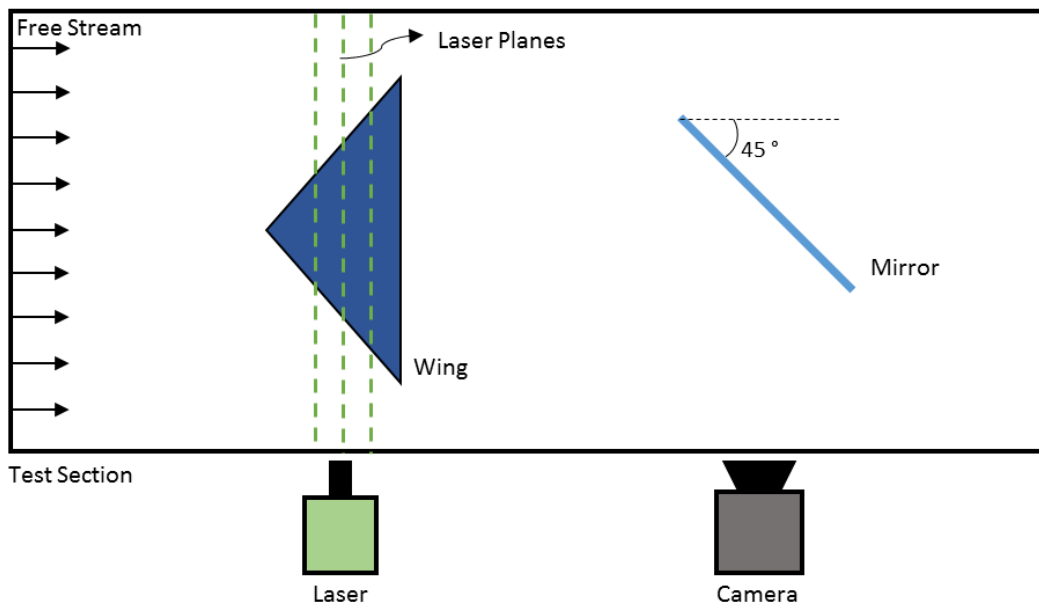


Figure 3.10 Experimental set-up for flow visualization at cross-flow planes  $x/C=0.32$ ,  $0.56$  and  $0.80$  (plan view)

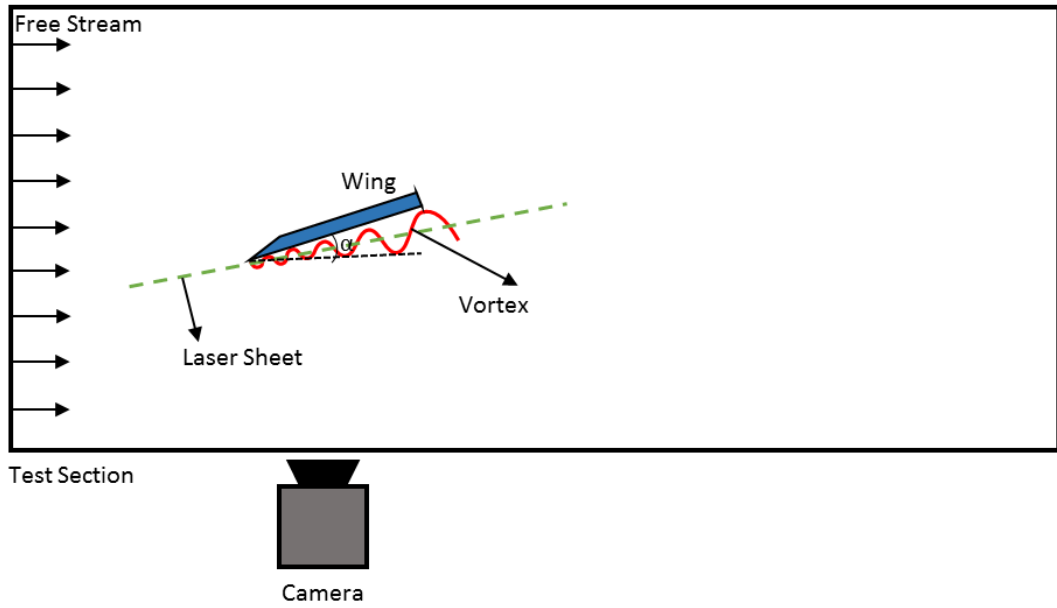


Figure 3.11 Experimental set-up for flow visualization at a plane parallel to the leading edge vortices (side view)



Figure 3.12 The 16-channel pressure scanner system used in the experiments (Netscanner 9116)

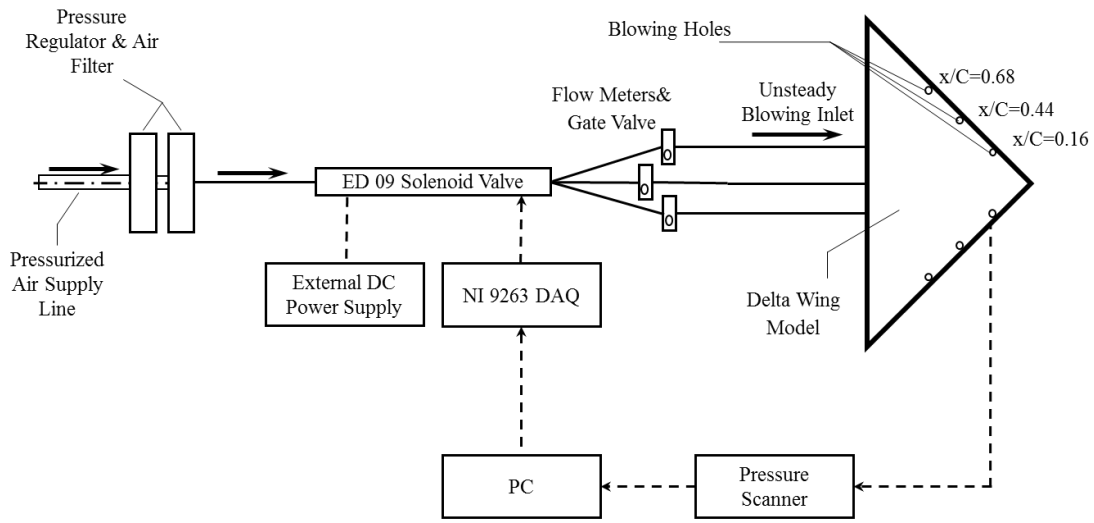


Figure 3.13 Schematic of control setup

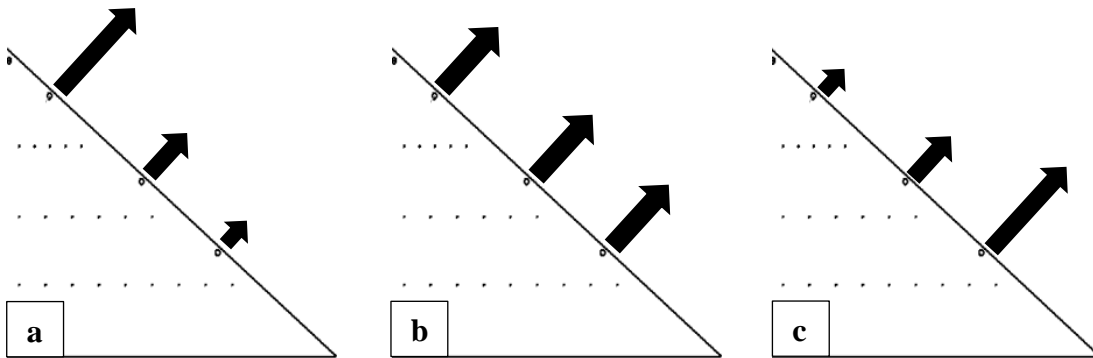


Figure 3.14 Schematic of different flow control patterns; a) descending, b) uniform, c) ascending

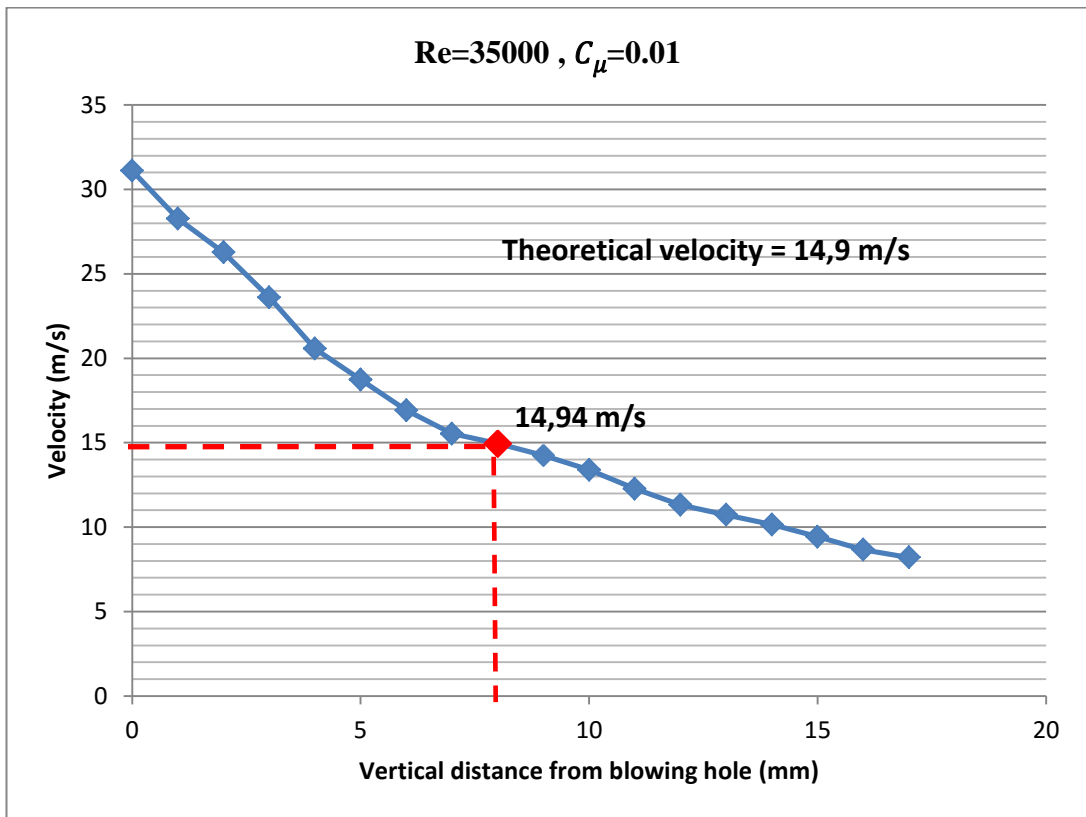


Figure 3.15 Velocity measurement at the exit of the jet hole.



## CHAPTER 4

### RESULTS AND DISCUSSION

This chapter mainly includes the results of the experiments conducted in the present study. First, the surface flow and the cross flow visualizations are given and discussed in detail, then the results of the surface pressure measurements are reported.

#### 4.1 Results of Surface Flow Visualization

The results of the surface flow visualizations are presented in Figures 4.1-4.6. Surface flow visualization experiments are conducted at Reynolds numbers of  $Re=14000$  and  $35000$  for attack angles of  $7$ ,  $13$  and  $16$  degrees. Figures are constructed in order to identify the effect of the flow control technique on the flow structure, such that each figure is assigned to a single attack angle and a single Reynolds number. In each figure, the results of the steady blowing cases at momentum coefficients of  $C_\mu = 0.005$ ,  $0.01$  and  $0.02$  are demonstrated along with the results of the no control case. The columns of the figures are constructed to show different blowing patterns, i.e. from left to right descending, uniform and ascending patterns.

Figure 4.1 represents surface flow visualization results for Reynolds numbers  $14000$  at an angle of attack  $7$  degree with different blowing patterns. The image of no blowing case represents a pair of dual leading edge vortices with the indication of the vortex breakdown over the wing surface. For descending blowing pattern, by increasing the momentum coefficient to  $C_\mu = 0.005$ , the location of the vortex breakdown is shifted toward the wing apex, where the spatial extend of the vortices are increased in spanwise distance. Increasing the momentum coefficient to  $C_\mu = 0.01$ , causes further movement of the vortex breakdown location toward the wing

apex. Considering  $C_\mu = 0.02$ , there is no noticeable change in the flow structure compared to the  $C_\mu = 0.01$  in surface flow visualization. For uniform blowing pattern, it is seen that increasing the momentum coefficient causes the deterioration in vortical structure and moves the vortex breakdown location upstream. However the burst level in the vortex breakdown region is not as strong as in descending blowing pattern. For ascending blowing pattern, increasing the momentum coefficient also leads to movement of the vortex breakdown location through the wing apex. Considering the all blowing patterns for this figure, the flow structure in the no control case does not benefit from the leading edge blowing technique instead axial extend of the flow field is dominated by vortex breakdown. However, the negative effect on the flow structure for ascending blowing pattern is minimal compared to the other patterns performed.

Figure 4.2 represents surface flow visualization results for Reynolds number 35000 at an angle of attack 7 degree with different blowing patterns. For no control case, leading edge vortices still exist and vortex breakdown is witnessed almost at the half chord distance of the planform. As previously discussed for Reynolds number 14000 case shown in Figure 4.1, for descending blowing pattern, increase in momentum coefficient does not postpone the occurrence of the vortex breakdown instead moves breakdown location toward upstream. For each blowing coefficient, the surface flow visualization results appear in a similar fashion. Similarly for uniform and ascending blowing patterns, excitations have adverse effects on the flow structure. For this figure, there is no clear evidence in the surface flow visualizations for the impact of the different blowing patterns on the flow structure.

Figure 4.3 represents surface flow visualization results for Reynolds number 14000 at an angle of attack 13 degree. The result of no blowing case indicates a fully separated flow over the wing surface. A pair of large-scale swirls dominates the wing planform. For descending blowing pattern, by increasing the momentum coefficient to  $C_\mu = 0.005$ , a recovered flow structure is obtained for which the spatial extent of the swirl level reduces and moves toward the wing apex. With injection of  $C_\mu = 0.01$ , a pair of leading edge vortices starts to develop with axial flow in the core at the proximity of the wing tip and the vortex breakdown location become apparent. Vortex breakdown starts to move downward and shrinks the size of vortical structure

at each side with further increase in momentum coefficient. For uniform blowing pattern, momentum coefficient  $C_\mu = 0.005$  leads to a decrease in the size of separated flow. With further increase in momentum coefficient three-dimensional separated flow starts to accumulate at the wing apex. When the amount of blowing momentum coefficient is set to 0.02, formation of leading edge vortices and its breakdown become evident over the wing surface. For ascending blowing pattern, likewise descending ordered blowing, swirl pattern gets closer to the wing tip. With momentum coefficient  $C_\mu = 0.01$ , steady blowing gives a rise to leading edge vortices. Further increase in momentum coefficient results in vortex breakdown over the wing surface.

Figure 4.4 represents surface flow visualization results for Reynolds number 35000 at an angle of attack 13 degree. The image of no blowing case represents a vortex breakdown near the apex. For descending blowing pattern, when the excitation is applied, no significant change is witnessed up to  $C_\mu = 0.01$ . Further increase in momentum coefficient moves vortical structure toward the leading edge with a vortex breakdown at the tip of the wing. Similarly for uniform and ascending blowing pattern, the vortex breakdown is observed at the apex of wing and no significant change is witnessed when the momentum coefficient is increased up to 0.01. Further increase in momentum coefficient results in movement of vortical structures through the leading edges.

Figure 4.5 represents surface flow visualization results for Reynolds number 14000 at an angle of attack 16 degree with different blowing patterns. The result of no blowing case illustrates a fully separated flow over the wing surface. For descending blowing pattern, fully separated flow is enhanced when the momentum coefficients are set to  $C_\mu = 0.005$  and  $C_\mu = 0.01$ , which provide smaller swirling pattern on the wing surface. However, increase in momentum coefficient promises a shift toward the tip of the wing and maybe leading edge vortices, it does not give a rise to vortex and its breakdown. Similarly for uniform and ascending blowing pattern, leading edge steady blowing seems to be sufficient which corresponds that three dimensional separated flow accumulates to the apex of the wing. However, early accumulation is observed at descending ordered blowing pattern compared to uniform ordered and ascending ordered blowing patterns.

Figure 4.6 represents surface flow visualization results for Reynolds number 35000 at an angle of attack 16 degree with different ordered blowing patterns. No blowing case shows a fully separated flow over the wing surface. For descending blowing pattern, at  $C_\mu = 0.005$ , there can be seen a decrease in the size of separated flow structure. Further increase in momentum coefficient delays separated flow structure and the level of swirls are reduced. When the momentum coefficient is set to  $C_\mu = 0.02$ , formation of vortical structure is witnessed. For uniform blowing pattern, likewise descending ordered blowing pattern, swirl structure gets closer to the wing tip. With further increase in momentum coefficient, which corresponds to  $C_\mu = 0.02$ , does not give a rise to vortical structure. For ascending blowing pattern, separated flow has a good response, when the momentum coefficients are  $C_\mu = 0.005$  and  $C_\mu = 0.01$ , which provides a smaller swirling pattern on the wing surface. Further increase in momentum coefficient represents the imprints of the vortex on the surface of the wing.

#### 4.2 Results of Cross Flow Visualization

Figures 4.7, 4.8, 4.9 and 4.10 show cross flow visualizations of half planform at different momentum coefficients for attack angles of  $\alpha = 7^\circ$  and  $13^\circ$ . Results are presented for uniform ordered blowing pattern at Reynolds numbers 14000 and 35000. For each figure, two columns of the figures represent the results for chordwise distance of  $x/C = 0.32$  and  $x/C = 0.80$ , which corresponds to 1<sup>st</sup> and 3<sup>rd</sup> station, respectively. Each row represents different momentum coefficient and is constructed in increasing order. Figure 4.7 represents cross flow visualization results for Reynolds number 14000 at an angle of attack 7 degree with uniform ordered blowing pattern. At  $x/C = 0.32$ , the image of no blowing case represents a pair of dual leading edge vortices without an indication of vortex breakdown at first station end view plane; however secondary vortices seem to be less intensive compared to inboard primary vortices. When the third station end-view is considered, it is witnessed that breakdown of secondary vortex and primary vortex occur before they reach to this plane. When steady excitation with momentum coefficient  $C_\mu = 0.005$  is applied at uniform blowing pattern at  $x/C = 0.32$ , it is seen that the momentum coefficient causes the decay in vortical structure and moves the vortex breakdown

location toward the wing apex. Further increase in momentum coefficient has adverse effects on the flow structure. At  $x/C = 0.80$ , increase in momentum coefficient to  $C_{\mu} = 0.01$  and  $C_{\mu} = 0.02$ , flow structure starts to disperse and covers wider range on this plane. Considering the all momentum coefficients for this figure, the flow structure in the no control case does not benefit from the leading edge blowing technique instead vortex moves toward leading edge and increases its scale.

Figure 4.8 represents cross flow visualization results for Reynolds number 35000 at an angle of attack 7 degree with uniform ordered blowing pattern. For no blowing case, at  $x/C = 0.32$ , due to the upward movement of vortex breakdown location, the dual vortex structure does not take place. Secondary vortex becomes fully dispersed. Further movement of downstream, at  $x/C = 0.80$ , illustrates that all the vortical structures become dispersed and no leading edge vortices are evident in the flow field. When steady excitation with momentum coefficient 0.005 is applied at uniform blowing pattern, no enhancement is observed at  $x/C = 0.32$  and  $x/C = 0.80$ , The flow has a similar structure at each end-view plane with decrease in its intensity. Further increase in momentum coefficient results in increase in height of flow structure at each cross plane and vortex moves toward leading edge

Figure 4.9 represents cross flow visualization results for Reynolds number 14000 at an angle of attack 13 degree with uniform ordered blowing pattern. At first station, the image of no blowing case represents three-dimensional separation from wing surface. Leading edge vortices do not appear in the flow anymore. When the third station end-view is considered, it is witnessed that vortical structure, encountered in the first end view plane, is also evident at this plane. When steady excitation with momentum coefficient 0.005 is applied at uniform blowing pattern, no noticeable change in the flow structure is seen, however, according to surface flow visualization results one can say that there can be seen a decrease in the size of separated flow. With further increase in momentum coefficient to  $C_{\mu} = 0.01$ , three-dimensional separated flow starts to accumulate of the wing apex. Formation of leading edge vortices can be seen from the image of the cross flow results. When the amount of blowing momentum coefficient is set to 0.02, leading edge vortex and its breakdown become evident considering the end view images at different cross flow planes.

Figure 4.10 represents cross flow visualization results for Reynolds number 35000 at an angle of attack 13 degree with uniform ordered blowing pattern. At  $x/C = 0.32$ , the image of no blowing case depicts separated shear layer from leading edges. It is not possible to observe vortical structures in the flow field. When the third station end-view is considered, vortical structure is not visible and is also fully dispersed. When steady excitation is applied at uniform blowing pattern, no significant change is witnessed for all end view planes. However, as the momentum coefficient is increased the reattachment location moves outboard of the wing centerline.

### 4.3 Pressure Measurements

In this part of the thesis, results of the surface pressure measurements are presented from Figures 4.11 to 4.16 for three different attack angles 7, 13 and 16 degrees at Reynolds numbers of 35000 and 75000. Due to the high uncertainty level at lower Re numbers, results of pressure measurements at  $Re=20000$  for angles of attack 7, 13 and 16 degrees are demonstrated in Appendix C as Figures C1, C2 and C3, respectively and not discussed in detail. Figures are constructed to show the effect of leading edge blowing in the flow structure, such that each figure corresponds to a single attack angle and a single Reynolds number case. The rows represent the different chordwise locations of  $x/C = 0.32, 0.56$  and  $0.80$ , respectively. The three columns of the figures are assigned to show different blowing patterns, i.e. from left to right descending, uniform and ascending patterns. The mean pressure distribution against dimensionless spanwise distances, are plotted for each cases. Horizontal axis of the each plots represent  $y/s$  the dimensionless spanwise distance from the root chord of the wing. The dimensionless pressure coefficient  $C_p$  was calculated in order to plot the mean pressure distribution for which the details are given in previous chapter. MATLAB software is used to calculate and plot  $C_p$  values. Appendix A represents the source codes to process raw data taken from the computer. Vertical axis of the plots represents  $-C_p$  values. The distribution of the pressure coefficient  $C_p$  is a useful tool that identifies the vortical structure of the flow on the wing, which helps to understand general aerodynamic performance of the delta wings. High  $-C_p$  values means high suction region and low  $-C_p$  values means that the flow reattachment occurs. Footprints of vortex structure are clearly visible at all angles of

attack as the suction peaks are observed in Figures 4.11 – 4.16. These suction peaks point the axis of leading edge vortex and also have a match with smoke visualization results. And it is also seen that suction peaks lean to reduce with downstream movement as a result of increase of distance between flow structure and wing surface in the same direction. As it is seen from the steady pressure measurement figures that the suction peaks broadens, and the vortex core axis and the reattachment line moves inboard of the wing toward the centerline with increasing the angle of attack.

Figure 4.11 presents the results of the experiments at angle of attack 7 degrees for Re 35000. Pressure distributions at all stations regardless of blowing patterns almost show similar trend. At  $x/C=0.32$ , highest  $-C_p$  values can be reached at highest momentum coefficient, however lowest  $-C_p$  values can be reached at lowest momentum coefficient. It is hard to observe significant difference considering which blowing pattern provide best enhancement for the pressure distribution. At  $x/C=0.56$ , the effect of momentum coefficient 0.02 is evident at any blowing pattern in terms of increasing the  $-C_p$  value whereas blowing in lower momentum coefficients seems to be ineffective on the flow structure. At  $x/C=0.80$ , effect of blowing is hardly seen.

Figure 4.12 presents the results of the experiments at angle of attack 7 degrees for Re 75000. At  $x/C=0.32$ , ascending ordered pattern seems to be more effective regarding momentum coefficient range reached, which is the highest at this pattern. Effect of descending and uniform pattern are not as good as ascending blowing pattern. At  $x/C=0.56$  and  $x/C=0.80$ , the effect of momentum coefficient 0.02 is evident at any blowing pattern. Most significant result of all 6 plot is seen at  $x/C=0.56$  when the uniform pattern blowing is applied. Highest  $-C_p$  value is reached at this pattern.

For all  $\alpha = 7^\circ$  pressure measurement results, suction peak at high momentum coefficient may be the indication of lift enhancement on the wing.

Figure 4.13 presents the results of the experiments at angle of attack 13 degrees for Re 35000. Pressure distributions at all stations are similar when the momentum coefficient varies between 0 and 0.01. However, each blowing coefficient creates a suction peak, which corresponds to vortex and vortex breakdown at  $x/C=0.32$ , where  $-C_p$  values show a sharp decrease near wing center compared to no control case. The descending pattern of blowing is clearly effective on the first measurement station at  $x/C=0.32$  for all momentum coefficients. The most significant change, for  $C_\mu =$

0.02, can be seen at first and second station. At these stations, an increase in highest value along with a decrease in lowest value of  $-C_p$  is evident. At the second station, decrease in  $-C_p$  values at low  $y/s$  region is an indicator of flow reattachment. Flat distribution is also observed at third station at  $x/C=0.80$ . For this configuration of experiments, the effect of blowing pattern is hardly seen.

Figure 4.14 presents the results of the experiments at angle of attack 13 degrees for Re 75000. Likewise Re 3500 results, blowing lower than  $C_\mu = 0.02$  momentum coefficient does not significantly affect the flow structure. However, at first station, an enhancement of  $-C_p$  values is evident. Remarkable changes can be seen when the momentum coefficient is set to 0.02 at  $x/C=0.56$ . At this station, an increase in highest value along with a decrease in lowest value of  $-C_p$  is evident. Flat pressure distribution is obtained at  $x/C=0.80$ .

For  $\alpha = 13^\circ$  results, pressure measurement and flow visualization results are in line with each other, which indicate that  $-C_p$  values are increased and three dimensional separation is dispersed. As a result, lift enhancement is expected over the wing surface due to high suction peak.

Figure 4.15 presents the flow field over the wing surface at  $\alpha= 16^\circ$  at Re 35000. An increase in  $-C_p$  values can be seen by the increase of blowing coefficient at  $x/C=0.32$ . The descending pattern of blowing is clearly effective on the first measurement station, whereas  $-C_p$  value doubles for highest momentum coefficient. At  $x/C=0.56$ , effect of descending pattern is still evident in terms of increasing the  $-C_p$  values whereas blowing in lower momentum coefficients seems to be ineffective on the flow structure. On third station  $x/C=0.80$ , flat distribution is eliminated by applying steady blowing through leading edges. It is observed that as the momentum coefficient is increased flow structure exhibits vortical flow distribution. However, for this configuration of experiments, the effect of blowing pattern is hardly seen. For all 9 plots, pressure distribution variations are more at momentum coefficient 0.02 compared to lower momentum coefficients.

Figure 4.16 presents the flow field over the wing surface at  $\alpha= 16^\circ$  at Re 75000. For all different blowing patterns, maximum and minimum  $-C_p$  values are witnessed at  $C_\mu = 0.02$ . The effectiveness of descending blowing pattern for all stations is

evident. Regardless of momentum coefficient number set, highest  $-C_p$  values are reached at descending blowing pattern for all cases, particularly momentum coefficient higher than  $C_\mu = 0.01$ . It is obvious that descending blowing pattern can even alter the flow distribution on the wing surface when the momentum coefficient is set to  $C_\mu = 0.01$ .

For  $\alpha = 16^\circ$  case, since the separated flow turns into a vortical flow structure, steady leading edge blowing provides a substantial enhancement in lift.

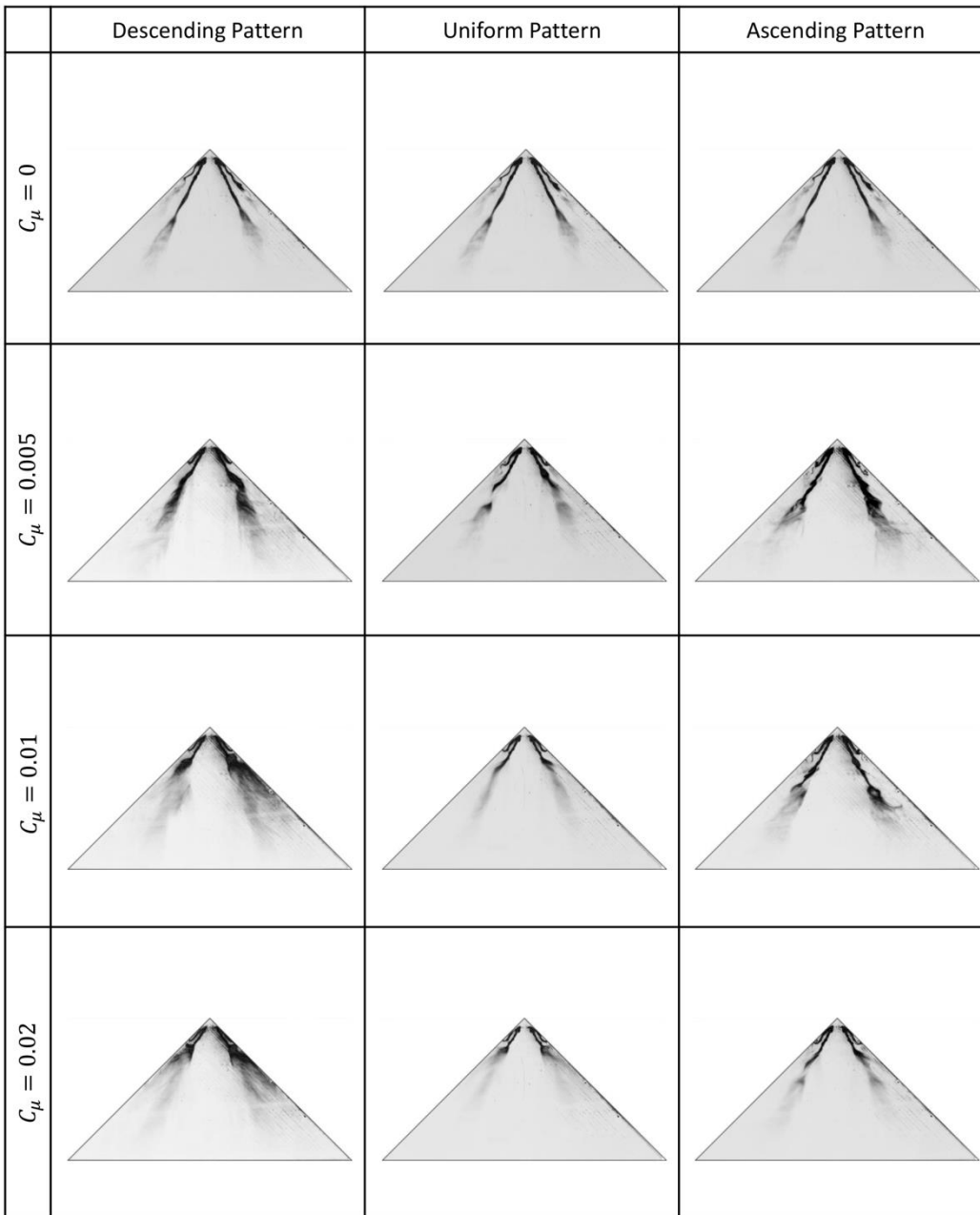


Figure 4.1 Surface flow visualization at  $\alpha = 7^\circ$  angle of attack and  $Re = 14000$ , at different momentum coefficients and blowing patterns

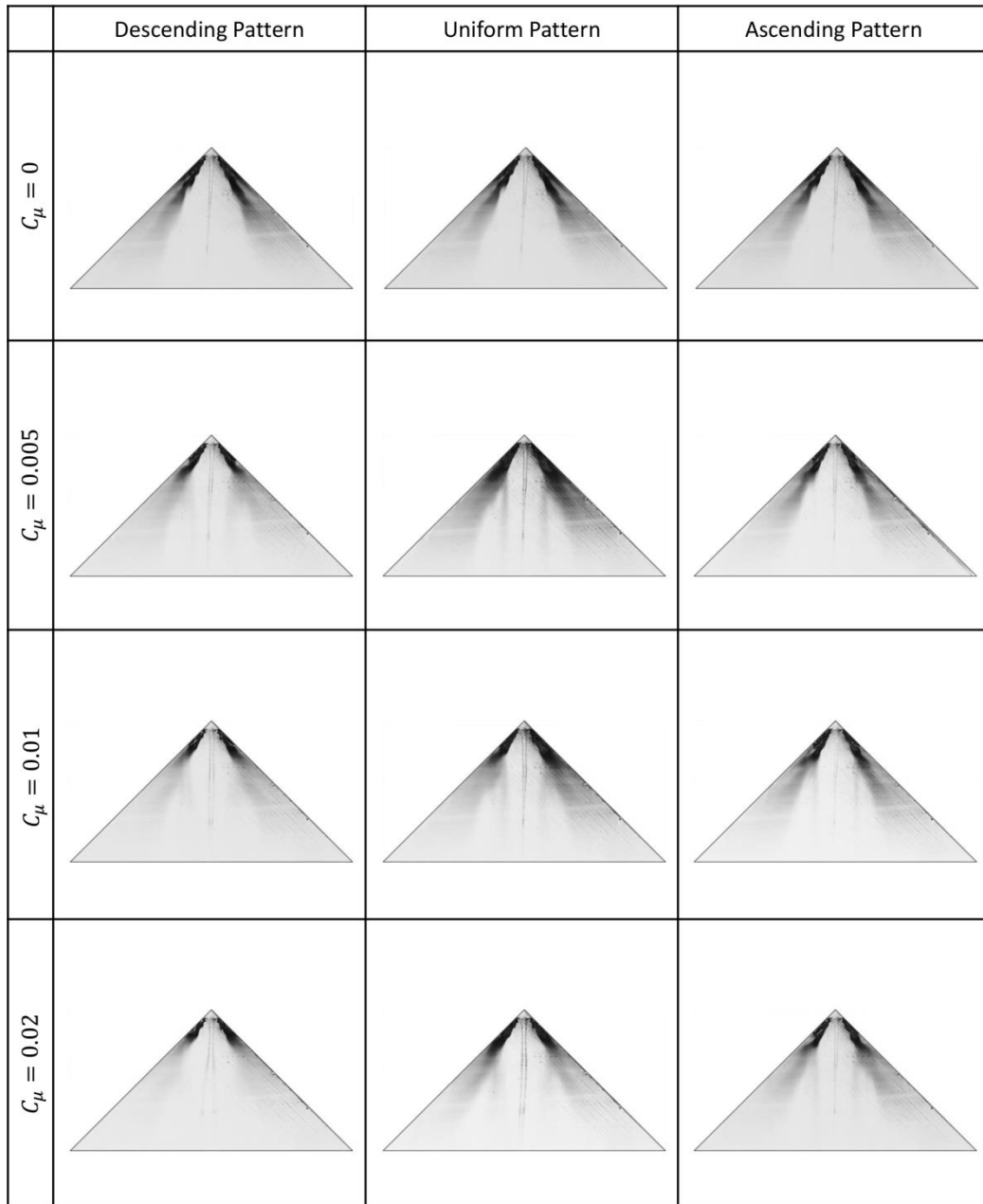


Figure 4.2 Surface flow visualization at  $\alpha = 7^{\circ}$  angle of attack and  $Re = 35000$ , at different momentum coefficients and blowing patterns

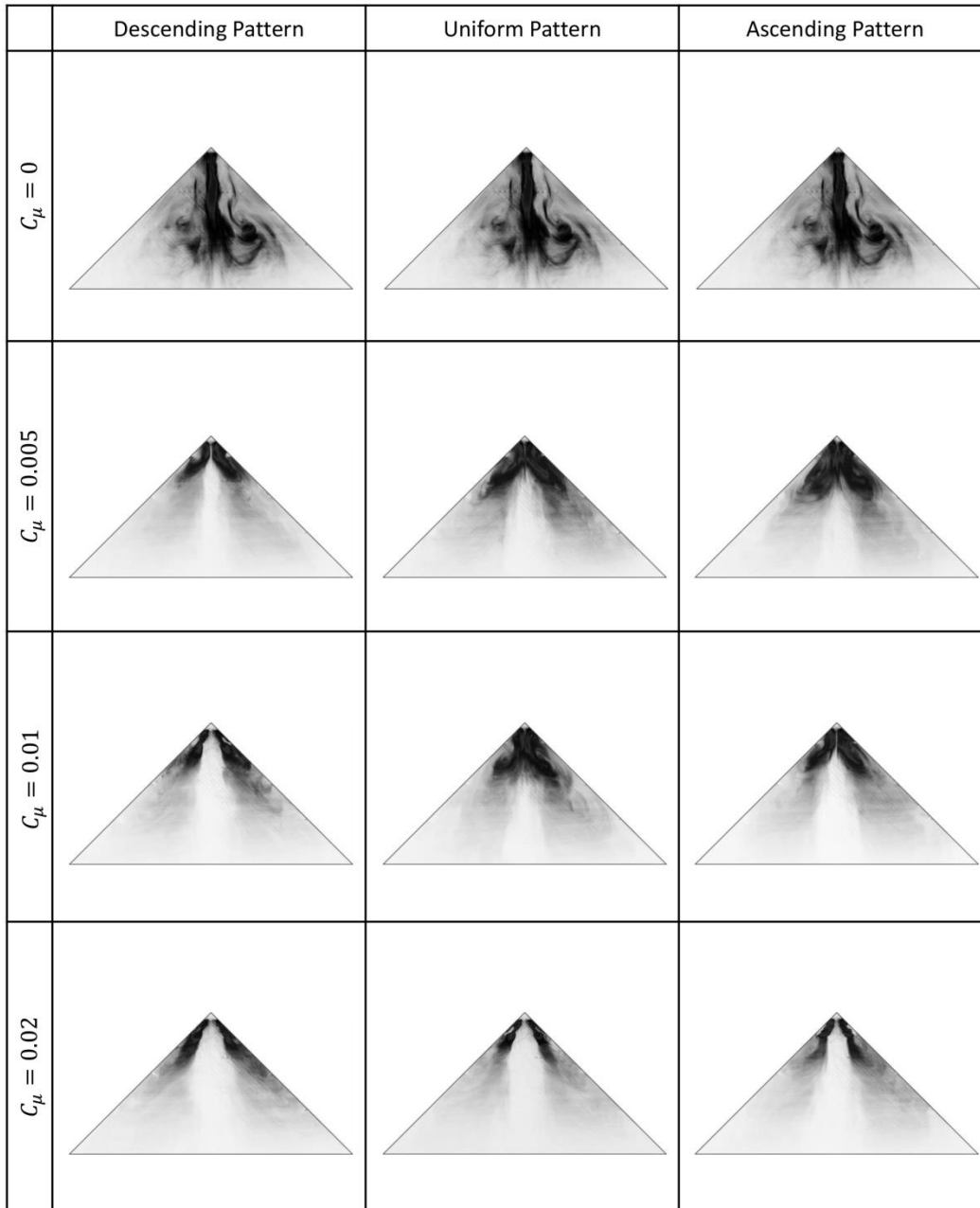


Figure 4.3 Surface flow visualization at  $\alpha = 13^\circ$  angle of attack and  $Re = 14000$ , at different momentum coefficients and blowing patterns

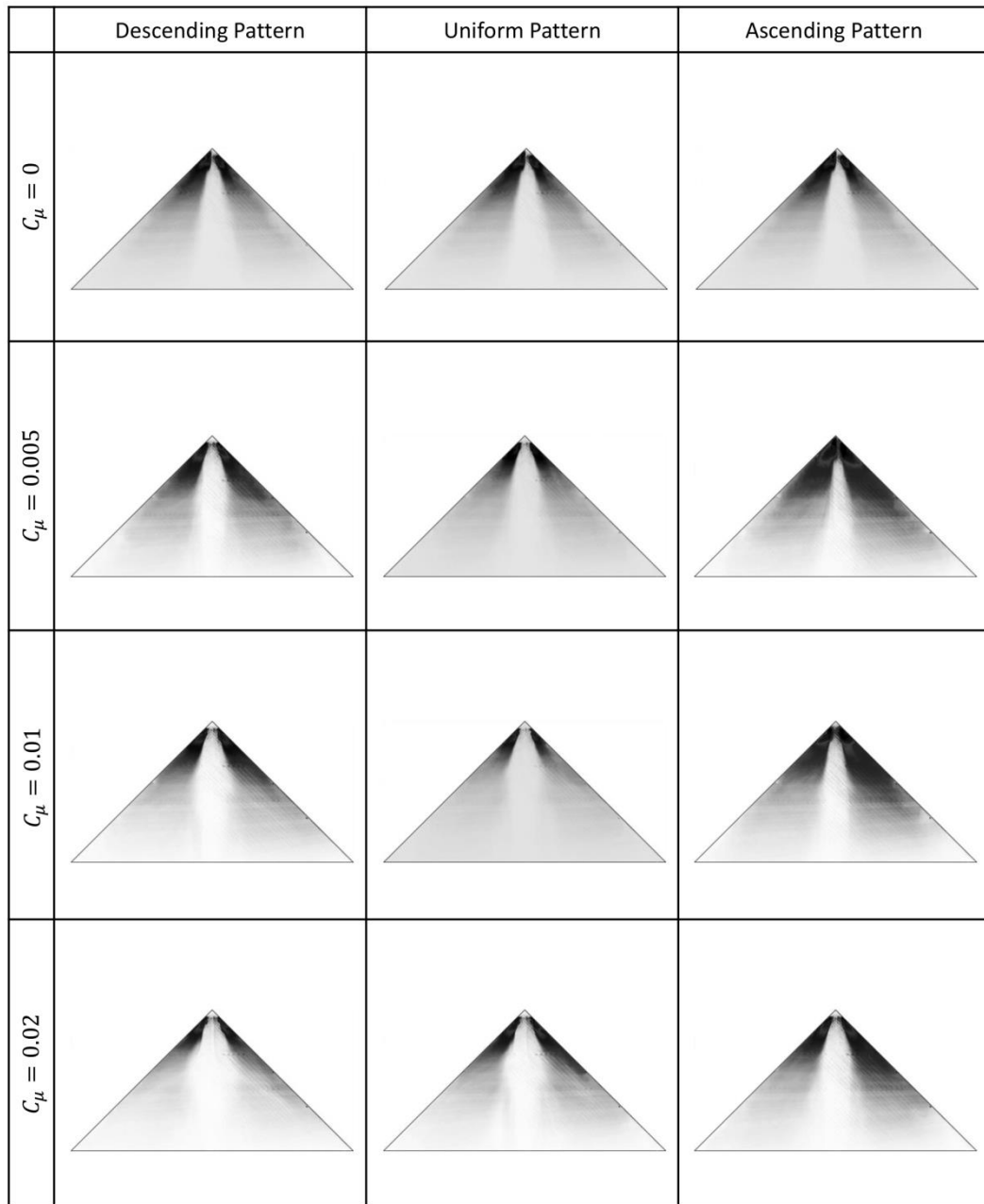


Figure 4.4 Surface flow visualization at  $\alpha = 13^{\circ}$  angle of attack and  $Re = 35000$ , at different momentum coefficients and blowing patterns

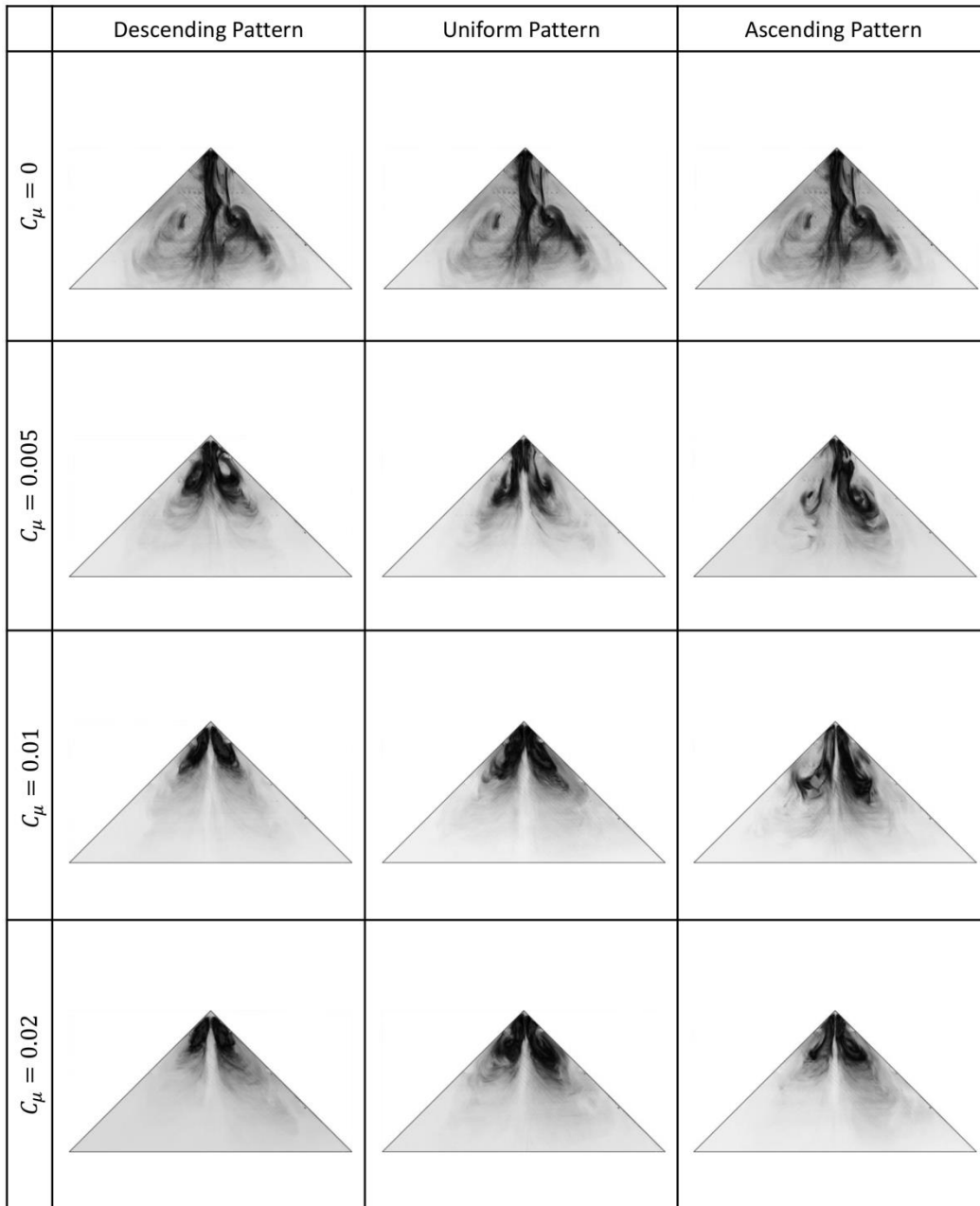


Figure 4.5 Surface flow visualization at  $\alpha = 16^\circ$  angle of attack and  $Re = 14000$ , at different momentum coefficients and blowing patterns

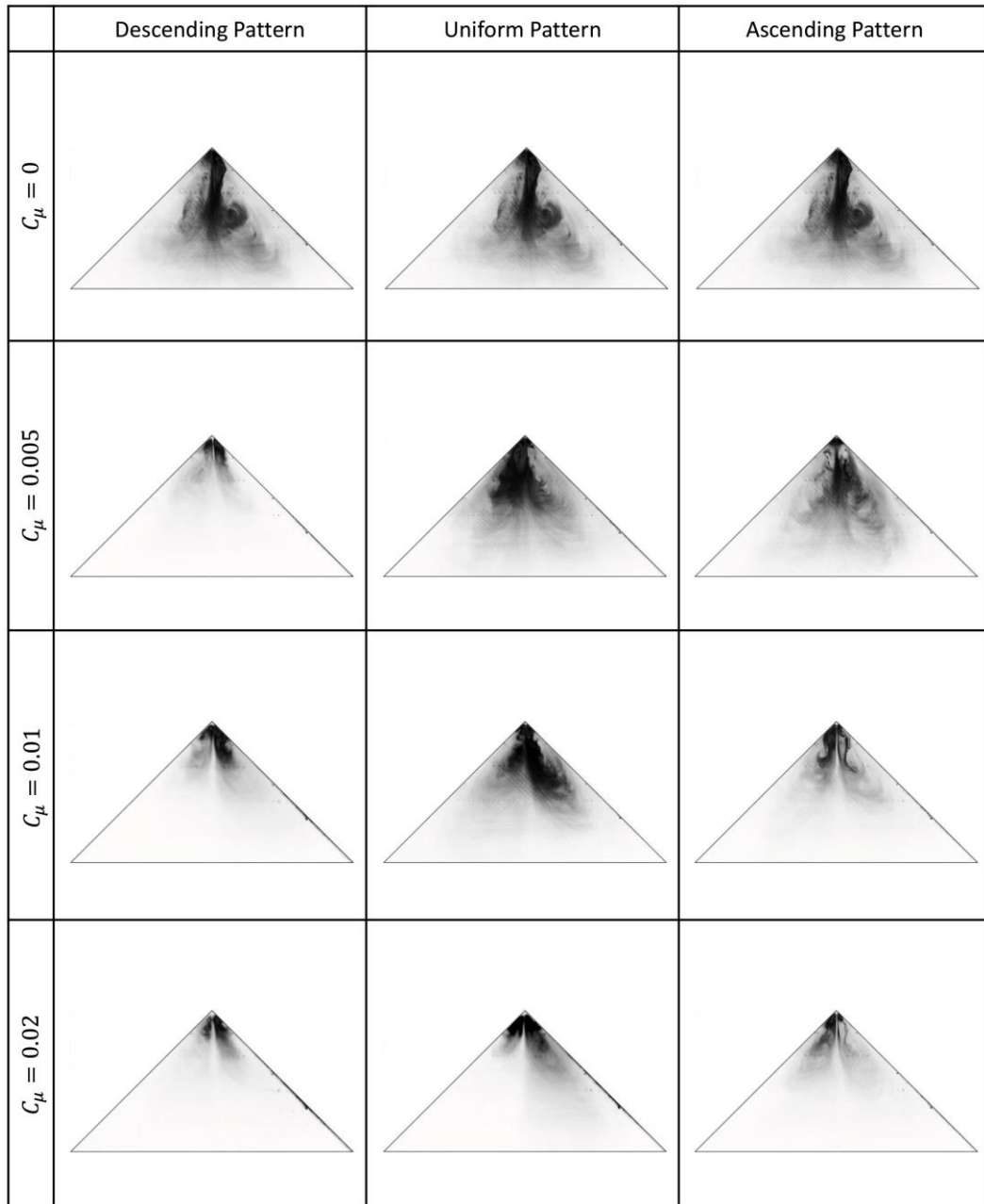


Figure 4.6 Surface flow visualization at  $\alpha = 16^{\circ}$  angle of attack and  $Re = 35000$ , at different momentum coefficients and blowing patterns

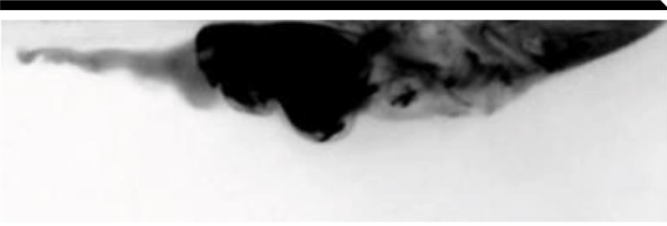
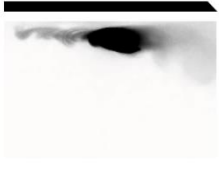
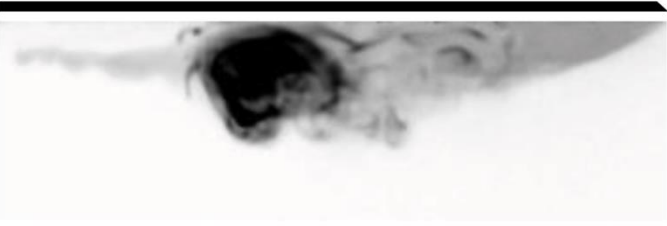
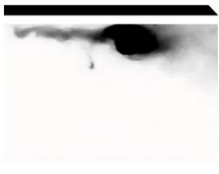
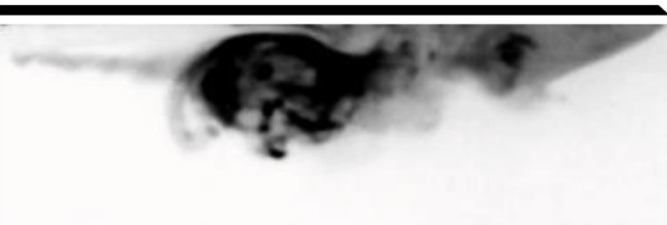
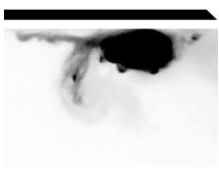
$\alpha = 7^\circ$ , Uniform Ordered Blowing		Smoke Visualization, Re = 14000
	1 <sup>st</sup> Station ( $x/C = 0.32$ )	3 <sup>rd</sup> Station ( $x/C = 0.80$ )
$C_\mu = 0$		
$C_\mu = 0.005$		
$C_\mu = 0.01$		
$C_\mu = 0.02$		

Figure 4.7 Cross flow visualization on  $x/C = 0.32$  and  $x/C = 0.80$  chordwise distances at  $\alpha = 7^\circ$  angle of attack and Re=14000 for different momentum coefficients

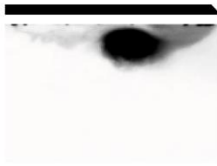
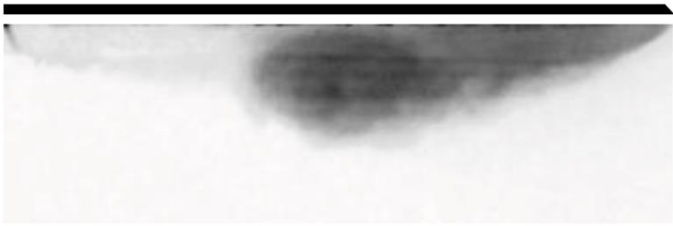
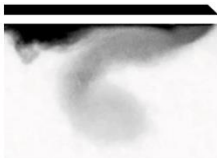
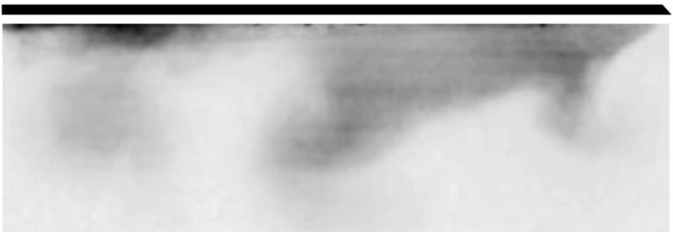
$\alpha = 7^\circ$ , Uniform Ordered Blowing		Smoke Visualization, Re = 35000
	1 <sup>st</sup> Station (x/C = 0.32)	3 <sup>rd</sup> Station (x/C = 0.80)
$C_\mu = 0$		
$C_\mu = 0.005$		
$C_\mu = 0.01$		
$C_\mu = 0.02$		

Figure 4.8 Cross flow visualization on  $x/C = 0.32$  and  $x/C = 0.80$  chordwise distances at  $\alpha = 7^\circ$  angle of attack and Re=35000 for different momentum coefficients

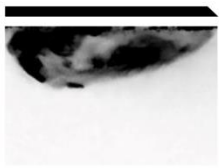
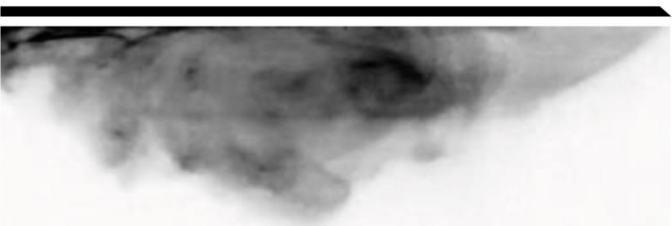
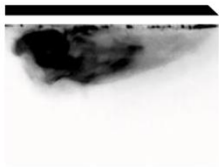
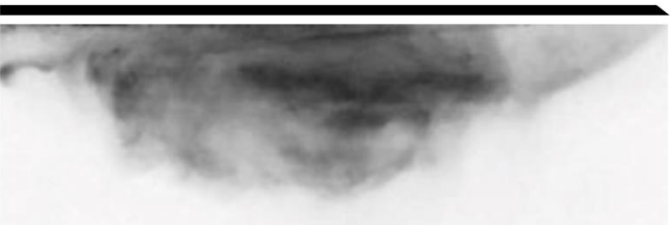
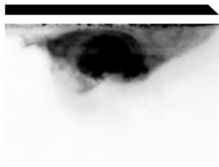
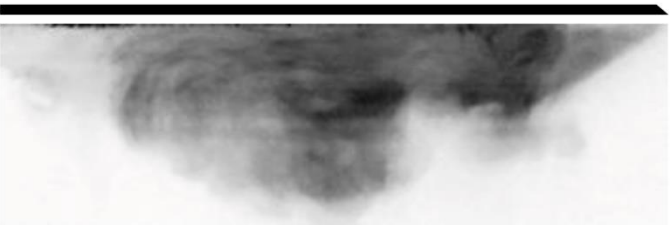
$\alpha = 13^\circ$ , Uniform Ordered Blowing		Smoke Visualization, Re = 14000
	1 <sup>st</sup> Station ( $x/C = 0.32$ )	3 <sup>rd</sup> Station ( $x/C = 0.80$ )
$C_\mu = 0$		
$C_\mu = 0.005$		
$C_\mu = 0.01$		
$C_\mu = 0.02$		

Figure 4.9 Cross flow visualization on  $x/C = 0.32$  and  $x/C = 0.80$  chordwise distances at  $\alpha = 13^\circ$  angle of attack and Re=14000 for different momentum coefficients

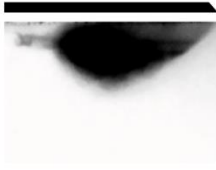
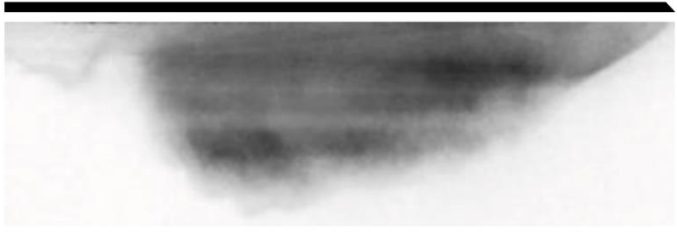
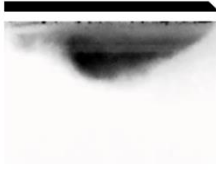
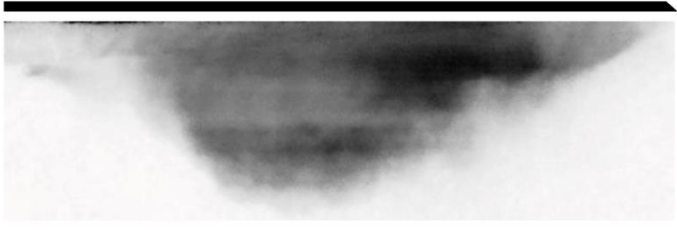
$\alpha = 13^\circ$ , Uniform Ordered Blowing		Smoke Visualization, Re = 35000
	1 <sup>st</sup> Station ( $x/C = 0.32$ )	3 <sup>rd</sup> Station ( $x/C = 0.80$ )
$C_\mu = 0$		
$C_\mu = 0.005$		
$C_\mu = 0.01$		
$C_\mu = 0.02$		

Figure 4.10 Cross flow visualization on  $x/C = 0.32$  and  $x/C = 0.80$  chordwise distances at  $\alpha = 13^\circ$  angle of attack and Re=35000 for different momentum coefficients

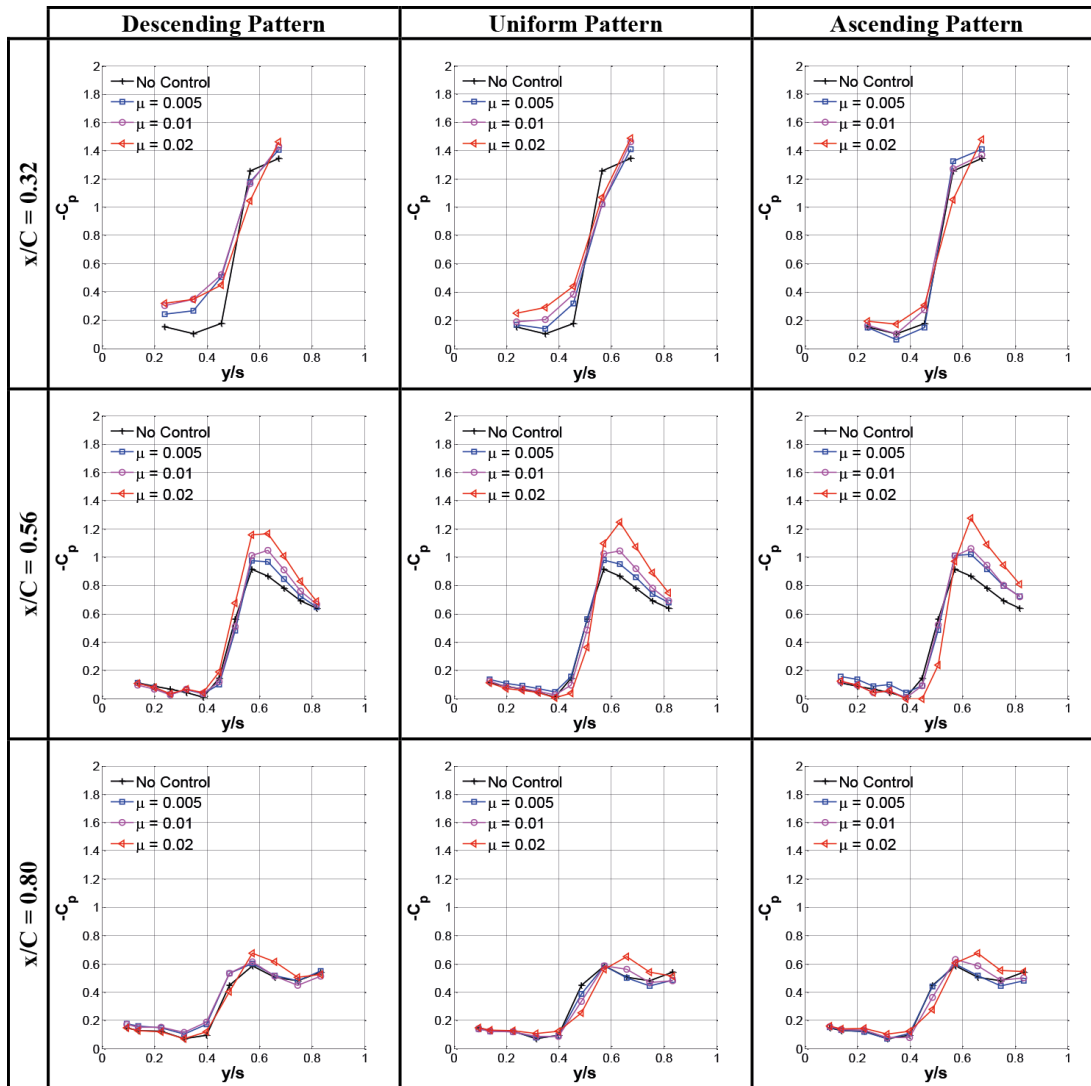


Figure 4.11 Spanwise  $-C_p$  plots at  $\alpha = 7^\circ$  angle of attack and  $Re=35000$  on chordwise distances of  $x/C = 0.32, 0.56$  and  $0.80$  and different Reynolds numbers

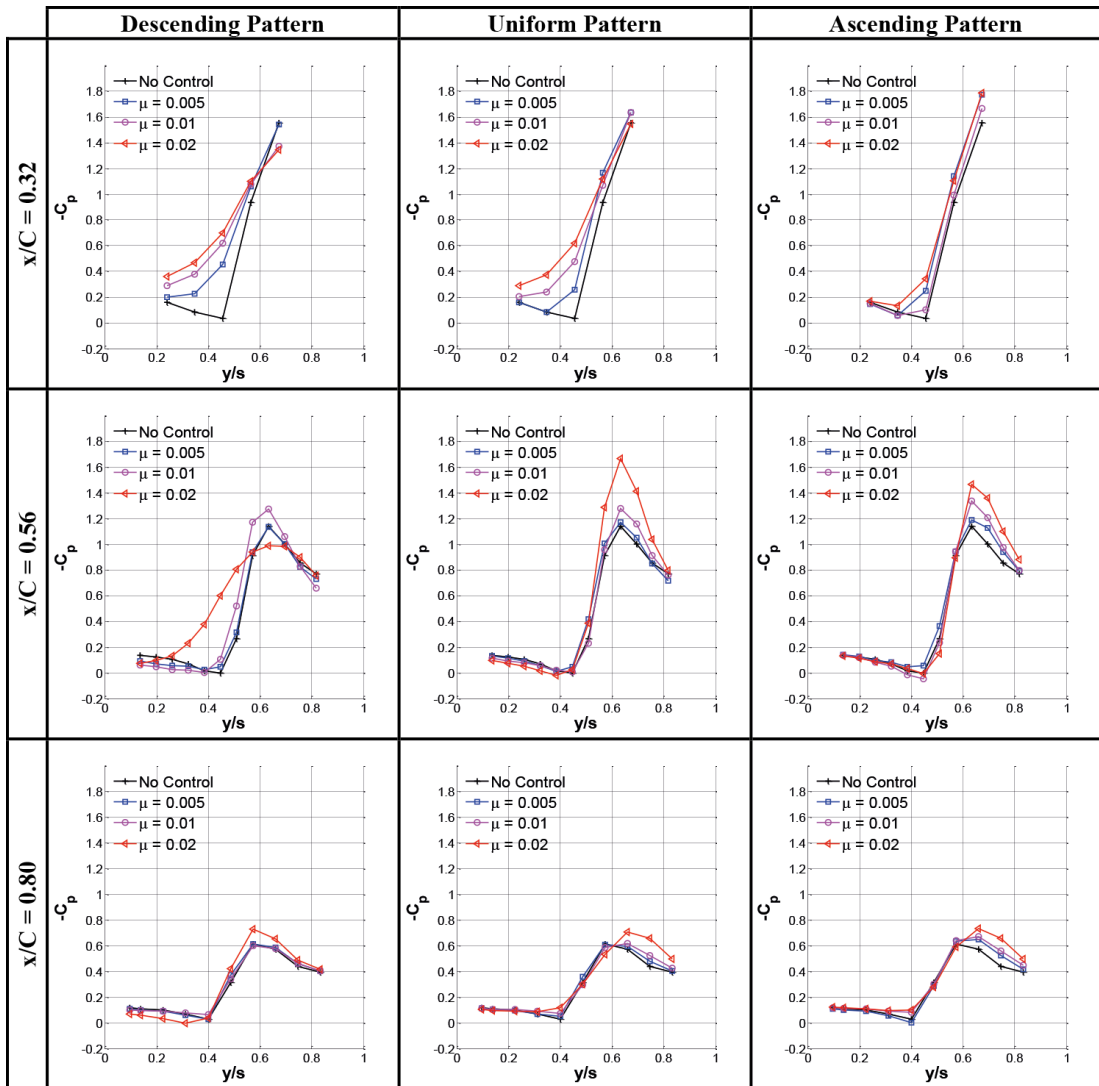


Figure 4.12 Spanwise  $-C_p$  plots at  $\alpha = 7^\circ$  angle of attack and  $Re=75000$  on chordwise distances of  $x/C = 0.32, 0.56$  and  $0.80$  and different Reynolds numbers

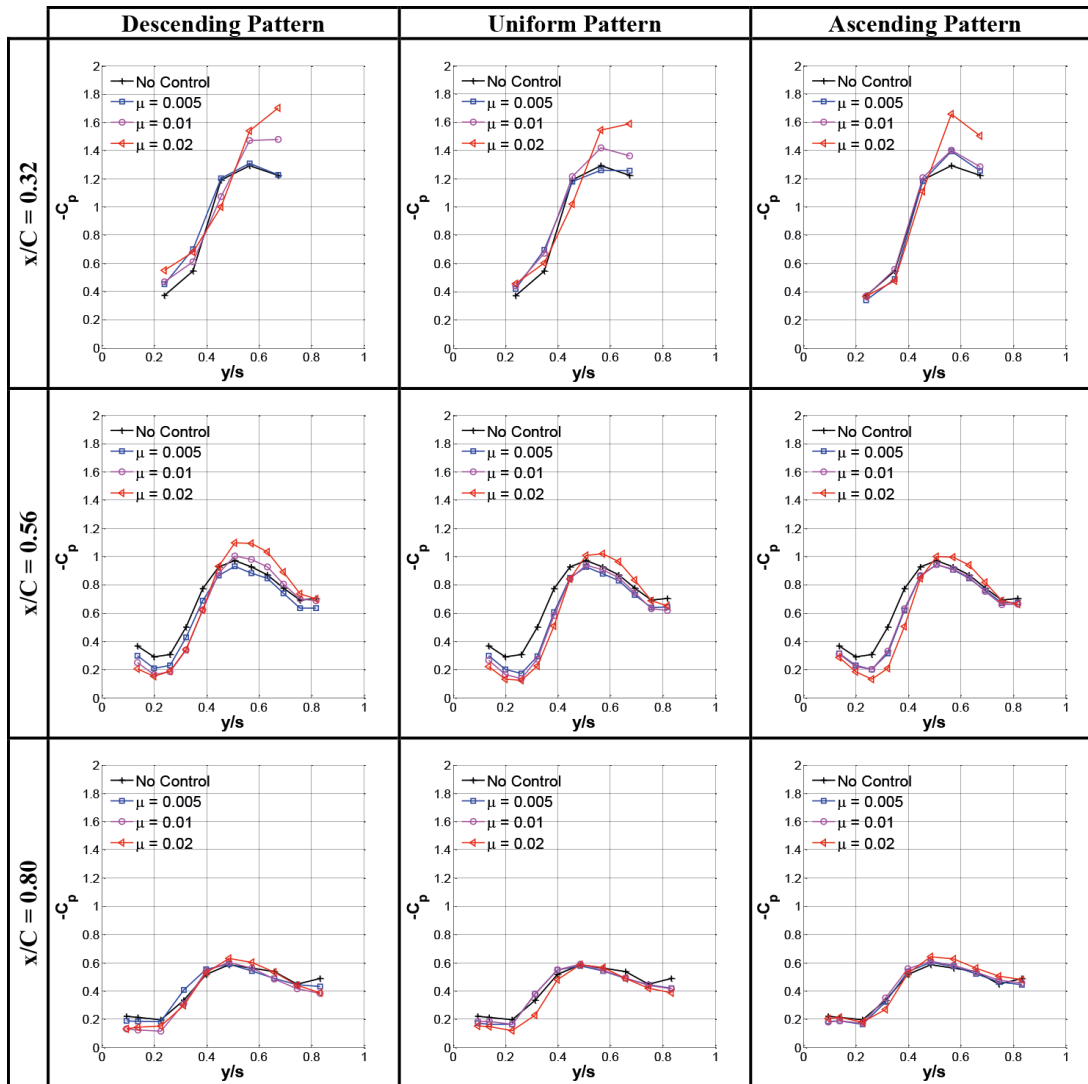


Figure 4.13 Spanwise  $-C_p$  plots at  $\alpha = 13^\circ$  angle of attack and  $Re=35000$  on chordwise distances of  $x/C = 0.32, 0.56$  and  $0.80$  and different Reynolds numbers

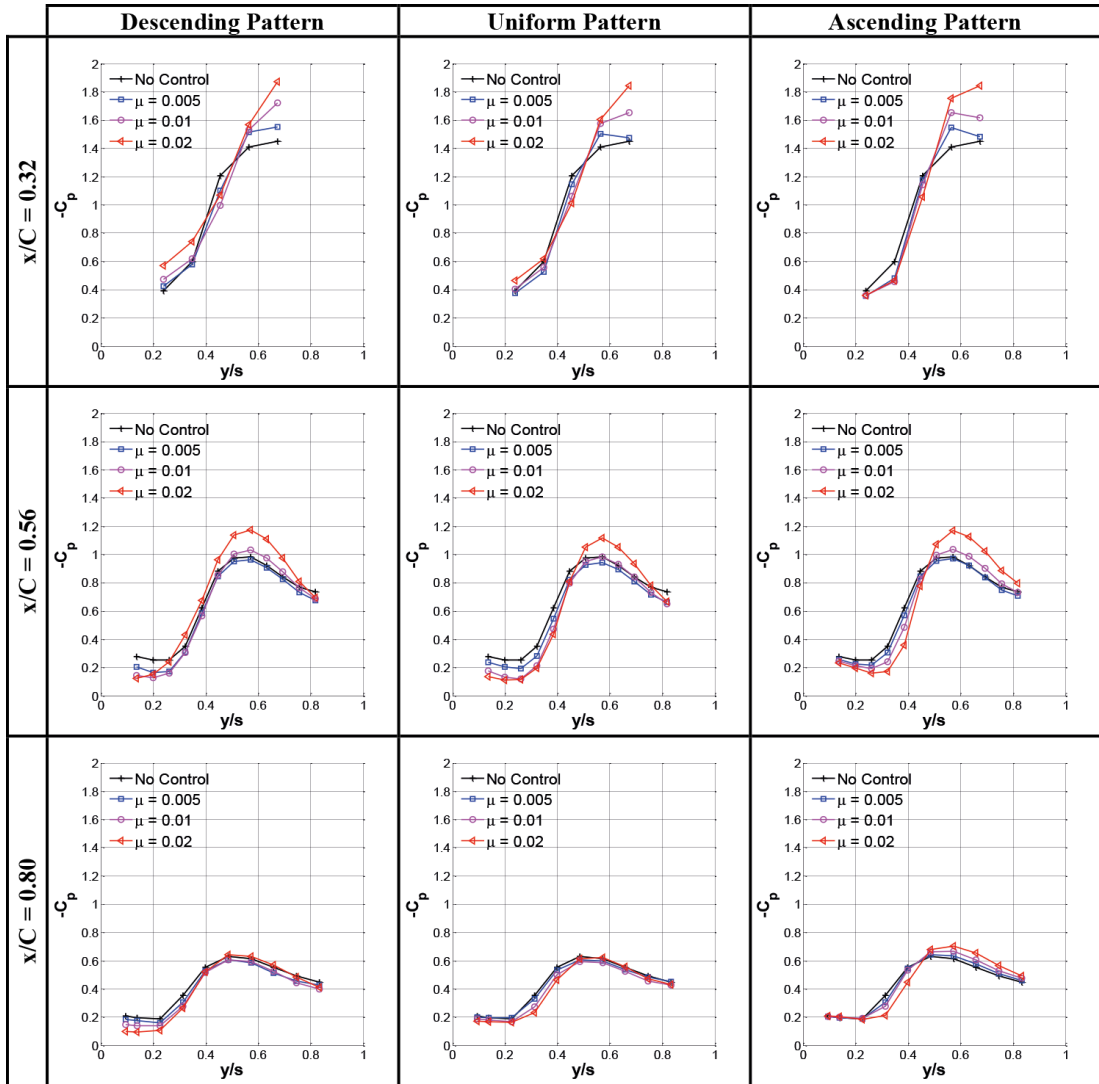


Figure 4.14 Spanwise  $-C_p$  plots at  $\alpha = 13^\circ$  angle of attack and  $Re=75000$  on chordwise distances of  $x/C = 0.32, 0.56$  and  $0.80$  and different Reynolds numbers

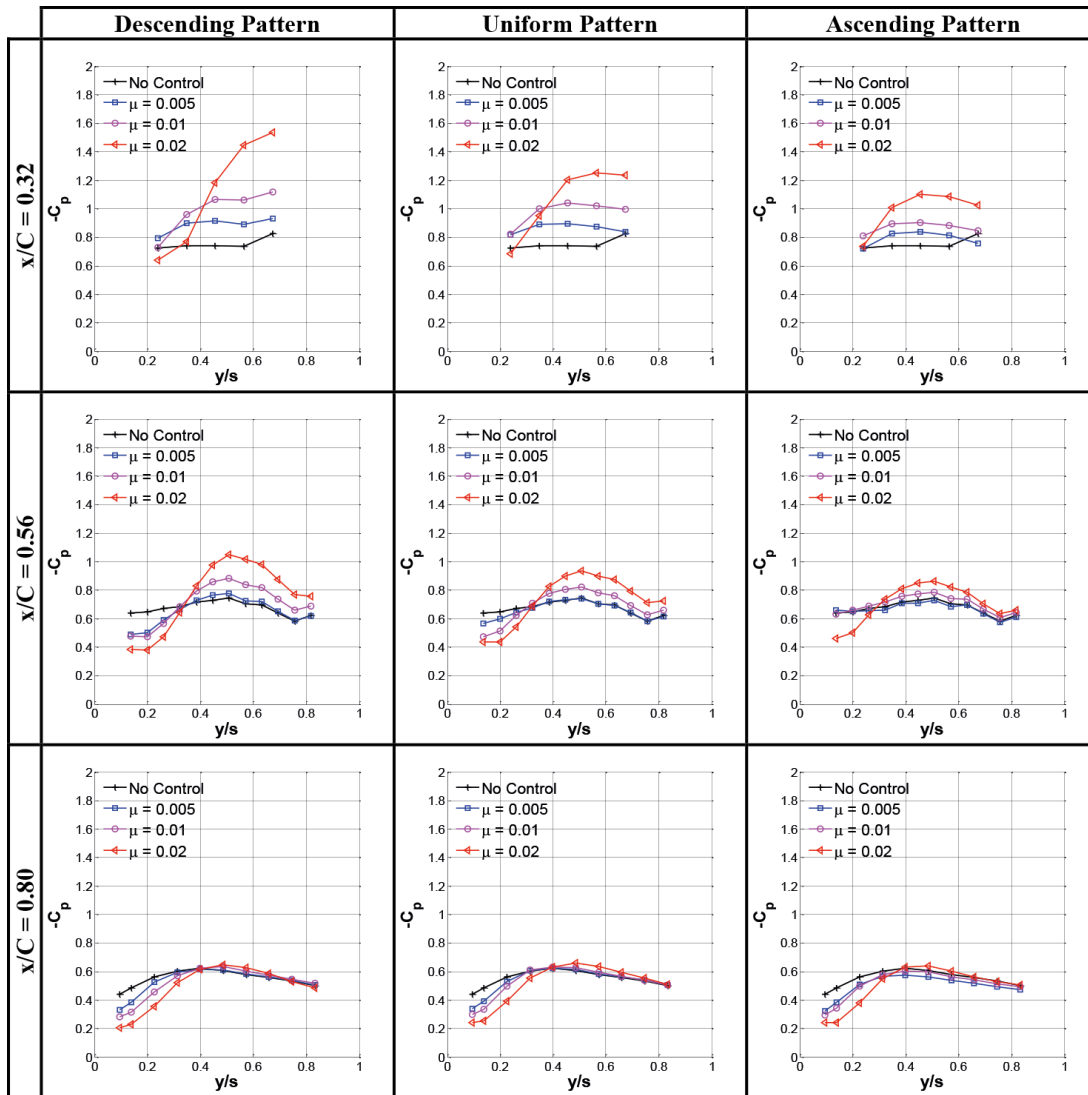


Figure 4.15 Spanwise  $-C_p$  plots at  $\alpha = 16^\circ$  angle of attack and  $Re=35000$  on chordwise distances of  $x/C = 0.32, 0.56$  and  $0.80$  and different Reynolds numbers

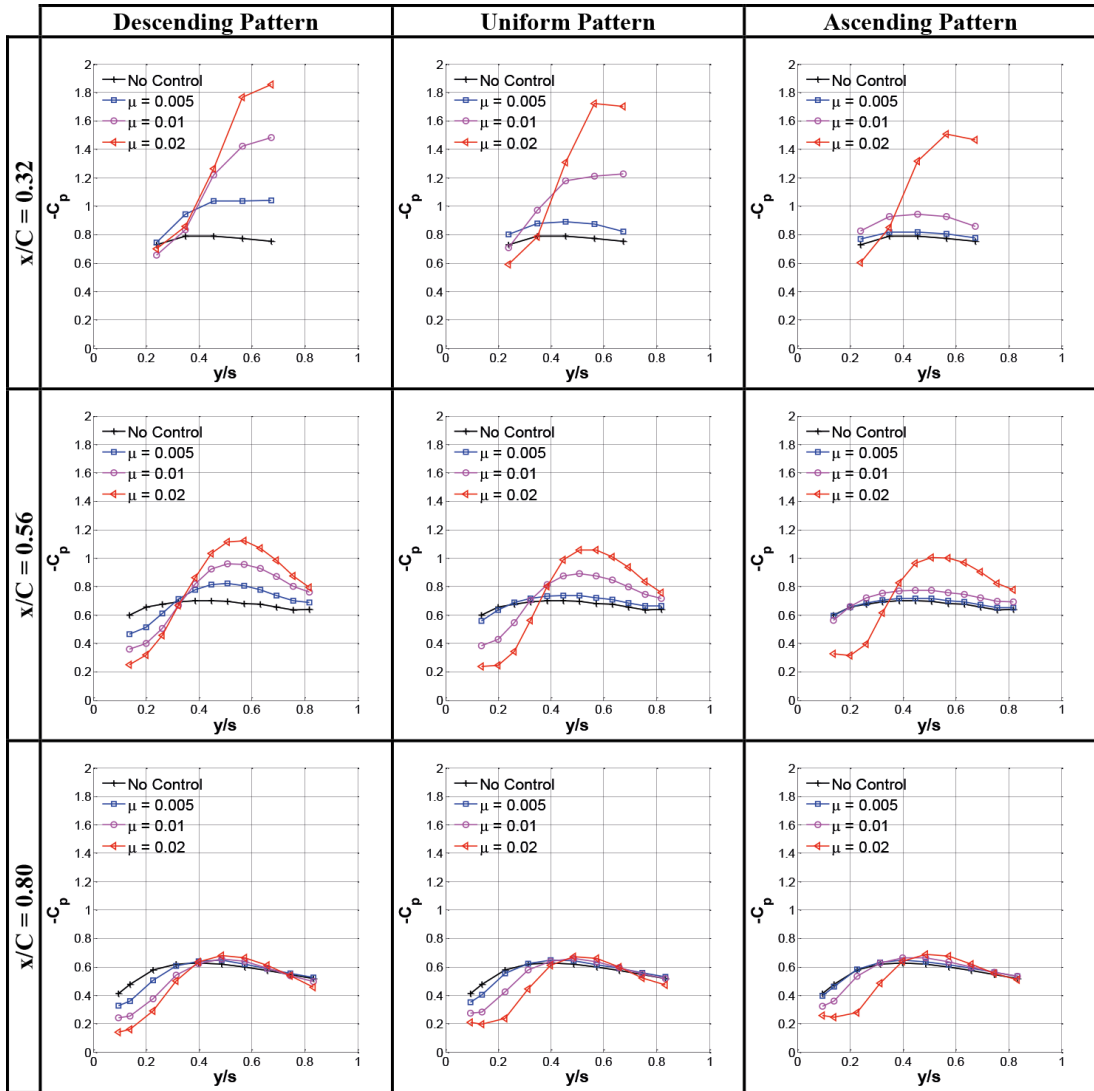


Figure 4.16 Spanwise  $-C_p$  plots at  $\alpha = 16^\circ$  angle of attack and  $Re=75000$  on chordwise distances of  $x/C = 0.32, 0.56$  and  $0.80$  and different Reynolds numbers



## CHAPTER 5

### CONCLUSION AND RECOMMENDATIONS FOR FUTURE WORK

#### 5.1 Conclusion

The present study focuses on the effect of steady blowing pattern through the leading edge on flow structure of  $\Lambda = 45^\circ$  delta wing at broad range of Reynolds number and angle of attack. Variation in vortex breakdown location or elimination of three-dimensional separation with recovery of the vortical flow structure is investigated at attack angles of  $7^\circ$ ,  $13^\circ$  and  $16^\circ$  and Reynolds numbers varying from  $Re = 1.4 \times 10^4$  to  $Re = 7.5 \times 10^4$  both qualitatively and quantitatively using laser illuminated smoke visualization and surface pressure measurements. Surface smoke visualization experiments were performed at a plane parallel to the center plane of vortex core. Cross flow visualization experiments were conducted at chordwise distances of  $x/C = 0.32$  and  $0.80$ , where the first and third pressure taps are located, respectively. Pressure measurements were taken from pressure taps that are located in three different chordwise distances on the wing surface. Moreover, three different blowing patterns were utilized from leading edge of the wing with corresponding momentum coefficients of  $0.005$ ,  $0.01$  and  $0.02$ . Based on the present investigation performed, the following are concluded:

- Excitation through the leading edge provides good enhancement on the flow structure at relatively high attack angles. It is quite effective in preventing the three-dimensional surface separation and recovering the leading edge vortices. For instance, at  $\alpha = 13^\circ$ , once the momentum coefficient is set to  $0.01$ , three-dimensional surface separation starts to vanish and leading edge vortices become apparent.

- Considering all experiments performed in this study, surface flow visualization and pressure measurement experiments have an agreement with each other.
- Descending blowing pattern seems to be more effective compared to other patterns tested in the experiments, showing that control near the apex can be more efficient.
- At  $\alpha = 7^\circ$ , applying flow control technique does not enhance the flow structure, in fact, blowing through leading edges disturbs dual vortex structure for low Reynolds number experiments and causes vortex breakdown earlier than it already is. However, for  $Re=35000$ , excitation moves vortex breakdown upstream slower and does not significantly change vortex breakdown location compared to excitation at lower Reynolds number visualization.
- At  $\alpha = 13^\circ$ , excitation through leading edge can enhance the pressure distribution for the descending blowing pattern. It can be observed that the excitation increases the highest  $-C_p$  values between the range of 10-20 % and decreases the lowest  $-C_p$  values between the range of 40-50 %.
- For  $\alpha = 16^\circ$  at first station, the air injection with descending blowing pattern can alter  $-C_p$  values up to 100-120 %, which creates a dramatical change of the flow structure as flat distribution turns into a vortical structure. At second station, the influence of the steady leading edge blowing corresponds to a 50-60 % increase in highest value along with a 40-50 % decrease in lowest value of  $-C_p$  values.
- Regarding the flow visualization and pressure measurement results the effectiveness of steady leading edge blowing can be considered as a function of Reynolds number and angle of attack.
- Considering flow visualization and pressure measurement results, several assumptions for lift enhancement can be proposed. For  $\alpha = 7^\circ$  case, despite the fact that blowing causes deterioration of vortical structure, pressure measurement results show an enhancement in pressure distribution, which indicates a possible increase in lift over the wing surface. For  $\alpha = 13^\circ$  case, it can be concluded from the flow visualization and pressure measurement

results that steady leading edge blowing improves overall flow structure where three dimensional separation is dispersed or vortex breakdown location is delayed over the wing and creates suction peaks in the flow field where  $-C_p$  values are increased. These facts may be considered as an indication of lift enhancement. For  $\alpha = 16^\circ$  case, separated flow over the wing is converted into a vortical flow structure by steady leading edge blowing, which presumably would cause a substantial increase in lift.

## 5.2 Recommendations for Future Work

Results indicate that steady blowing through leading edges is quite sufficient and practical for most cases. However, further investigations could be studied as following:

- Since the results show angle of attack and Reynolds number dependence, critical angle of attack and critical Reynolds number should be investigated for further experiments to determine until what angle of attack and Reynolds number blowing deteriorates flow structure.
- Momentum coefficient can be lowered to figure out critical number of amount of momentum, particularly for descending pattern.
- Blowing patterns and methods could be varied with different designs to enhance the effect of blowing, such as different blowing hole designs, different blowing locations and various of wings having different thicknesses.
- The ratios of the momentum given through the leading edges could be varied in descending ordered blowing, which gives the best enhancement in flow structure for relatively high angles of attack.
- Experiments could be supported by Particle Image Velocimetry (PIV) measurements to understand velocity field passing through surface of the wing, particularly at the locations where transition of the flow structure occurs.



## REFERENCES

- [1] I. Gursul, “Vortex flows on UAVs: Issues and challenges,” *Aeronaut. J.*, vol. 108, no. 1090, pp. 597–610, 2004.
- [2] I. Gursul, R. Gordnier, and M. Visbal, “Unsteady aerodynamics of nonslender delta wings,” *Prog. Aerosp. Sci.*, vol. 41, no. 7, pp. 515–557, Oct. 2005.
- [3] I. Gursul, Z. Wang, and E. Vardaki, “Review of flow control mechanisms of leading-edge vortices,” *Progress in Aerospace Sciences*, vol. 43, pp. 246–270, 2007.
- [4] M. Lee and C. Ho, “Lift force of delta wings,” vol. 43, no. 9, 1990.
- [5] P. B. Earnshaw and J. A. Lawford, *Low-speed wind tunnel experiments on a series of sharp-edged delta wings*. H. Majesty’s Stationery Office, 1966.
- [6] N. M. Williams, Z. Wang, and I. Gursul, “Active Flow Control on a Nonslender Delta Wing,” *J. Aircr.*, vol. 45, no. 6, pp. 2100–2110, Nov. 2008.
- [7] I. Gursul, “Review of Unsteady Vortex Flows over Slender Delta Wings,” *J. Aircr.*, vol. 42, no. 2, pp. 299–319, Mar. 2005.
- [8] M. V. Ol and M. Gharib, “Leading-Edge Vortex Structure of Nonslender Delta Wings at Low Reynolds Number,” *AIAA Journal*, vol. 41, pp. 16–26, 2003.
- [9] G. S. Taylor and I. Gursul, “Buffeting Flows over a Low-Sweep Delta Wing,” *AIAA J.*, vol. 42, no. 9, pp. 1737–1745, Sep. 2004.
- [10] H. Werle, “Hydrodynamic flow visualization,” *Annu. Rev. Fluid Mech.*, vol. 5, no. 1, pp. 361–386, 1973.
- [11] D. L. Kohlman and J. R. Wentz W. H., “Vortex breakdown on slender sharp-edged wings,” *J. Aircr.*, vol. 8, no. 3, pp. 156–161, Mar. 1971.
- [12] J. Andreopoulos and J. H. Agui, “Wall-vorticity flux dynamics in a two-dimensional turbulent boundary layer,” *J. Fluid Mech.*, vol. 309, pp. 45–84,

- 1996.
- [13] M. M. Yavuz, “Origin and control of the flow structure and topology on delta wings.” 2006.
- [14] S. Yayla, Ç. Canpolat, B. Şahin, and H. Akilli, “Elmas Kanat Modelinde Oluşan Girdap Çökmesine Sapma Açısının Etkisi,” *Isı Bilim. ve Tek. Dergisi/Journal Therm. Sci. Technol.*, vol. 30, no. 1, 2010.
- [15] C. Breitsamter, “Unsteady flow phenomena associated with leading-edge vortices,” *Prog. Aerosp. Sci.*, vol. 44, no. 1, pp. 48–65, 2008.
- [16] M. M. Yavuz and D. Rockwell, “Identification and Control of Three-Dimensional Separation on Low Swept Delta Wing,” *AIAA J.*, vol. 44, no. 11, pp. 2805–2811, Nov. 2006.
- [17] J. M. Delery, “Aspects of vortex breakdown,” *Prog. Aerosp. Sci.*, vol. 30, no. 1, pp. 1–59, Jan. 1994.
- [18] H. Johari, D. J. Olinger, and K. C. Fitzpatrick, “Delta Wing Vortex Control via Recessed Angled Spanwise Blowing,” vol. 32, no. 4, pp. 804–810, 1995.
- [19] M. Zharfa, I. Ozturk, and M. M. Yavuz, “Flow Structure on Nonslender Delta Wing: Reynolds Number Dependence and Flow Control,” *AIAA J.*, vol. 54, no. 3, pp. 880–897, Jan. 2016.
- [20] A. M. Mitchell, D. Barberis, P. Molton, and J. Delery, “Oscillation of vortex breakdown location and blowing control of time-averaged location,” *AIAA J.*, vol. 38, no. 0, pp. 793–803, 2000.
- [21] F. Renac, D. Barberis, and P. Molton, “Control of Vortical Flow over a Rounded Leading-Edge Delta Wing,” *AIAA J.*, vol. 43, no. 7, pp. 1409–1418, 2005.
- [22] D. Rockwell, “Three-dimensional flow structure on delta wings at high angle-of-attack- Experimental concepts and issues,” in *AIAA, Aerospace Sciences Meeting and Exhibit, 31 st, Reno, NV*, 1993, p. 1993.
- [23] M. Visbal, “Computational and physical aspects of vortex breakdown on delta wings,” in *33rd Aerospace Sciences Meeting and Exhibit*, American Institute

of Aeronautics and Astronautics, 1995.

- [24] C. Shih and Z. Ding, “Unsteady structure of leading-edge vortex flow over a delta wing,” in *34th Aerospace Sciences Meeting and Exhibit*, American Institute of Aeronautics and Astronautics, 1996.
- [25] I. Gursul, “Unsteady flow phenomena over delta wings at high angle of attack,” *AIAA J.*, vol. 32, no. 2, pp. 225–231, Feb. 1994.
- [26] O. K. Rediniotis, H. Stapountzis, and D. P. Telionis, “Periodic vortex shedding over delta wings,” *AIAA J.*, vol. 31, no. 9, pp. 1555–1562, Sep. 1993.
- [27] M. Menke and I. Gursul, “Unsteady nature of leading edge vortices,” *Phys. Fluids*, vol. 9, no. 10, p. 2960, 1997.
- [28] I. Gursul and W. Xie, “Buffeting Flows over Delta Wings,” *AIAA J.*, vol. 37, no. 1, pp. 58–65, Jan. 1999.
- [29] R. E. Gordnier and M. R. Visbal, “Unsteady vortex structure over a delta wing,” *J. Aircr.*, vol. 31, no. 1, pp. 243–248, Jan. 1994.
- [30] B. Yaniktepe and D. Rockwell, “Flow Structure on a Delta Wing of Low Sweep Angle,” *AIAA J.*, vol. 42, no. 3, pp. 513–523, Mar. 2004.
- [31] E. Vardaki, I. Gursul, and G. Taylor, “Physical Mechanisms of Lift Enhancement for Flexible Delta Wings,” in *43rd AIAA Aerospace Sciences Meeting and Exhibit*, American Institute of Aeronautics and Astronautics, 2005.
- [32] I. Gursul, E. Vardaki, and Z. Wang, “Active and Passive Control of Reattachment on Various Low-Sweep Wings,” in *44th AIAA Aerospace Sciences Meeting and Exhibit*, American Institute of Aeronautics and Astronautics, 2006.
- [33] A. M. Mitchell, D. Barberis, P. Molton, and D. Jean, “Control of Leading-Edge Vortex Breakdown by Trailing Edge Injection Introduction,” *J. Aircr.*, vol. 39, no. 2, pp. 221–226, 2002.
- [34] K. Parmenter and D. Rockwell, “Transient response of leading-edge vortices to localized suction,” *AIAA J.*, vol. 28, no. 6, pp. 1131–1133, Jun. 1990.

- [35] H. Johari and J. Moreira, "Delta wing vortex manipulation using pulsed and steady blowing during ramp-pitching," *J. Aircr.*, vol. 33, no. 2, pp. 304–310, Mar. 1996.
- [36] H. E. Helin and C. W. Watry, "Effects of trailing-edge jet entrainment on delta wing vortices," *AIAA J.*, vol. 32, no. 4, pp. 802–804, Apr. 1994.
- [37] C. Shih and Z. Ding, "Trailing-edge jet control of leading-edge vortices of a delta wing," *AIAA J.*, vol. 34, no. 7, pp. 1447–1457, Jul. 1996.
- [38] S. Phillips, C. Lambert, and I. Gursul, "Effect of a Trailing-Edge Jet on Fin Buffeting," in *1st Flow Control Conference*, American Institute of Aeronautics and Astronautics, 2002.
- [39] W. Gu, O. Robinson, and D. Rockwell, "Control of vortices on a delta wing by leading-edge injection," *AIAA J.*, vol. 31, no. 7, pp. 1177–1186, Jul. 1993.
- [40] D. Nawrocki, "Differential and vectored trailing edge jet control of delta wing vortices," in *33rd Aerospace Sciences Meeting and Exhibit*, American Institute of Aeronautics and Astronautics, 1995.
- [41] P. Vorobieff and D. Rockwell, "Multiple-actuator control of vortex breakdown on a pitching delta wing," *AIAA J.*, vol. 34, no. 10, pp. 2184–2186, Oct. 1996.
- [42] P. V Vorobieff and D. O. Rockwell, "Vortex Breakdown on Pitching Delta Wing: Control by Intermittent Trailing-Edge Blowing," *AIAA J.*, vol. 36, no. 4, pp. 585–589, Apr. 1998.
- [43] M. M. Yavuz and D. Rockwell, "Control of Flow Structure on Delta Wing with Steady Trailing-Edge Blowing," vol. 44, no. 3, 2006.
- [44] G. N. Malcolm and A. M. Skow, "Flow visualization study of vortex manipulation on fighter configurations at high angles of attack," in *In AGARD, Aerodynamic and Related Hydrodynamic Studies Using Water Facilities 19 p (SEE N88-23125 16-34)*, 1987, vol. 1.
- [45] S. Margalit, D. Greenblatt, A. Seifert, and I. Wygnanski, "Delta Wing Stall and Roll Control Using Segmented Piezoelectric Fluidic Actuators," *J. Aircr.*,

vol. 42, no. 3, pp. 698–709, May 2005.

- [46] J. Riou, E. Garnier, and C. Basdevant, “Control of the Flow over a Delta Wing in the Transonic Regime,” *AIAA J.*, vol. 48, no. 8, pp. 1851–1855, Aug. 2010.
- [47] S. McCormick and I. Gursulf, “Effect of Shear-Layer Control on Leading-Edge Vortices,” *J. Aircr.*, vol. 33, no. 6, pp. 1087–1093, 1996.
- [48] Z.-J. Wang, P. Jiang, and I. Gursul, “Effect of Thrust-Vectoring Jets on Delta Wing Aerodynamics,” *J. Aircr.*, vol. 44, no. 6, pp. 1877–1888, Nov. 2007.
- [49] F. Y. Wang and K. B. M. Q. Zaman, “Aerodynamics of a Jet in the Vortex Wake of a Wing,” *AIAA J.*, vol. 40, no. 3, pp. 401–407, Mar. 2002.
- [50] G. Taylor, T. Schnorbus, and I. Gursul, “An Investigation of Vortex Flows over Low Sweep Delta Wings,” in *33rd AIAA Fluid Dynamics Conference and Exhibit*, American Institute of Aeronautics and Astronautics, 2003.
- [51] E. P. Symons and T. L. Labus, “Experimental Investigation of an Axisymmetric Fully Developed Laminar Free Jet,” p. 20, 1971.
- [52] H. J. Hussein, S. P. Capp, and W. K. George, “Velocity measurements in a high-Reynolds number, momentum-conserving, axisymmetric, turbulent jet,” *J. Fluid Mech.*, vol. 258, pp. 31–75, 1994.
- [53] C. Cetin, “Control of Flow Structure on Low Swept Delta Wing Using Unsteady Leading Edge Blowing,” METU, 2016.



## APPENDIX A

### SOURCE CODES OF CALCULATION OF PRESSURE COEFFICIENT

```
clear all;
close all;
clc;
addpath ./TestFiles
%=====
% Coordinates of Station 1 of the Delta Wing
xSt1 = [0.239583333 0.347916667 0.45625 0.564583333 0.672916667];
% Coordinates of Station 2 of the Delta Wing
xSt2 = [0.136904762 0.198809524 0.260714286 0.322619048 0.38452381
0.446428571 0.508333333 0.570238095 0.632142857 0.694047619
0.755952381 0.817857143];
% Coordinates of Station 3 of the Delta Wing
xSt3 = [0.095833333 0.138833333 0.225833333 0.3125 0.399166667
0.485833333 0.5725 0.659166667 0.745833333 0.8325];
%=====
% Read Data Here
% Case 1: No Blowing
% Case 2: Cnu = 0.005
% Case 3: Cnu = 0.01
% Case 4: Cnu = 0.02

% Initializing variables
zer1 = zeros(size(xSt1)); zer2 = zeros(size(xSt2)); zer3 =
zeros(size(xSt3));
%=====
% INPUTS
% Number of Samples for the DataSet
fprintf('Number of Samples: %d\n', NSamples);
fprintf('Reading Reference Data\n');
fprintf('Read Zero Data, select 1st station then 2nd station.\n');
% Calling subfunction to extract data from raw data when the wind
tunnel is off
[CalData] = ReadGokayZeroData();
%=====
% Start of read zero blow data
Case1_1 = zer1; Case1_2 = zer2; Case1_3 = zer3;
for i=1:NSamples
    fprintf('Read No Blowing Case, select 1st station then 2nd
station\n');
    fprintf('Reading Sample Number: %d\n', i);
    % Calling subfunction to extract data from raw data
    [Case1_1S Case1_2S Case1_3S] = ReadGokayData(CalData);
    Case1_1 = Case1_1+Case1_1S';
    Case1_2 = Case1_2+Case1_2S';
    Case1_3 = Case1_3+Case1_3S';
end
% Taking average of samples
```

```

Case1_1 = Case1_1/NSamples;
Case1_2 = Case1_2/NSamples;
Case1_3 = Case1_3/NSamples;
% End of read zero blow data
%=====
% Start of read Cnu = 0.005 case data
Case2_1 = zer1; Case2_2 = zer2; Case2_3 = zer3;
for i=1:NSamples
    fprintf('Read Cnu = 0.005 Case, select 1st station then 2nd
station\n');
    fprintf('Reading Sample Number: %d\n', i);
    % Calling subfunction to extract data from raw data
    [Case2_1S Case2_2S Case2_3S] = ReadGokayData(CalData);
    Case2_1 = Case2_1+Case2_1S';
    Case2_2 = Case2_2+Case2_2S';
    Case2_3 = Case2_3+Case2_3S';
end
% Taking average of samples
Case2_1 = Case2_1/NSamples;
Case2_2 = Case2_2/NSamples;
Case2_3 = Case2_3/NSamples;
% End of read Cnu = 0.005 case data
%=====
% Start of read Cnu = 0.01 case data
Case3_1 = zer1; Case3_2 = zer2; Case3_3 = zer3;
for i=1:NSamples
    fprintf('Read Cnu = 0.01 Case, select 1st station then 2nd
station\n');
    fprintf('Reading Sample Number: %d\n', i);
    % Calling subfunction to extract data from raw data
    [Case3_1S Case3_2S Case3_3S] = ReadGokayData(CalData);
    Case3_1 = Case3_1+Case3_1S';
    Case3_2 = Case3_2+Case3_2S';
    Case3_3 = Case3_3+Case3_3S';
end
% Taking average of samples
Case3_1 = Case3_1/NSamples;
Case3_2 = Case3_2/NSamples;
Case3_3 = Case3_3/NSamples;
% End of read Cnu = 0.01 case data
%=====
% Start of read Cnu = 0.02 case data
Case4_1 = zer1; Case4_2 = zer2; Case4_3 = zer3;
for i=1:NSamples
    fprintf('Read Cnu = 0.02 Case, select 1st station then 2nd
station\n');
    fprintf('Reading Sample Number: %d\n', i);
    % Calling subfunction to extract data from raw data
    [Case4_1S Case4_2S Case4_3S] = ReadGokayData(CalData);
    Case4_1 = Case4_1+Case4_1S';
    Case4_2 = Case4_2+Case4_2S';
    Case4_3 = Case4_3+Case4_3S';
end
% Taking average of samples
Case4_1 = Case4_1/NSamples;
Case4_2 = Case4_2/NSamples;
Case4_3 = Case4_3/NSamples;
% End of read Cnu = 0.02 case data
%=====

```

```

% Figure 1: Compares results of Station 1 of the Delta Wing
fgh = figure (1);
% Specify properties of Figure 1
h1 = axes;
% Specify Size of Figure
FigureSize = [4.0,4.0,16.0,16.0];
set(fgh, 'Units', 'centimeters ');
set(fgh, 'Position', FigureSize);
% Set X axis Limit
set(gca, 'XLim', [0.0 1.0]);set(gca, 'FontSize', fs-4);
set(gca, 'YLim', [0.0 2.0]);
% set(gca, 'YTick', [-0.2:0.2:2.0]);
% set(gca, 'YTickLabel', [-0.2:0.2:2.0]);
xlabel('\bf{y/s}', 'FontSize', fs+2);
ylabel('\bf{-C_p}', 'FontSize', fs+2);

hold on;      grid on;
%=====
% Plotting No Blowing, Cnu = 0.005, Cnu = 0.01, Cnu = 0.02 cases for
Station 1 of the Delta Wing
h00 = plot(xSt1,Case1_1, 'k-
+', 'MarkerSize', MS, 'MarkerEdgeColor', 'k', 'LineWidth', lw);
h01 = plot(xSt1,Case2_1, 'b-
s', 'MarkerSize', MS, 'MarkerEdgeColor', 'b', 'LineWidth', lw);
h02 = plot(xSt1,Case3_1, 'm-
o', 'MarkerSize', MS, 'MarkerEdgeColor', 'm', 'LineWidth', lw);
h03 = plot(xSt1,Case4_1, 'r-
<', 'MarkerSize', MS, 'MarkerEdgeColor', 'r', 'LineWidth', lw);
%=====
string00='No Control';
string01='\mu = 0.005';
string02='\mu = 0.01';
string03='\mu = 0.02';
%
leg = legend( [h00, h01,h02,h03],{string00,
string01,string02,string03});
set(leg, 'fontsize', fs, 'Location', 'NorthWest', 'box', 'off');
hold off;
%=====
% Figure 2: Compares results of Station 2 of the Delta Wing
fgh = figure (2);
% Specify properties of Figure 2
h1 = axes;
% Specify Size of Figure
FigureSize = [4.0,4.0,16.0,16.0];
set(fgh, 'Units', 'centimeters ');
set(fgh, 'Position', FigureSize);
% Set X axis Limit
set(gca, 'XLim', [0.0 1.0]);set(gca, 'FontSize', fs-4);
set(gca, 'YLim', [0.0 2.0]);
% set(gca, 'YTick', [-0.2:0.2:2.0]);
% set(gca, 'YTickLabel', [-0.2:0.2:2.0]);
%
xlabel('\bf{y/s}', 'FontSize', fs+2);
ylabel('\bf{-C_p}', 'FontSize', fs+2);
hold on;      grid on;
%=====
% Plotting No Blowing, Cnu = 0.005, Cnu = 0.01, Cnu = 0.02 cases for
Station 2 of the Delta Wing

```

```

h00 = plot(xSt2,Case1_2,'k-
+', 'MarkerSize',MS, 'MarkerEdgeColor', 'k', 'LineWidth',lw);
h01 = plot(xSt2,Case2_2,'b-
s', 'MarkerSize',MS, 'MarkerEdgeColor', 'b', 'LineWidth',lw);
h02 = plot(xSt2,Case3_2,'m-
o', 'MarkerSize',MS, 'MarkerEdgeColor', 'm', 'LineWidth',lw);
h03 = plot(xSt2,Case4_2,'r-
<', 'MarkerSize',MS, 'MarkerEdgeColor', 'r', 'LineWidth',lw);
%=====
string00='No Control';
string01='\mu = 0.005';
string02='\mu = 0.01';
string03='\mu = 0.02';
%
leg = legend( [h00, h01,h02,h03],{string00,
string01,string02,string03});
set(leg, 'fontsize',fs, 'Location', 'NorthWest', 'box', 'off');
hold off;
%=====
% Figure 3: Compares results of Station 3 of the Delta Wing
fgh = figure (3);
% Specify properties of Figure 3
h1 = axes;
% Specify Size of Figure
FigureSize = [4.0,4.0,16.0,16.0];
set(fgh, 'Units', 'centimeters ');
set(fgh, 'Position', FigureSize);
% Set X axis Limit
set(gca, 'XLim', [0.0 1.0]);set(gca, 'FontSize',fs-4);
set(gca, 'YLim', [0.0 2.0]);
% set(gca, 'YTick', [-0.2:0.2:2.0]);
% set(gca, 'YTickLabel', [-0.2:0.2:2.0]);
%
xlabel('\bf{y/s}', 'FontSize',fs+2);
ylabel('\bf{-C_p}', 'FontSize',fs+2);
hold on;      grid on;
%=====
% Plotting No Blowing, Cnu = 0.005, Cnu = 0.01, Cnu = 0.02 cases for
Station 3 of the Delta Wing
h00 = plot(xSt3,Case1_3,'k-
+', 'MarkerSize',MS, 'MarkerEdgeColor', 'k', 'LineWidth',lw);
h01 = plot(xSt3,Case2_3,'b-
s', 'MarkerSize',MS, 'MarkerEdgeColor', 'b', 'LineWidth',lw);
h02 = plot(xSt3,Case3_3,'m-
o', 'MarkerSize',MS, 'MarkerEdgeColor', 'm', 'LineWidth',lw);
h03 = plot(xSt3,Case4_3,'r-
<', 'MarkerSize',MS, 'MarkerEdgeColor', 'r', 'LineWidth',lw);
%=====
string00='No Control';
string01='\mu = 0.005';
string02='\mu = 0.01';
string03='\mu = 0.02';
%
leg = legend( [h00, h01,h02,h03],{string00,
string01,string02,string03});
set(leg, 'fontsize',fs, 'Location', 'NorthWest', 'box', 'off');
hold off;
%=====

```

### Sub class codes to read pressures with noblow :

% Start of converting LabView noblow pressure data to readable one

```
function [CalData] = ReadGokayZeroData()  
%===== %  
skData = 1;  
for stationNum = 1:2  
    filename = uigetfile('./TestFiles/*.csv');  
    [fid, message]=fopen(filename,'r');  
    %  
    for i =1:7  
        line = fgetl(fid);  
    end  
    %  
    sk=1;  
    line = fgetl(fid);  
    while(line~-=-1)  
        line = strrep(line, ',', '.'); line = str2num(line);  
        %  
        Data(sk,:) = line;  
        sk = sk+1;  
        line = fgetl(fid);  
    end  
    % %  
    DataMeanDummy = mean(Data(:,2:end),1);  
  
    CalDataMean(skData,:) = DataMeanDummy; skData =skData+1;  
    fclose(fid);  
end  
  
CalData = CalDataMean;  
  
end
```

### Sub class codes to read pressures with blowing:

% Start of converting LabView pressure data to readable one

```
function [Data1 Data2 Data3] = ReadGokayData(CalData)  
%===== %  
MapSt1 = [1 2 3 4 29];  
MapSt2 = [17 18 19 20 21 22 23 24 25 26 27 28];  
MapSt3 = [5 6 7 8 9 10 11 12 13 14];  
%===== %  
skData= 1;  
for stationNum = 1:2  
    filename = uigetfile('./TestFiles/*.csv');  
    % filename = '7-14x-1-a_Stream1.csv';  
    [fid, message]=fopen(filename,'r');  
    %  
    for i =1:7  
        line = fgetl(fid);  
    end
```

```

%
sk=1;
line = fgetl(fid);
while(line~-=-1)
    line = strrep(line, ',', '.'); line = str2num(line);
    %
    Data(sk,:) = line;
    sk = sk+1;
    line = fgetl(fid);
end
% %
DataMeanDummy = mean(Data(:,2:end),1);
%
DataMeanDummy = DataMeanDummy - (CalData( stationNum,:));

for dataDot=1:14
    DataMeanDummy(dataDot)=(DataMeanDummy(15) -
DataMeanDummy(dataDot)) ...
    / (DataMeanDummy(16)-DataMeanDummy(15));
end

DataMean(skData,:) = DataMeanDummy; skData =skData+1;

fclose(fid);
end
%=====
DataMean = DataMean';
DataMean
%
Data1 = DataMean(MapSt1(:));
Data2 = DataMean(MapSt2(:));
Data3 = DataMean(MapSt3(:));
end

```

## APPENDIX B

### CALCULATION OF UNCERTAINTY

```
% Sample uncertainty calculation for 7 degree and Re=35000 with no
blowing

clear all;
close all;
clc;

% Measurements and known

p = -13.1081264;      % Pressure tap static pressure
p_sta = -12.102595;  % Pitot tube static pressure
p_tot = -6.2793536;  % Pitot tube total pressure
a = 0.3;             % Length of span in meter
h = 0.15;           % Length of chord in meter
d = 0.002*cos(pi/4); % Diameter of blowing hole
Q = 13.45*pi*d^2/4; % Flow rate passing through blowing hole
rho = 1.067;        % Density of the air

% Individual uncertainties of each variable

dp = p*0.0005;
dp_sta = p_sta*0.0005;
dp_tot = p_tot*0.0005;
dp_dyn = sqrt(0.0005^2+0.0005^2)
da = 0.0005;
dh = 0.0005;
dd = 5.0e-5;
dQ = 0.05/(1000*60);

difference= [abs(dp/p); abs(dp_sta/p_sta); abs(dp_tot/p_tot);
abs(da/a); abs(dh/h); abs(dd/d); abs(dQ/Q)];

% Calculating pressure coefficient uncertainty

dCpdp = 1/(p_tot-p_sta);
dCpdp_sta = (p-p_sta)/(p_tot-p_sta)^2;
dCpdp_tot = (p_sta-p)/(p_tot-p_sta)^2;

dCp = [dCpdp*dp; dCpdp_sta*dp_sta; dCpdp_tot*dp_tot];
dCp = norm(dCp);

Cp = (p-p_sta)/(p_tot-p_sta);
percentile_Cp = abs(dCp/Cp)*100
```

```

% Calculating momentum coefficient uncertainty

dCmdQ = 8*Q*rho/((p_tot-p_sta)*a*h*pi*d^2);
dCmdp_tot = -4*Q^2*rho/((p_tot-p_sta)^2*a*h*pi*d^2);
dCmdp_sta = 4*Q^2*rho/((p_sta-p_tot)^2*a*h*pi*d^2);
dCm da = -4*Q^2*rho/((p_tot-p_sta)*a^2*h*pi*d^2);
dCmdh = -4*Q^2*rho/((p_tot-p_sta)*a*h^2*pi*d^2);
dCm dd = -8*Q^2*rho/((p_tot-p_sta)*a*h*pi*d^3);

dCm = [dCmdQ*dQ; dCmdp_tot*dp_tot; dCmdp_sta*dp_sta; dCm da*da;
dCmdh*dh; dCm dd*dd];
dCm = norm(dCm);

Cm = 4*Q^2*rho/((p_tot-p_sta)*a*h*pi*d^2);
percentile_Cm = abs(dCm/Cm)*100

```

# APPENDIX C

## PRESSURE MEASUREMENTS FOR $Re=20000$

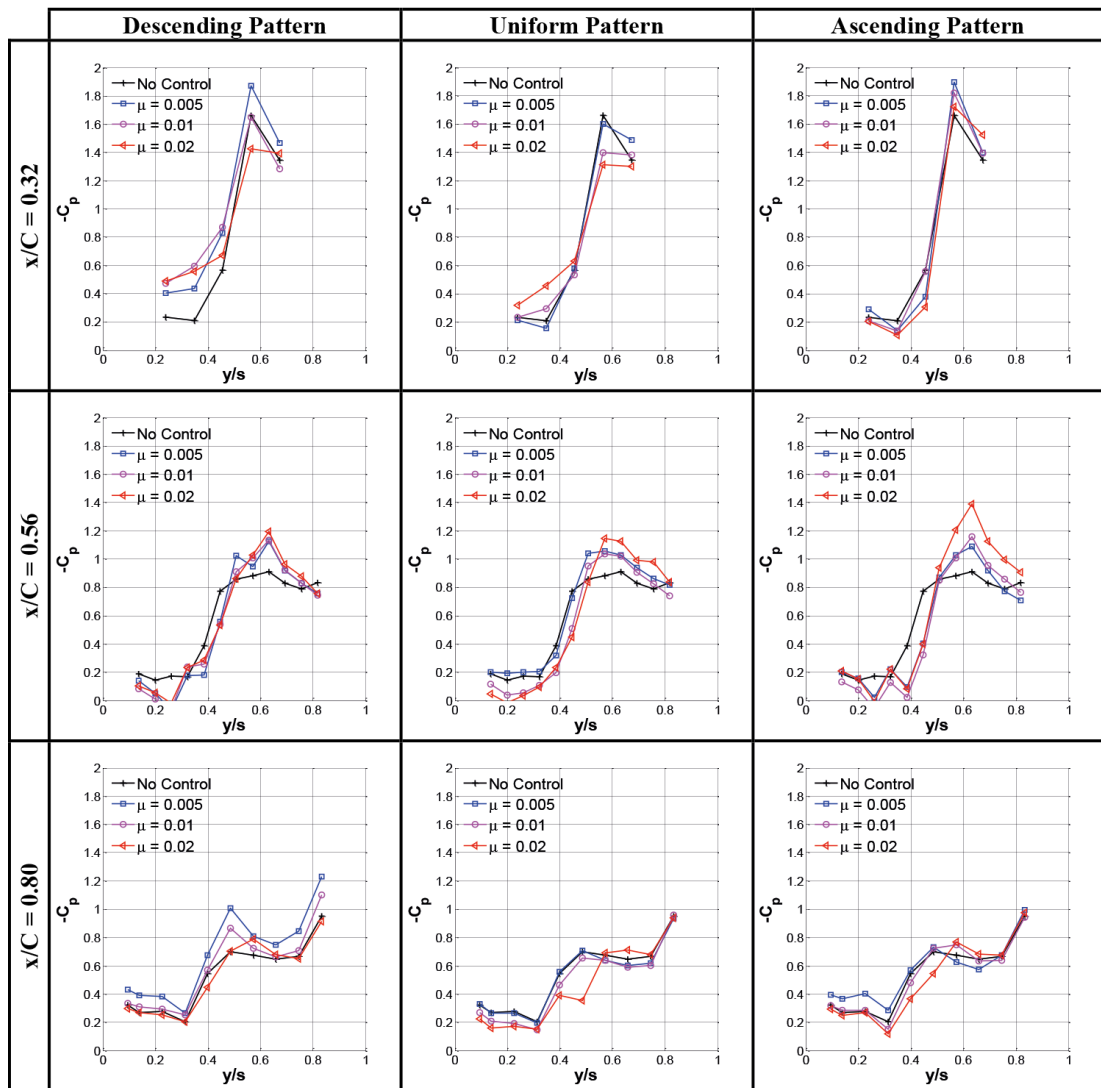


Figure C.1 Spanwise  $-C_p$  plots at  $\alpha = 7^\circ$  angle of attack and  $Re=20000$  on chordwise distances of  $x/C = 0.32, 0.56$  and  $0.80$  and different Reynolds numbers

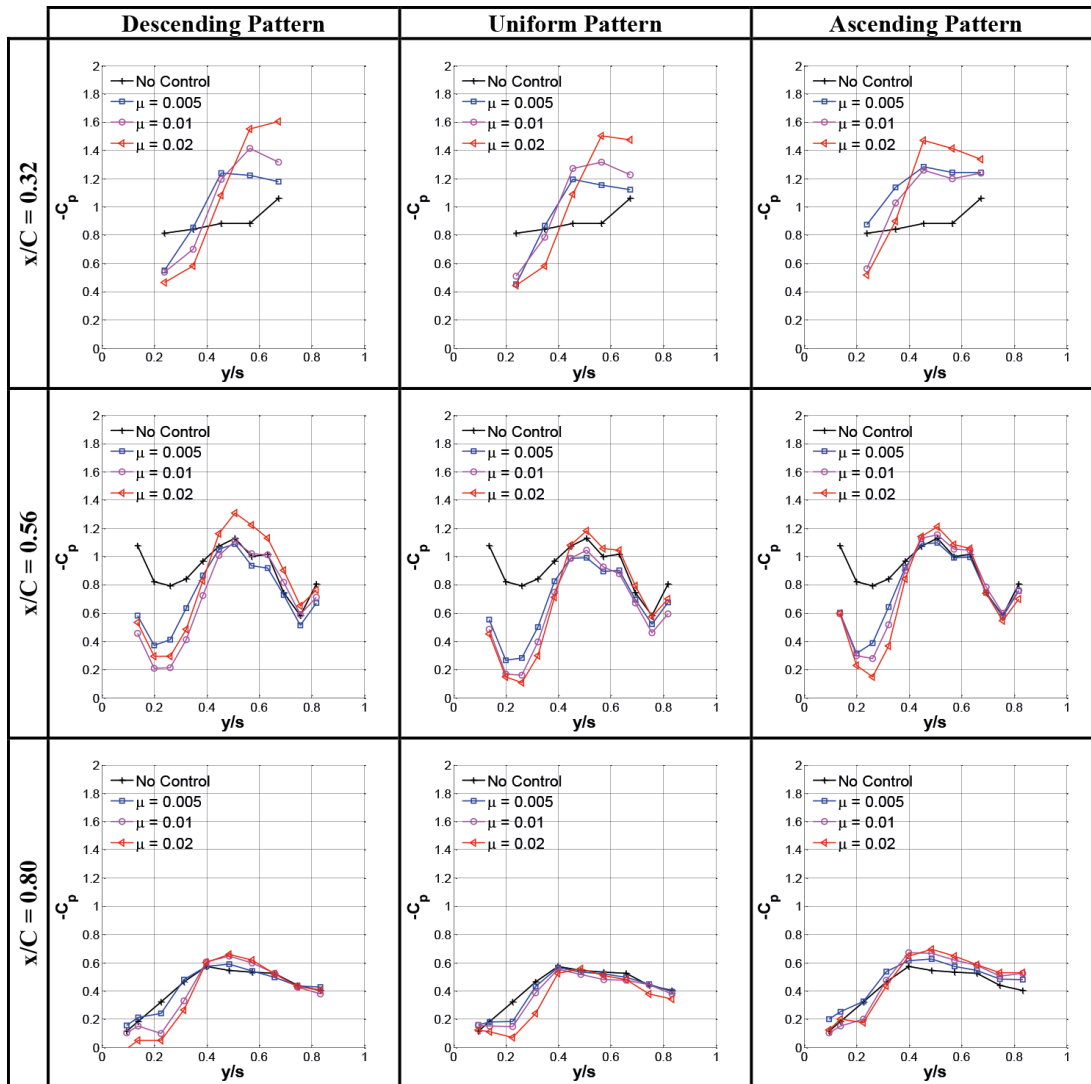


Figure C.2 Spanwise  $-C_p$  plots at  $\alpha = 13^\circ$  angle of attack and  $Re=20000$  on chordwise distances of  $x/C = 0.32, 0.56$  and  $0.80$  and different Reynolds numbers

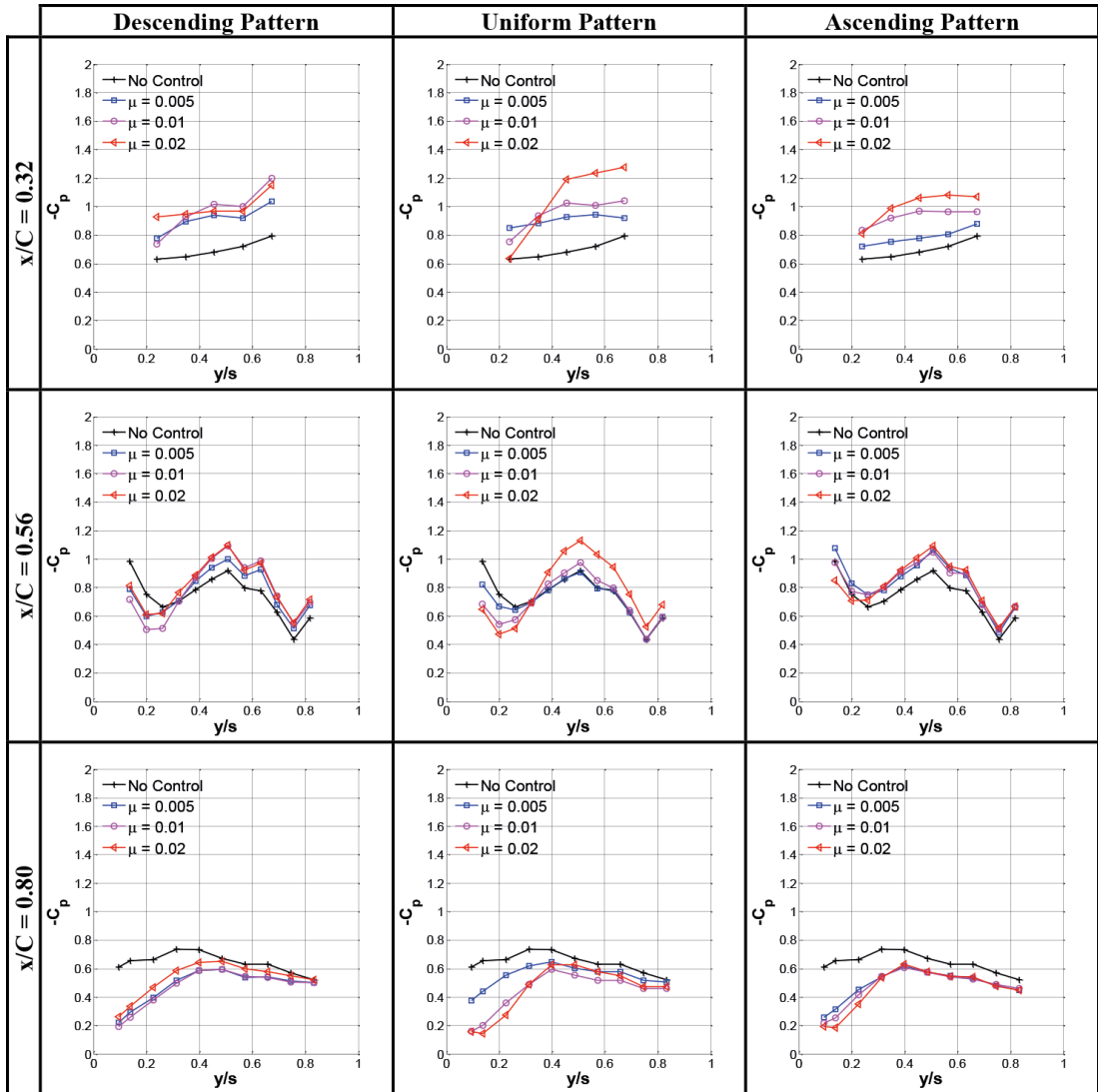


Figure C.3 Spanwise  $-C_p$  plots at  $\alpha = 16^\circ$  angle of attack and  $Re=20000$  on chordwise distances of  $x/C = 0.32, 0.56$  and  $0.80$  and different Reynolds numbers